Active photonic devices based on spin crossover molecules

Lijun Zhang

Université Fédérale

Toulouse Midi-Pyrénées

THÈSE

En vue de l'obtention du

DOCTORAT DE L'UNIVERSITÉ DE TOULOUSE

Délivré par :

Université Toulouse 3 Paul Sabatier (UT3 Paul Sabatier)

Présentée et soutenue par :
Lijun ZHANG

le mercredi 20 septembre 2023

Titre :

Dispositifs photoniques actifs à base de molécules à transition de spin

---

École doctorale et discipline ou spécialité :
ED SDM : Sciences et génie des matériaux - CO034

Unité de recherche :
LCC - Laboratoire de Chimie de Coordination

Directeur/trice(s) de Thèse :

Lionel SALMON et Gabor MOLNAR

Jury :
M. Maciej LORENC, Rapporteur
Mme Grace MORGAN, Rapporteure
M. Georges LANDA, Examinateur
M. Lionel SALMON, Directeur de thèse
M. Gabor MOLNAR, Invited
M. Stéphane CALVEZ, Invited

Acknowledgments

I am very grateful to all members of the jury for taking the time and energy to read my manuscript and participate in the defense process and thank all of them for their comments and corrections on my thesis.

I am deeply grateful to my supervisor Gábor Molnár for his comprehensive guidance on this work, which enabled me to complete my thesis; he has a wealth of knowledge and rigorous logical thinking, leading to accurate feedback and guidance for my experiments; his optimistic attitude deeply infected me, especially when I encountered difficulties in the early experiments. I would like to thank him for his patience and help over the past three years.

I am deeply grateful to Dr. Karl Ridier for leading me through this work. He has profound knowledge, innovative thinking, excellent analytical ability for experiments, and professional guidance for my work, all of which have benefited me a lot; he always taught me a lot of experimental skills and scientific research knowledge sincerely and patiently; in the face of every experimental challenge, he can always lead me to solve the problem optimistically and positively.

I would like to thank Dr. Stéphane Calves for his valuable advice and sincere guidance on this work. I would like to thank Dr. Lionel Salmon and Dr. Azzedine Bousseksou for giving me the opportunity to join this research team, and often giving me encouragement and advice. Their kindness made me feel a lot of warmth.

I would like to thank everyone in the Switchable Molecular Materials Team (Equipe P) for their help and support: William, Lucie, Saioa, Kane, Alejandro, Yuteng, Seyed, Ayman, Yue, Oleksandr, Shiteng, Ion, Fayan, Yongjian, Xinyu, Livia, Onkar, Maryam, Lydia. I would also like to thank all the friends I met during my Ph.D. who brought a lot of help and joy to my life.

Finally, I would like to thank my family for their spiritual support and their great concern for me, which gave me a lot of happiness and courage.

I am grateful to the China Scholarship Council for the Ph.D. grant.

Table of contents

List of abbreviations

PCMs	Phase-change materials
PIC	Photonic integrated circuits
SCO	Spin-crossover
HS	High spin
LS	Low spin
TIR	Total internal reflection
UV	Ultraviolet
Vis	Visible
FTIR	Fourier-transform infrared
LIESST	light Induced Excited Spin State Trapping
LD-LISC	Ligand-Driven Light Induced Spin Crossover
ptz	1-propyltetrazole
stpy	py-CH=CH-Ph
IR	Infrared
phen	1, 10-phenanthroline
DSC	Differential scanning calorimetry
XRD	X-ray diffraction
GIXRD	Grazing-incidence X-ray diffraction
tz	1,2,4-triazol-1-yl
NIR	near-infrared
MLCT	metal-ligand charge transfer
DIC	Differential interference microscopy
SPRM	Surface plasmon resonance microscopy
SPR	Surface plasmon resonance
LSPR	Localized surface plasmon resonance
SPPs	Surface plasmon polaritons
FOM	Figure of merit

O-PCM	Optical phase-change materials
pic	2-picolylamine
SLMs	Spatial light modulators
GST	$Ge_2Sb_2Te_5$
FSR	Free spectral range
AFM	atomic force microscopy
AOI	Angle of incidence
FWHM	Full width at half maximum
EM	Electromagnetic
USC	Ultra-strong coupling
VSC	Vibrational strong coupling
SPI	Spiropyran
MC	Merocyanine

GENRAL INTRODUCTION

GENERAL INTRODUCTION

Nanomaterials that undergo electronic and/or structural phase transition, associated with a reversible change of optical properties, have received recently increasing attention for the development of active photonic devices [Miller 2018; Zilun 2021] as well as for fundamental research in light-matter interactions. These phase-change materials (PCMs) exhibit large changes of the complex refractive index in response to an external stimulus (e.g. heat, voltage bias or light irradiation), which has been exploited for a variety of photonic applications such as smart windows [Beeckman 2011], optical memories [Wuttig 2017], spatial light modulators [Zhang 2019] and photonic integrated circuits (PIC) [Delaney 2020]. The most widely studied PCMs are transition metal oxides exhibiting metal-insulator transition, chalcogenide alloys showing amorphous-crystalline phase change and liquid crystals displaying order-disorder type transitions [Miller 2018; Zilun 2021], Among these materials, however, only liquid crystals have been readily employed in applications requiring transparency in the visible spectral range. Yet, the span of applications of liquid crystals remains restricted by the slow switching rates and high scattering losses as well as by the need for their encapsulation [Beeckman 2011].

In this context, molecular spin-crossover (SCO) compounds represent a promising novel class of phase-change materials with high potential for active photonics applications [Molnár 2018]. These transition metal complexes are known to display fast and reversible spin-state switching between the low-spin (LS) and high-spin (HS) electronic configurations of the central metal ion under various stimuli [Gütlich 2004]. Experimental and theoretical studies to elucidate the mechanism of switching between the high spin (HS) and low spin (LS) electronic configurations of the central metal ion have been ongoing for nearly a century and a number of recent reviews and books indicate the continuing interest in this subject [Gütlich 2004; Bousseksou 2011; Halcrow 2013; Kumar 2017, Bousseksou 2018]. In the past decade, attention in SCO materials for technological applications has been significantly increased through major advances in the synthesis and manipulation of SCO nanomaterials in a variety of forms

such as nanoparticles, thin films, nano-patterns, nano-heterostructures and nanocomposites [Molnár 2018].

Based on these advances, this thesis focuses on SCO-based active optical devices and takes benefit from the fact that the spin switching is accompanied by substantial changes in optical properties. Considering the complex refractive index $n^* = n + ik$, with a real part (refractive index, n) and an imaginary part (extinction coefficient, k), we propose two research strategies. The first strategy capitalizes on the variation of the refractive index at the SCO and the associated change of phase velocity of light to implement active tuning of optical devices. The second, unprecedented, strategy focuses on the extinction coefficient k, and studies the influence of absorbance changes on the degree of hybridization between SCO molecules and electromagnetic modes within optical cavities.

The scientific background and the results obtained during this thesis work are described in three chapters.

Chapter 1 provides an introduction to the SCO phenomenon. The molecular mechanism of spin crossover is briefly reminded using the crystal field theory. Then, we describe the most commonly observed SCO behaviors (gradual, abrupt, stepwise) and the notion of cooperativity is introduced. This is followed by the discussion of the effect of temperature, pressure and light irradiation on the spin state of the molecules. Finally, the resulting physical property changes and associated characterization methods are overviewed with special emphasis on the optical properties (refractive index and color changes).

Chapter 2 focuses on the change of refractive index of SCO materials in the context of active optical devices. We investigate two different resonators based on thin films of the same SCO complex **1** [Fe(HB(1,2,4-triazol-1-yl)$_3$)$_2$]. First, we discuss the fabrication and properties of Ag/**1**/Ag Fabry-Pérot cavities, which consist of two parallel silver layers as mirrors and the film of **1** as the dielectric layer sandwiched between them. This is followed by the investigation of Ag/**1** bilayer resonators, excited

in total internal reflection (TIR) geometry using a coupling prism. The optical properties of these two resonators are studied by measuring the resonance spectra as a function of the incident angle, polarization and temperature. We assess several important figures of merit, such as the shift of the resonance wavelength upon the SCO, the quality factor and the achievable reflectance (or transmittance) contrast. Finally, we exploit this tunability to demonstrate photothermal nonlinearity and optical limiting application for the Ag/**1** bilayer resonator.

Chapter 3 devises, for the first time, a strategy based on the change of the extinction coefficient k on the light-matter hybridization strength, brought into by the SCO phenomenon. To this aim, we used Al/SCO bilayer resonators, made of high quality thin films of the complexes [Fe(HB(1,2,4-triazol-1-yl)$_3$)$_2$] **1**, and [Fe(HB(1,2,3-triazol-1-yl)$_3$)$_2$] **2**, displaying abrupt and gradual SCO behaviors, respectively. The cavity mode was tuned into resonance with an optical dipole transition in the low spin state of the complexes, affording for light matter hybridization. The coupling strength was then investigated through the thermally induced switching of the molecules between their low-spin and high-spin states, offering the appealing possibility of a reversible switching between the ultrastrong and weak coupling regimes within the cavity.

The thesis end with a few general conclusions and perspectives for further work.

CHAPTER 1:

A BRIEF INTRODUCTION TO THE MOLECULAR SPIN CROSSOVER PHENOMENON

CHAPTER 1: A BRIEF INTRODUCTION TO THE MOLECULAR SPIN CROSSOVER PHENOMENON

Spin-crossover molecules are octahedral transition metal complexes with $3d^4$-$3d^7$ electronic configurations, including complexes of Cr^{II}, Mn^{III}, Mn^{II}, Fe^{III}, Fe^{II}, Co^{III} and Co^{II}. When subjected to external stimuli (such as temperature, pressure, light radiation, etc.), these transition metal complexes can reversibly convert between their high spin and low spin electronic configurations, called spin crossover (SCO), which is accompanied by changes in bond lengths and angles and, ultimately, by changes of physical properties such as magnetic moment, dielectric permittivity, heat capacity, elastic constants and color. As a result, the SCO phenomenon can be characterized by a plethora of techniques, including magnetic susceptibility measurements, electronic spectroscopy (UV-VIS), vibrational spectroscopy (Raman, FTIR), X-ray diffraction, dielectric spectroscopy, calorimetry and so forth. Importantly, in bulk materials, the manifestation of the SCO phenomenon is considerably altered by short- and long-range elastic interactions between the molecules in the crystal lattice, whereas in nano-scale materials the influence of surface/interface properties need to be also considered. Potentially, spin-crossover materials provide a broad scope for technological applications in sensing, display, actuation and information processing devices. In this chapter, after a general introduction, we mainly focus on the changes of optical properties accompanying the spin state switching and associated application ideas.

1.1. Splitting of d-orbitals in octahedral complexes

To understand the origin of the spin-crossover phenomenon in transition metal complexes, first we need to consider the effect of ligands on the central metal ion [Hauser 2004a]. The simplest approach, the so-called crystal-field theory, treats the interaction between the transition metal ion and the ligands is analogous to the electrostatic attraction of positive and negative ions in ionic crystals. The role of the ligands is to establish the negative charge potential field, called the crystal field. Under the perturbation of the crystal field, the degenerated 3d orbitals of the metal ion undergo

energy level splitting. To explain this phenomenon, we need to have a look at the spatial orientation of the five orbitals of the 3d energy level of the metal ion (see Figure1.1):

d_{xy}: the lobes are located between the x and the y axes;

d_{xz}: the lobes are located between the x and the z axes;

d_{yz}: the lobes are located between the y and the z axes;

d_{x2-y2}: the lobes are located on the x and y axes;

d_{z2}: the lobes are essentially located on the z axes.

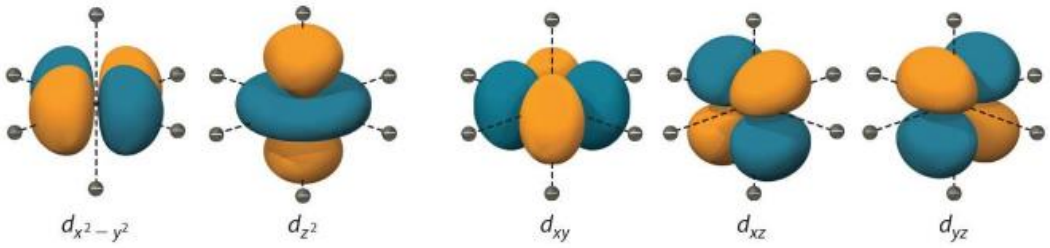

Figure 1.1. Schematic representation of the 3d orbitals in an octahedral complex.

In the free metal ion, the five degenerate d-orbitals have the same energy, namely $E_{dxy} = E_{dxz} = E_{dyz} = E_{dx^2-y^2} = E_{dz^2}$. Under a negatively charged spherical field, the energy of the 3d orbitals increases uniformly, but the energy levels are not split. Let us now consider the action of a field with a perfect octahedral geometry, wherein the metal ion is located in the center of the octahedron and the six ligands approach the metal ion along the positive and negative directions of the three coordinate axes (Figure 1.2). Due to the different orientations of the d-orbitals, the repulsion between the crystal field and the 3d orbitals electrons is also different, resulting in the splitting of energy levels in the 3d orbitals to reduce the total energy of the system. Under the perturbation of the octahedral crystal field, two energy levels will be formed. The lower energy level, called t_{2g}, consists of three non-bonding, degenerate orbitals d_{xy}, d_{xz}, d_{xz}. The higher energy level, called e_g, consists of two anti-bonding degenerate orbitals d_{x2-y2}, d_{z2}. The energy gap between these two energy levels is called the crystal field splitting energy

$\Delta_o=E_{e_g}-E_{t_{2g}}$, also denoted as 10Dq, a semi-empirical constant that depends on the strength of the crystal field.

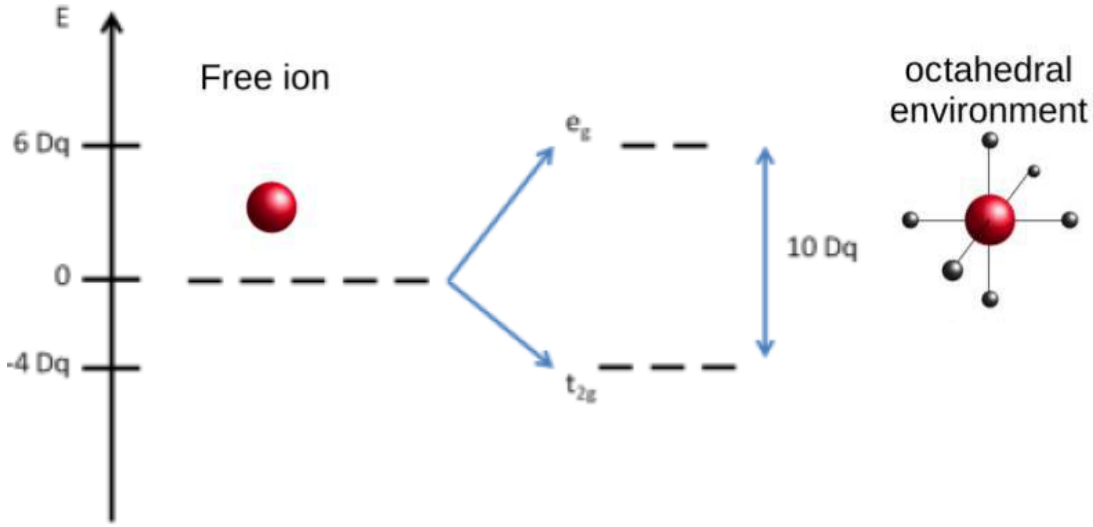

Figure 1.2. Influence of an octahedral environment on the 3d orbitals of a transition metal ion.

In addition to the crystal field splitting energy, one needs to consider also the spin pairing energy Π, which is the energy required to overcome the repulsion between electrons in the same orbit. As a result, two main effects are competing. On one hand, according to the lowest energy principle, the 3d electrons should preferentially occupy the lower energy t_{2g} orbitals. On the other hand, due to the spin pairing energy, electrons preferentially occupy different orbitals such a way that there is a maximum number of unpaired electrons. Taking the example of Fe(II) complexes, which were used in this thesis, the six electrons of the 3d orbitals may have two different arrangements according to the relative magnitudes of the crystal field splitting energy 10Dq and the spin pairing energy Π. As shown in Figure 1.3, in a weak crystal field (10Dq < Π), the six electrons will occupy each 3d orbitals. In this case, the number of unpaired electrons in the system is 4, then the total spin angular momentum is S= 2, resulting in the maximum spin multiplicity (2S+1=5). This paramagnetic complex is called high-spin (HS). Conversely, in a strong crystal field (10Dq > Π), the electrons will preferentially occupy the low-energy t_{2g} orbitals. In this case, there are no unpaired electrons, resulting

in the smallest spin multiplicity (2S+1=1). This diamagnetic complex is called low spin.

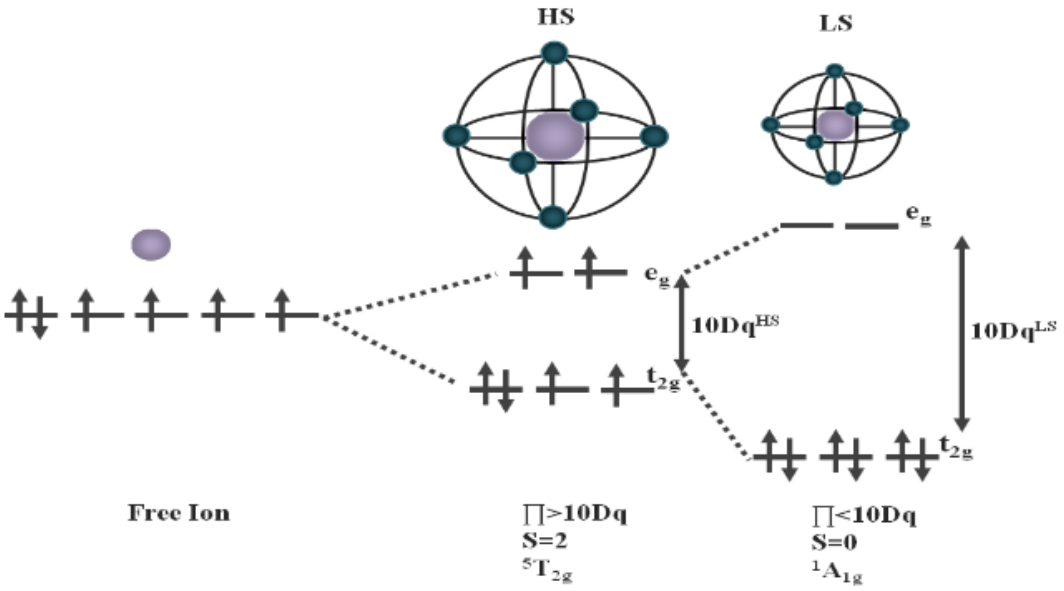

Figure 1.3. Energy splitting of the 3d orbitals of an Fe(II) ion in an octahedral environment induced by the ligand field (10Dq) – showing both the weak field (HS) and strong field (LS) cases.

For a given ligand, the crystal field depends on the distance (r) between the metal ion and the ligand, $\Delta_o = r^{-n}$, with n = 5-6. Choosing this distance as the relevant configurational coordinate, we can sketch a simplified energy diagram of the two spin states. As shown in Figure 1.4, in the vertical direction, the energy at the ground state of the two spin states is different, $\Delta E^0_{HL} = E^0_{HS} - E^0_{LS}$, which means that to achieve thermal spin transition ΔE^0_{HL} must be on the order of thermally accessible energy. In the horizontal direction, the distance between the metal ion and the ligand differs in these two spin states, $\Delta r_{HL} = r_{HS} - r_{LS}$. For complexes with $Fe^{II}N_6$ coordination core (used in this thesis), the average Fe-N distance in the LS and HS states are $r_{LS} \approx 2.0$ Å and $r_{HS} \approx 2.2$ Å, respectively. Therefore, the ratio of the ligand field strengths of these two spin states can be given as:

$$\frac{10Dq^{LS}}{10Dq^{HS}} = \left(\frac{r_{HS}}{r_{LS}}\right)^6 \approx 1.77 \qquad (1)$$

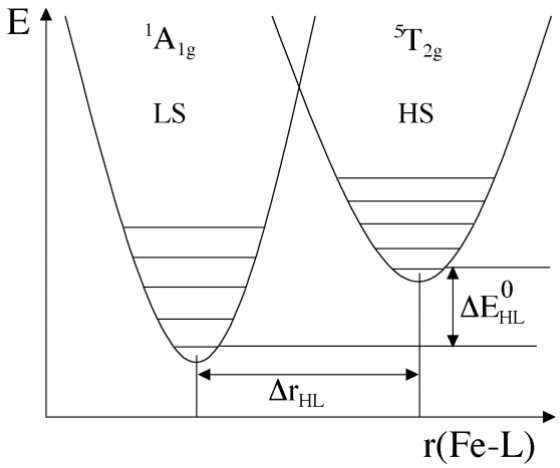

Figure 1.4. Simplified configurational diagram of two molecular spin states (HS and LS) [Hauser 2004a].

The effect of the crystal field on the energy levels of different transition metal ions is depicted in the so-called Tanabe-Sugano diagrams. Figure 1.5 depicts the Tanabe-Sugano diagram of the octahedral Fe(II) complexes [Tanabe 1954]. The electronic configuration of the free Fe(II) ion in the ground state is ^5D. Under the action of the crystal field, this state splits into the HS $^5T_{2g}$ ground state and the ^5E_g excited state. When 10Dq continues to increase beyond a critical value, the situation changes since the LS state ($^1A_1$) becomes the ground state. For octahedral Fe(II) complexes, Hauser estimated ΔE^0_{HL} as a function of the value of 10Dq. As shown in Figure 1.6, three different situations can be encountered [Hauser 2004a]:

1. For $10Dq^{HS} < \sim 10000$ cm^{-1} one obtains $\Delta E^0_{HL} < 0$. In this case, the HS state is the quantum mechanical ground state and the thermodynamically stable state at any temperature.

2.For $10Dq^{LS} > \sim 23000$ cm^{-1} one obtains $\Delta E^0_{HL} > \sim 2000$ cm^{-1}. In this case, the LS state is the quantum mechanical ground state and the thermodynamically stable state up to very high temperatures.

3.For ~ 11000 cm$^{-1} < 10Dq^{HS} < \sim 12500$ cm^{-1} and ~ 19000 cm$^{-1} < 10Dq^{LS} < \sim 22000$ cm^{-1}, $0 < \Delta E^0_{HL} < \sim 2000$ cm^{-1}. In this case, the thermally induced spin crossover may be expected.

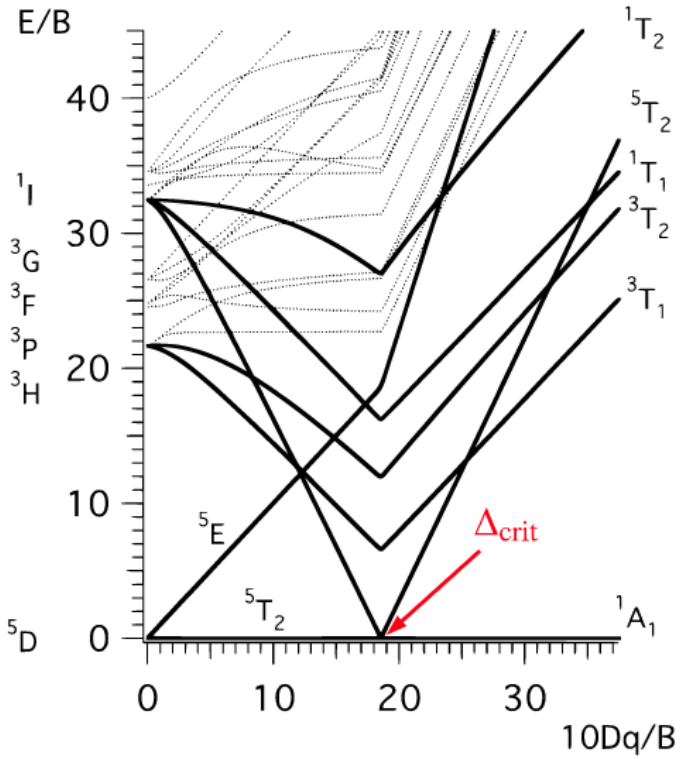

Figure 1.5. Tanabe-Sugano diagram for a transition metal ion with six d electrons in an octahedral ligand field symmetry (in units of the Racah parameter of electron-electronic repulsion, *B*) [Hauser 2004a].

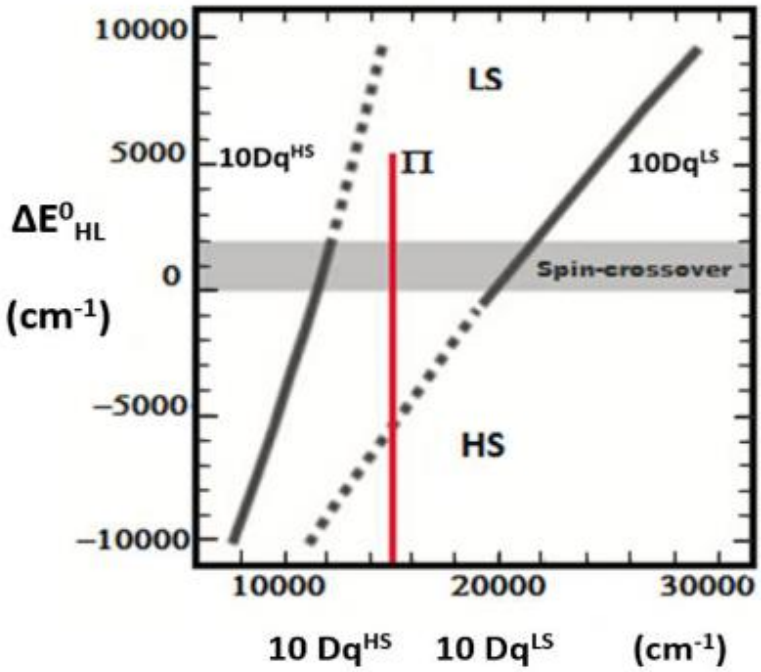

Figure 1.6. Stability regions of the LS and HS states as a function of 10Dq for octahedral Fe(II) complexes [Hauser 2004a].

1.2. Spin crossover in the solid state

1.2.1. Spin crossover curves

When non-interacting spin crossover molecules independently undergo spin state change (for example upon a temperature change), the spin-state of the system will follow a Boltzmann distribution. However, in solid materials, intermolecular interactions cannot be ignored. When the molecule undergoes SCO, the distance between the metal ion and the ligands changes, resulting in a change in the shape and volume of the molecule. This will give rise to a misfit of the molecule in the crystal lattice with important repercussions to its close and the long-range environment, ultimately affecting the energy of the whole lattice. This phenomenon, coined as the cooperativity of the SCO, is shown schematically in Figure 1.7. The magnitude of these elastic interactions [Spiering 2004] mainly depends on the volume change ($\Delta V/V_0$) upon the SCO and the compressibility of the lattice.

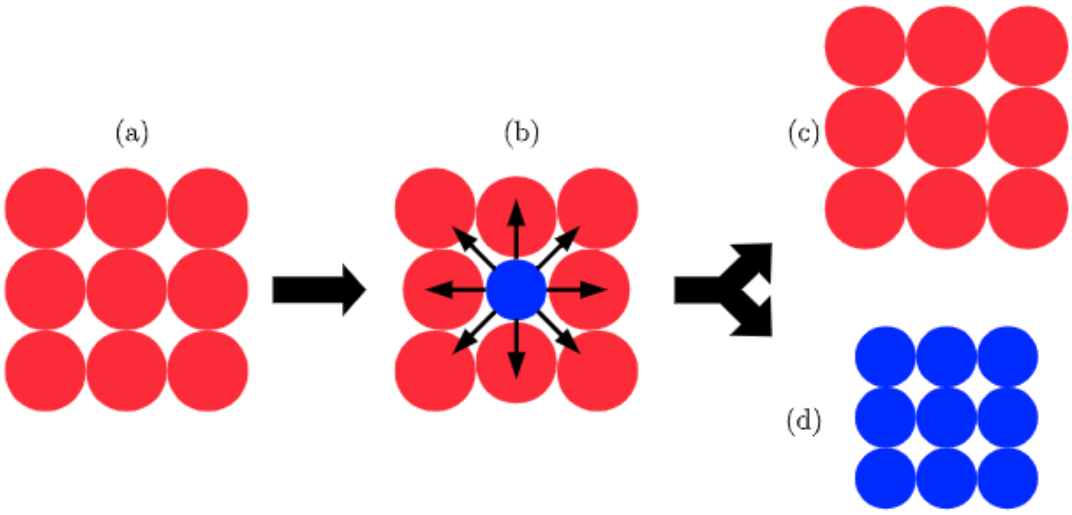

Figure 1.7. Simplified representation of collective mechanisms in the case of a highly cooperative SCO compound. a) The molecules are in the HS state. b) The central molecule is switched to the LS state, which results in a misfit of this molecule in the lattice and an associated increase of the elastic energy. To minimize the energy of the system, c) either the molecule returns to the HS state or d) the neighbors switch collectively to the LS state [Mikolasek 2016].

The spin crossover curve describes the mole fraction of the high spin state of the complex, $\gamma_{HS}(T)$, as a function of temperature. From the shape of the spin crossover curve, much information can be inferred, such as the degree of cooperativity of the system [Nicolazzi 2018]. The most common SCO curves are shown in Figure 1.8.

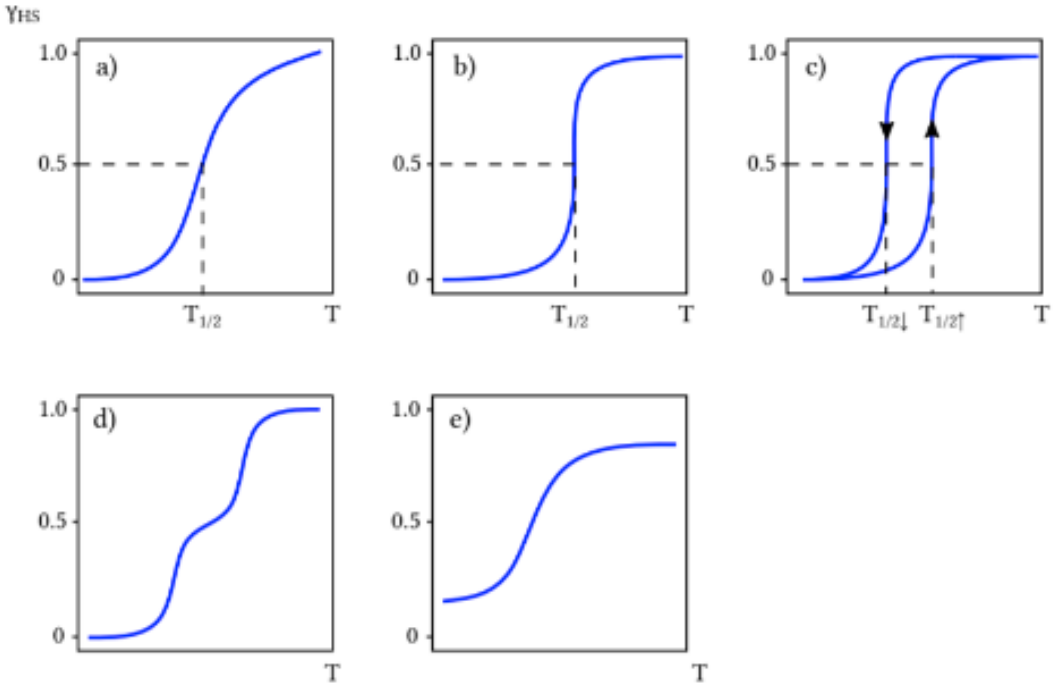

Figure 1.8. Principal types of thermally-driven spin transition curves. a) Gradual spin crossover. b) Abrupt spin transition. c) Spin transition with hysteresis. d) Two-step spin transition. e) Incomplete spin transition [Gütlich 2004].

(a) Gradual spin crossover: In a highly diluted system (such as a solution), intermolecular interactions are negligible (i.e. the cooperativity in the system is weak). In this case, the spin transition phenomenon spans over several tens (or hundreds) of Kelvins resulting in a gradual spin transition curve (see Figure 1.8 a).

(b) Abrupt spin transition: When the cooperativity in the system is enhanced (such as a bulk material), the spin transition becomes more and more abrupt and spans over a smaller temperature range (see Figure 1.8 b).

(c) Spin transition with hysteresis: As the cooperativity increases above a critical value,

the spin crossover becomes eventually discontinuous and a hysteresis loop opens (Figure 1.8 c). In this case, the HS and LS molecules are not miscible anymore, which leads to the creation of a nucleation energy barrier between the two phases. The material will be locked in a metastable state until the energy intake exceeds the energy barrier. As a result, the spin transition temperatures in the heating mode $T_{1/2}^{\uparrow}$ (LS→HS) and in the cooling mode $T_{1/2}^{\downarrow}$ (HS→LS) will be different.

(d) Multi-step spin transition: In certain cases, the spin-crossover phenomenon occurs in one or more steps, as shown in Figure 1.8 d. This phenomenon may have different origins. Obviously, this phenomenon is expected to occur in crystals whose lattice contains metal ions in (at least) two different positions. In this case, the ligand field around the ions will be different and they will switch at different temperatures. Remarkably, however, stepped transitions have been also reported for systems containing metal ions in a unique crystallographic position. In such cases, the stepwise transition should arise due to a competition of interactions of opposed sign (favoring either the pure or the mixed forms) [Bousseksou 1992].

(e) Incomplete spin transition: Such curves correspond to residual high-spin molecules at low temperatures and residual low-spin molecules at high temperatures (see Figure 1.8e). This phenomenon may have different origins. Molecules in a metastable high spin state may be trapped at low temperatures due to the kinetic effects. An additional reason is that some heterogeneities (defects, surfaces/interfaces, etc.) in the lattice may stabilize locally the HS and/or LS species.

1.2.2. Different stimuli to induce the spin crossover

The energy necessary to induce spin crossover phenomenon can be harvested from external stimuli. Here, we introduce the most common stimuli: temperature, light irradiation and pressure [Gütlich 2004]. However, it is worth noting that spin transitions can be also induced by an intense magnetic field [Bousseksou 2002] and the adsorption of gas/vapor molecules [Ohba 2009] or by protonation [Kelly 2023].

1.2.2.1 Temperature-induced spin transition

The most common way to induce a spin transition is to change the temperature. If the system is considered to be composed of isolated, non-interacting molecules, a simple thermodynamic model can be used to describe the spin crossover as an equilibrium between two phases. For this particular system, the pressure and temperature of the sample are experimentally controllable parameters, so the pertinent thermodynamic function is the Gibbs free energy, G = H – TS, with H the enthalpy and S the entropy. At constant pressure, for a given temperature, the difference between the Gibbs free energies of the two spin states is

$$\Delta G = G_{HS} - G_{LS} = \Delta H - T\Delta S \qquad (2)$$

ΔH and ΔS are the enthalpy and entropy variations during the LS to HS transition, respectively. For a spin crossover system, both quantities are expected to be positive. This means that at low temperatures the ground state is the LS state. However, when the temperature increases the HS state gets stabilized due to its higher entropy. The latter stems primarily from electronic ΔS_{el} and vibrational ΔS_{vibr} contributions. To a good approximation, ΔS_{el} can be assimilated to the multiplicity change arising from the change of the total spin momentum, which is given (for the case of Fe^{II}) by:

$$\Delta S_{el} \approx \Delta S_{el}^{spin} = R \ln\left(\frac{2S_{HS}+1}{2S_{LS}+1}\right) = R \ln 5 = 13.38\ JK^{-1}mol^{-1} \qquad (3)$$

where R represents the ideal gas constant [Gütlich 1981]. However, heat capacity measurements on Fe(II) based SCO complexes show that ΔS takes values typically between 40 $JK^{-1}mol^{-1}$ and 80 $JK^{-1}mol^{-1}$ [König 1985; Sorai 1972]. Obviously, these values are much higher than ΔS_{el} and we can thus conclude that the remaining, and most important, contribution comes from the vibrational component ΔS_{vib}. The main reason behind this considerable change of the vibrational entropy is that during the transition from the low-spin to high-spin state, the metal-ligand bond becomes weaker, resulting in lower vibrational frequencies [Sorai 1974, Bousseksou 2000].

1.2.2.2 Light-induced spin transition

Light (X-ray, UV, visible or near-infrared) is another stimulus to induce spin crossover. We can devise two different light-induced phenomena: the LIESST effect (Light Induced Excited Spin State Trapping) and the LD-LISC effect (Ligand-Driven Light-Induced Spin Change).

The LIESST effect refers to the photo-excitation of the molecule in the low spin state (via either a metal-centered d-d transition or via a metal to ligand charge transfer transition), followed by its relaxation to the metastable HS state. This phenomenon was first reported by McGarvey in solution in 1982 [McGarvey 1982] and then by Decurtins et al. in 1984 in solid state and is mainly investigated in Fe(II) complexes [Decurtins 1984]. The Jablonski diagram in Figure 1.9 provides a scheme of the LIESST effect by taking an Fe(II) complex as an example [Hauser 1991]. Light with a wavelength of 530 nm is absorbed by the d-d absorption band of the LS state, bringing the metal ion from the ground $^1A_1$ state to the $^1T_1$ excited state. The latter has a very short lifetime (< 1 ps) [Brady 2004] and quickly relaxes to lower lying levels (the $^3T_1$ energy level in Figure 1.9) to reach finally the metastable HS state ($^5T_2$), where the molecule can be held for a longer time. Indeed, the lifetime can be longer than one week at 20 K, but in any case the molecule must be kept at cryogenic temperatures to remain trapped. (The lifetime of the metastable state at room temperature falls typically in the μs-ns range [Hauser 1991, Hauser 2004b].) As an example, Figure 1.10 shows LIESST experiments for the complex $[Fe(ptz)_6](BF_4)_2$ at 77 K including the population of the metastable HS state at different excitation conditions (Figure 1.10a) and the relaxation of this photogenerated state in the dark (Figure 1.10b) [Moritomo 2006]. In addition, since the $^3T_1$ energy level is lower than the ^5E level, the reversibility of the LIESST effect is possible. This reverse-LIESST effect was demonstrated first by Hauser in 1986 for the same compound [Hauser 1986]. The authors used near-infrared light with a wavelength of 820 nm to irradiated into the $^5T_2$ - ^5E absorption band of the high spin form of the molecule, which allowed them to re-populate the $^1A_1$ (LS) state (Figure 1.9).

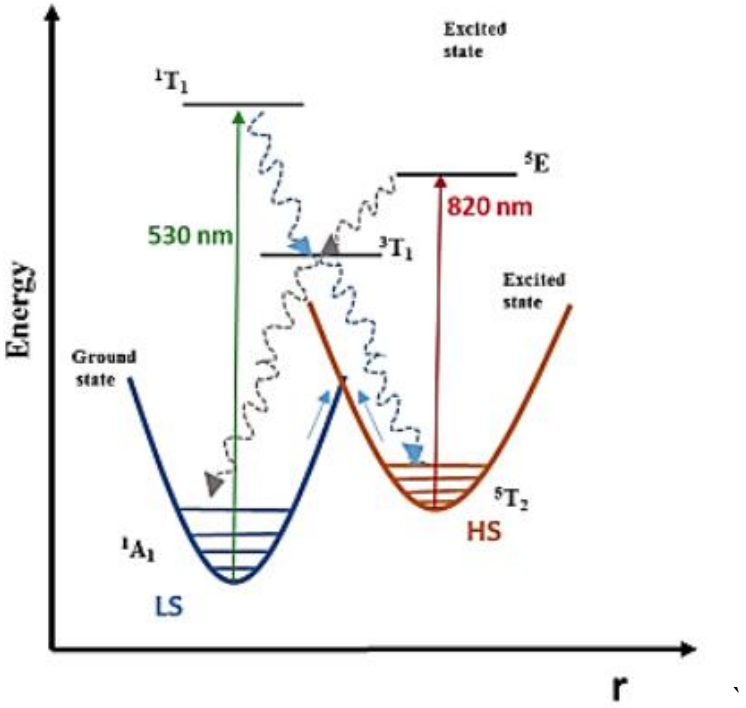

Figure 1.9. Jablonski diagram showing the LIESST and reverse LIESST effects: case of the $[Fe(ptz)_6](BF_4)_2$ complex [Hauser 1991].

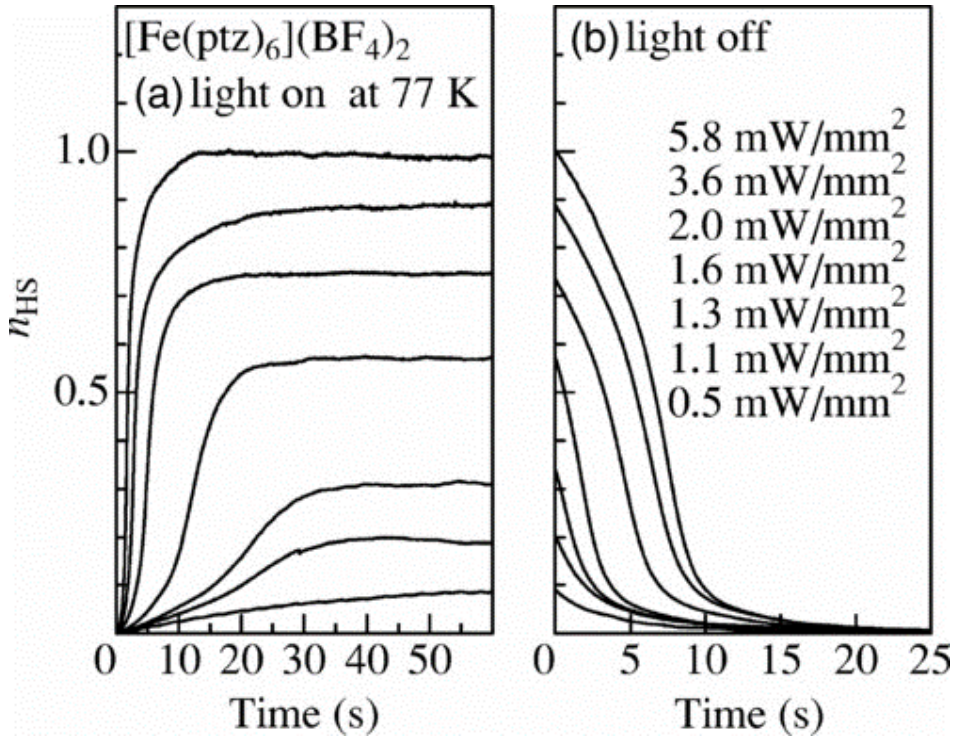

Figure 1.10. HS fraction of $[Fe(ptz)_6](BF_4)_2$ molecules as a function of time measured at 77 K during (a) photoexcitation with different power densities, followed by (b) relaxation in the dark [Moritomo 2006].

In contrast to the LIESST effect, LD-LISC phenomenon can occur at relatively high temperatures. The experimental observation of LD-LISC was first reported by Zarembowitch et al. in 1992 [Zarembowitch 1992]. This phenomenon can be observed for a few complexes containing photosensitive ligands. The conformation of the ligand is changed by a photochemical reaction, which results in the modification of the strength of the crystal field and ultimately it leads to the change of the spin state of the metal center [Zarembowitch 1993; Boillot 1999]. Figure 1.11 shows the example of the $[Fe(stpy)_4(NCBPh_3)_2]$ complex. In this molecule the ligand undergoes cis-trans isomerization under the action of light with a given wavelength [Boillot 2004]. It is worth noting that the wavelengths of the light required are different for the trans-to-cis and cis-to-trans transformations [Roux 1994]. The results show that $[Fe(cis\text{-}stpy)_4(NCBPh_3)_2]$ (C_c) remains in the high spin state at any temperature, whereas $[Fe(trans\text{-}stpy)_4(NCBPh_3)_2]$ (C_t) undergoes spin crossover between ~250 K and 140 K (Figure 1.12). This difference in magnetic properties is attributed to the stronger ligand field brought in by the trans-stpy ligands relative to the cis-stpy ligands. It should be noted, however, that the photoisomerization of the ligands is usually difficult in the bulk solid and, in practice, the LD-LISC effect is mostly efficient if the molecules are diluted in a polymer matrix.

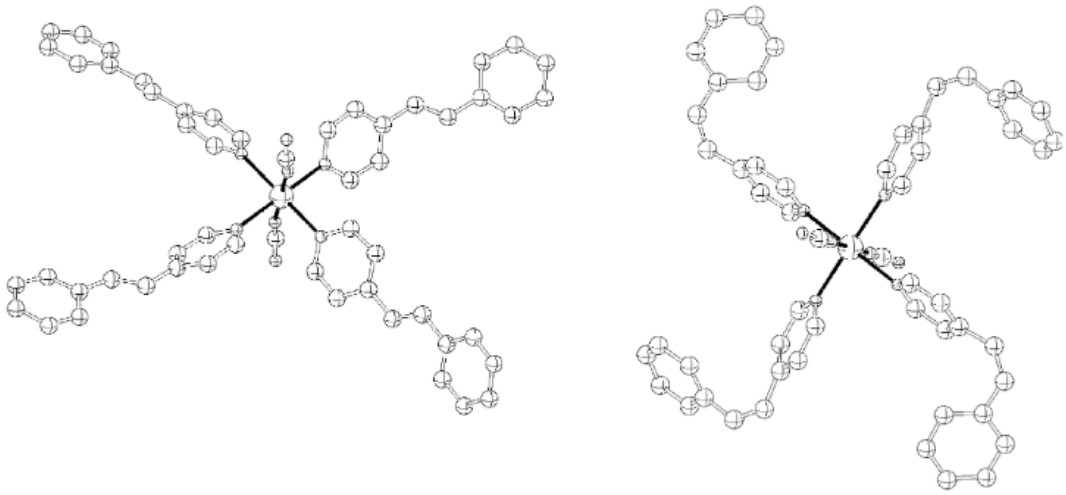

Figure 1.11. Molecular structures of $[Fe(trans\text{-}stpy)_4(NCS)_2]$ and $[Fe(cis\text{-}stpy)_4(NCS)_2]$. Hydrogen atoms were omitted for clarity [Boillot 2004].

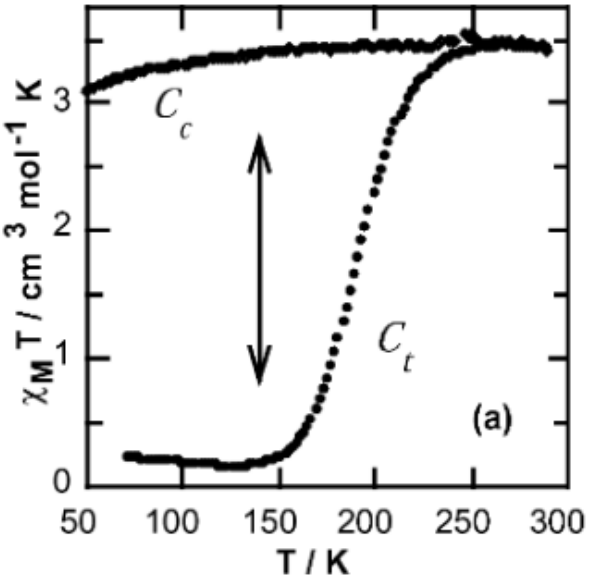

Figure 1.12. Temperature dependence of the magnetic susceptibility temperature product, $\chi_M T$, for polycrystalline samples of $[Fe(trans\text{-}stpy)_4(NCS)_2]$ and $[Fe(cis\text{-}stpy)_4(NCS)_2]$ C_t and $[Fe(stpy)_4(NCBPh_3)_2]$ C_c isomers [Boillot 2004].

1.2.2.3 Pressure-induced spin transition

Pressure-induced spin crossover has been reported less frequently than thermal and light-induced SCO phenomena, mainly because experiments under hydrostatic pressure are more difficult to conduct [Gaspar 2018]. The effect of pressure on the equilibrium of spin crossover was first reported for Fe(III)-dithiocarbamate complexes by Ewald et al in 1969 [Ewald 1969]. Subsequently, high-pressure investigations were conducted by many teams for various SCO complexes using piston-cylinder or anvil-type pressure cells coupled with various detection methods (Mössbauer, UV-Vis and IR spectroscopies etc.) [Drickamer 1982]. SCO complexes are very sensitive to the application of external pressure because of the large volume change between the two spin states ($\Delta V_{HL}=V_{HS}-V_{LS}$). A schematic representation of the pressure influence on the HS and LS potential wells of Fe(II) is shown in Figure 1.13 [Ksenofontov 2004]. By applying a 'moderate' pressure in the range of 0-1 GPa, the HS potential well is significantly displaced in the vertical direction with respect to the reference LS state, i.e. the energy gap between the two spin states increases by $p\Delta V_{HL}$. A displacement of the potential wells in the horizontal direction is also encountered due to the decrease of

the bond lengths with the increase of pressure, but this effect remains small in the pressure range of interest (< 1 GPa) and can be ignored in most cases. One shall note that the applied pressure not only increases the zero-point energy difference ΔE^0_{HL}, but leads also to the decrease of the energy barrier for the HS to LS relaxation ΔW^0_{HL}.

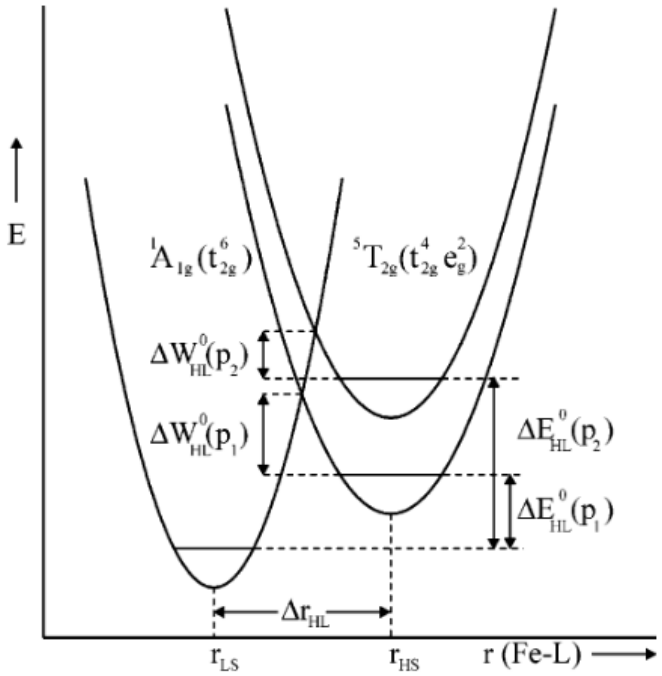

Figure 1.13. Schematic representation of the pressure influence (p_2>p_1) on the LS and HS potential wells of an Fe(II) complex [Ksenofontov 2004].

For Fe(II) complexes, under the action of external pressure, the equilibrium temperature of the spin crossover increases typically at a rate of 15-20 K/kbar. In addition, the spin crossover curves become more and more gradual and the width of the hysteresis loop (if any) decreases. A typical example is shown in Figure 1.14. It is worth noting that the influence of pressure on the spin-crossover phenomenon appears often more complex. Indeed, several 'anomalous' cases have been reported in the literature, such as increasing hysteresis width with increasing pressure [Gaspar 2018]. The origin of these anomalies remains often unclear, but it is generally accepted now that pressure may not only impacts the spin state equilibrium via the work term, but it may induce also additional structural changes to the lattice and its effect on the lattice dynamics may be also significant.

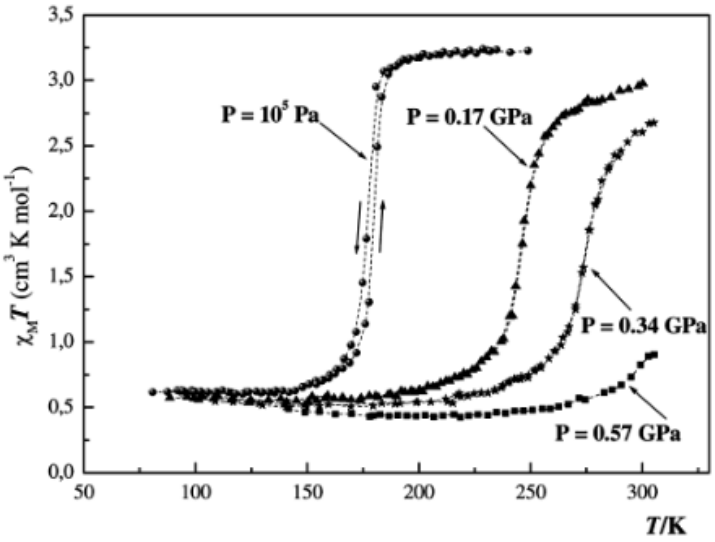

Figure 1.14. $\chi_M T$ versus T curves at different pressures for the compound $[Fe(phen)_2(NCS)_2]$ [Ksenofontov 2004].

1.3 Physical property changes at the SCO and associated characterization methods

Due to the strong electronic-lattice coupling, the spin crossover process is accompanied by changes in virtually all physical properties of the material (such as magnetic, optical, elastic, thermal properties etc.), so there are a series of corresponding experimental methods (such as magnetometry, electronic spectroscopy, mechanical testing, calorimetry, etc.) to detect spin crossover. In the following, we briefly overview the most common methods (magnetometry, calorimetry, crystallography and vibrational spectroscopy), followed by a more extensive discussion of optical properties and optical detection methods.

1.3.1 Changes and characterization of magnetic properties

During the spin transition phenomenon, the electrons of the metal ions rearrange such that the spin multiplicity changes between the lowest and highest possible values, resulting obviously in a change in the magnetic properties. The SCO can thus easily be detected by measuring the magnetic susceptibility of the material, which is also the most popular, 'standard' characterization method of bulk SCO solids. In the LS state, Fe(II) complexes are diamagnetic, and the magnetic susceptibility does not change (or changes very little) with temperature. However, in the HS state, the material is

paramagnetic, and the magnetic susceptibility changes significantly with temperature. The magnetic susceptibility of the material can be expressed as $\chi_m(T) = \gamma_{HS} \cdot \chi_{HS} + (1-\gamma_{HS}) \cdot \chi_{LS}$, where χ_{HS} and χ_{LS} are the magnetic susceptibilities of the material in the HS and LS states, respectively, and γ_{HS} is the mole fraction of the high spin state of the complex. According to the Curie law, for paramagnetic materials the product $\chi_m \cdot T$ is a constant. Therefore, usually the plot of χm*T versus temperature is reported for SCO compounds. As an example, Figure 1.15 shows the temperature dependence of the product $\chi_m \cdot T$ for a microcrystalline powder sample of the complex [Fe($H_2B(pz)_2$)$_2$(NH_2-phen)], revealing a nearly complete and gradual spin crossover centered near 154 K [Schleicher 2018]. (N.B. The expected spin-only values of $\chi_m \cdot T$ in the HS and LS states are 3.0 and 0 $cm^3mol^{-1}K$, respectively. The experimental values may sometimes deviate from these theoretical spin-only values due to other possible contributions to the overall magnetic response of the sample.)

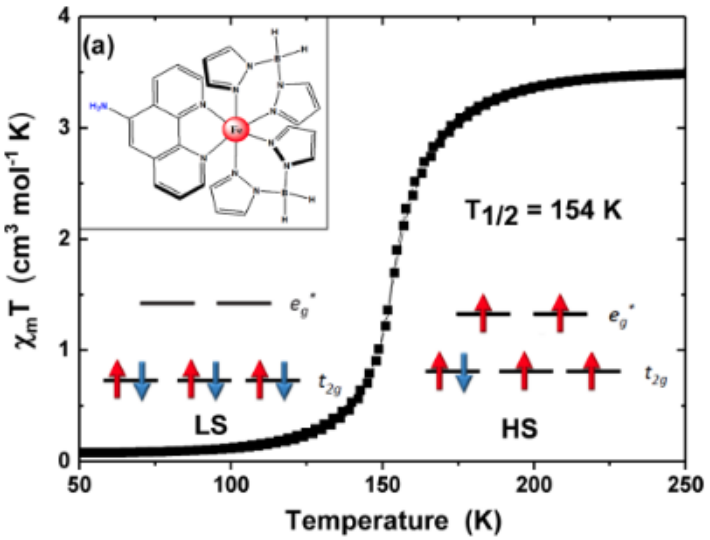

Figure 1.15. $\chi_m T$ vs T plot for the complex [Fe($H_2B(pz)_2$)$_2$(NH_2-phen)] and the corresponding electronic configurations [Schleicher 2018]. Note that the diamagnetic contributions to the magnetic susceptibility were subtracted.

1.3.2 Changes and characterization of thermal properties

As mentioned earlier, the thermally induced spin crossover is an entropy-driven process. Therefore the SCO phenomenon can be also characterized by measuring the heat

capacity changes – most often by means of differential scanning calorimetry (DSC) [Molnar 2019]. The first calorimetric measurement on an SCO material was reported by Sorai and Seki in 1972 for the compound $Fe(phen)_2(NCS)_2$ [Sorai 1972]. As shown in Figure 1.16, the heat capacity as a function of temperature displays an anomaly near 176 K in this compound. The relationship between the entropy change and excess heat capacity is given by $dS = \frac{Cp}{T} dT$, from which the entropy difference due to SCO was calculated as 48 $Jmol^{-1}K^{-1}$. In practice, however, instead of the relatively tedious heat capacity measurements, the DSC is used to measure the enthalpy of transformation, from which the entropy change is evaluated using equation 2.

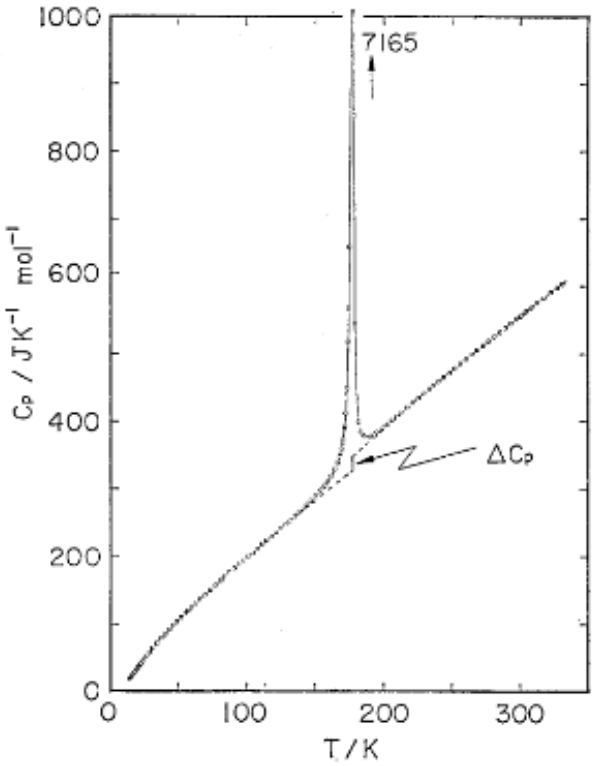

Figure 1.16. Temperature dependence of the heat capacity for $Fe(phen)_2(NCS)_2$ [Sorai 1972]. Note that besides the heat capacity anomaly due to the spin transition there is also a small difference in the "normal" heat capacities of the HS and LS forms.

1.3.3 Changes and characterization of the crystal structure

As mentioned before, during the spin crossover process, the metal-ligand bond lengths change drastically, leading also to a change of the unit cell parameters of the lattice.

This variation of the lattice is most often isostructural, but in some cases, it can be also coupled to a change of the space group. Single crystal and powder X-ray diffraction (XRD) techniques can therefore be used to characterize the SCO phenomenon. However, when conventional θ/2θ scanning methods are used to characterize SCO thin films, weak signals from the thin film and strong signals from the substrate are usually produced. To avoid this problem, a 2θ scan with a fixed grazing angle of incidence (called GIXRD) is adopted, resulting in enhanced thin film signals and reduced substrate signals. Since GIXRD provides signals only from crystal planes parallel to the substrate, one can easily depict the preferential orientation of the films (if any). As an example, Figure 1.17 shows the powder diffraction patterns of the compound [Fe(HB(1,2,4-triazol-1-yl)$_3$)$_2$]. Remarkably, the diffraction peak at 2θ = 10.11° in the low spin state, corresponding to the 002 reflection, shift to 2θ = 9.59° in the HS state, denoting a significant elongation of the lattice along the *c*-axis. Interestingly, the diffraction pattern of thin films of this compound exhibit only the 002 reflection, which means that the films are oriented with the c-axis normal to the substrate [Shalabaeva 2017a].

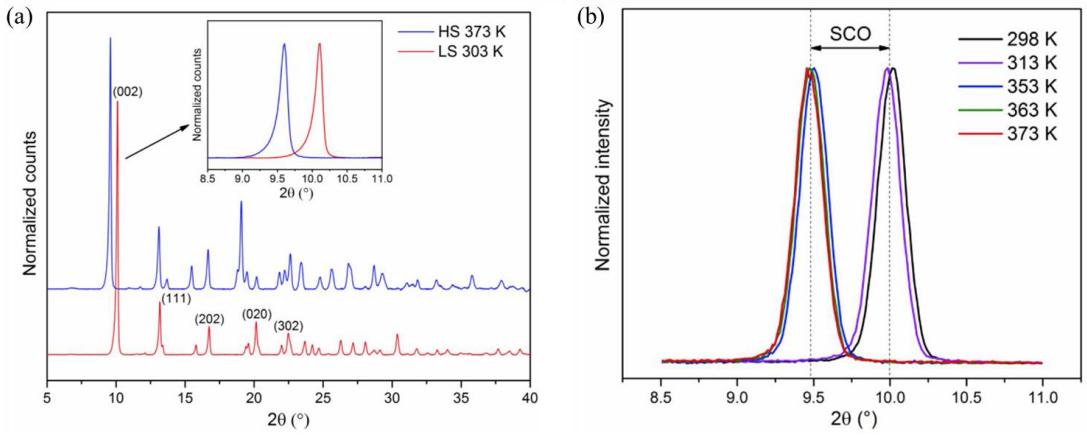

Figure 1.17. (a) PXRD patterns of the bulk powder [Fe(HB(tz)$_3$)$_2$] in the LS and HS states. (b) GIXRD patterns of a 194 nm crystalline film of [Fe(HB(tz)$_3$)$_2$] at different temperatures [Shalabaeva 2017a].

1.3.4 Changes and characterization of vibrational properties

The spin transition is accompanied by a change in the metal-ligand distance, resulting

eventually in a change of the metal-ligand vibrational frequencies. Table 1 depicts the metal-ligand stretching frequencies of some SCO complexes revealing indeed a significant increase (ca. 150-200 %) when going from the HS to the LS state.

Table 1. Fe-N stretching frequency changes upon SCO in selected iron(II) compounds. [Tuchagues 2004]

Compound	Fe-N stretching frequencies (cm^{-1})		ω_{LS}/ω_{HS}	Ref
	HS state	LS state		
$[Fe(X\text{-}bzimpy)_2](ClO_4)_2$ (X=H, OH, Cl)	220, 215, 212	436, 436, 436	2.0–2.1	23
$[Fe(X\text{-}bzimpyH_{-1})_2]$ (X=H, OH, Cl)	229, 217, 213	440, 436, 435	1.9–2.0	24
$[Fe(ptz)_6](BF_4)_2$	167, 231	261/279, 412	1.6, 1.8	25
$[Fe(phen)_2(NCS)_2]$	220, 252	368, 376	1.7, 1.5	18
$[Fe(phen)_2(^{15}N^{13}CS)_2]$	220, 248	368, 374	1.7, 1.5	19
$[Fe(phen)_2(NCSe)_2]$	218	363	1.7	14
$[Fe(bpy)_2(NCS)_2]$	235	384	1.6	16
$[Fe(HB(pz)_3)_2]$	223, 258	400, 434	1.8, 1.7	26
$[Fe(CH_3O\text{-}phen)_3](ClO_4)_2{\cdot}H_2O$	227, 237	341, 352	1.5	27
$[Fe(tpa)(NCS)_2]$	241, 242, 284	344, 375, 424	1.5	22
$[Fe(pz)(M(CN)_4)]{\cdot}2H_2O$ (M: Ni, Pd, Pt)	231, 223, 226	394, 390, 402	1.7–1.8	11
$[Fe(py)_2(M(CN)_4)]$ (M: Pd, Pt)	217, 221	383, 395	1.8	11

Vibrational spectra are mainly obtained by measuring infrared absorption and Raman scattering spectra. For infrared absorption experiments, however, the materials need to be ground, squeezed, etc. during the sample preparation process, which might also alter the SCO properties. This problem is avoided in Raman spectroscopic experiments, which provides the ability to detect samples in various states (crystals, powders, films, solutions) without any sample preparation. It is worth noting that Raman laser heating effects have an impact on the measurement of highly colored samples, so it is really essential to choose the appropriate excitation wavelength. In practice, it is not always obvious to detect and/or identify the metal-ligand stretching vibrations in the vibrational spectra of SCO complexes. Nevertheless, the vibrational fingerprints, which are always different to some extent in the two spin states, can be conveniently used to track the SCO process. Figure 1.18 shows the example of a crystalline film of $[Fe(HB(tz)_3)_2]$, whose Raman spectrum shows obvious differences both in intensity and

in peak positions during the spin state switching around 338 K [Shalabaeva 2017a].

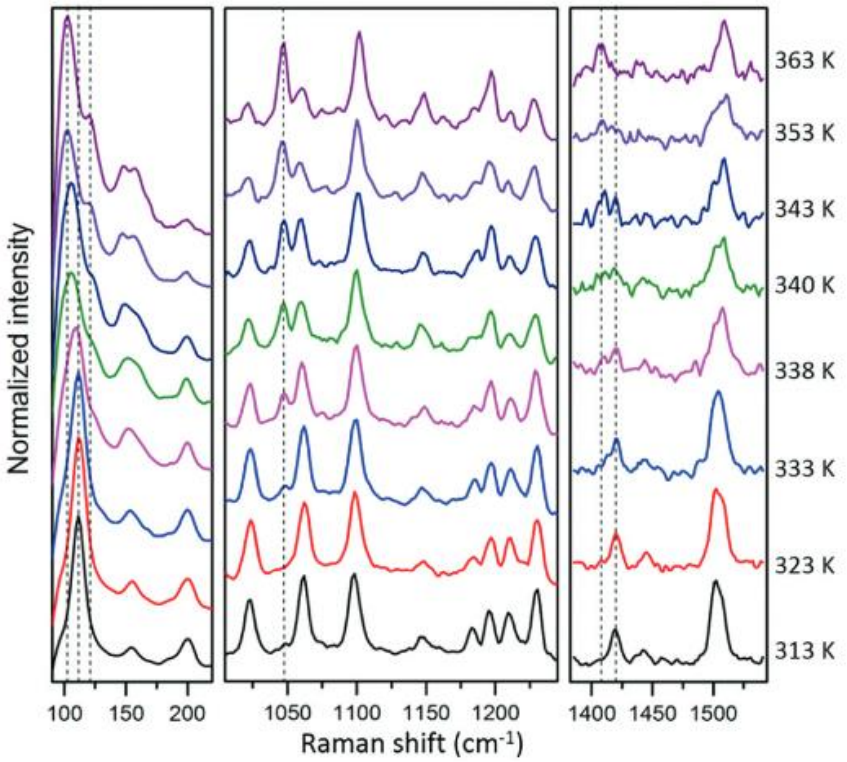

Figure 1.18. Raman spectra of a 194 nm thick crystalline film of $[Fe(HB(tz)_3)_2]$ acquired at different temperatures in the heating mode [Shalabaeva 2017a].

1.4 Changes and characterization of optical properties

1.4.1 Changes in the optical absorption properties

Another appealing feature of the spin transition is the concomitant change in the optical absorption properties of the material. This happens obviously because the change of the electronic state (between HS and LS) results inevitably in a change of all metal-centered ligand field transitions and one expects significant modification of the metal-to ligand and ligand-to-metal charge transfer transitions as well. As a consequence, one of the most striking (and well-known) aspects of the spin transition is the dramatic color change of the material, a property which is referred as thermo-, photo- or piezo-chromism, depending on the stimuli used [Hauser 2004b]. As an example, Figure 1.19 displays the absorption spectra of a single crystal of the compound $[Fe(ptz)_6](BF_4)_2$ in the two spin states, as well as photographs of the crystal showing the corresponding

color change, from pink in the LS state to colorless in the HS state. In detail, in the LS state, the spectrum shows two ligand-field absorption bands, $^1A_1 \rightarrow {}^1T_1$ and $^1A_1 \rightarrow {}^1T_2$, the former appearing in the visible (18500 cm^{-1}, $\lambda \approx 540$ nm) while the latter in the ultraviolet region (26500 cm^{-1}, $\lambda \approx 375$ nm). Consequently, as the crystal in the LS state mainly absorbs in the green, it appears in the complementary color, i.e. pink. When switching the crystal into the HS state, the spectrum shows only one ligand-field absorption band in the near-infrared (NIR) region (11800 cm^{-1}, $\lambda \approx 850$ nm), arising from the $^5T_2 \rightarrow {}^5E$ transition, while no significant absorption occurs in the visible range, which explains why the crystal appears colorless.

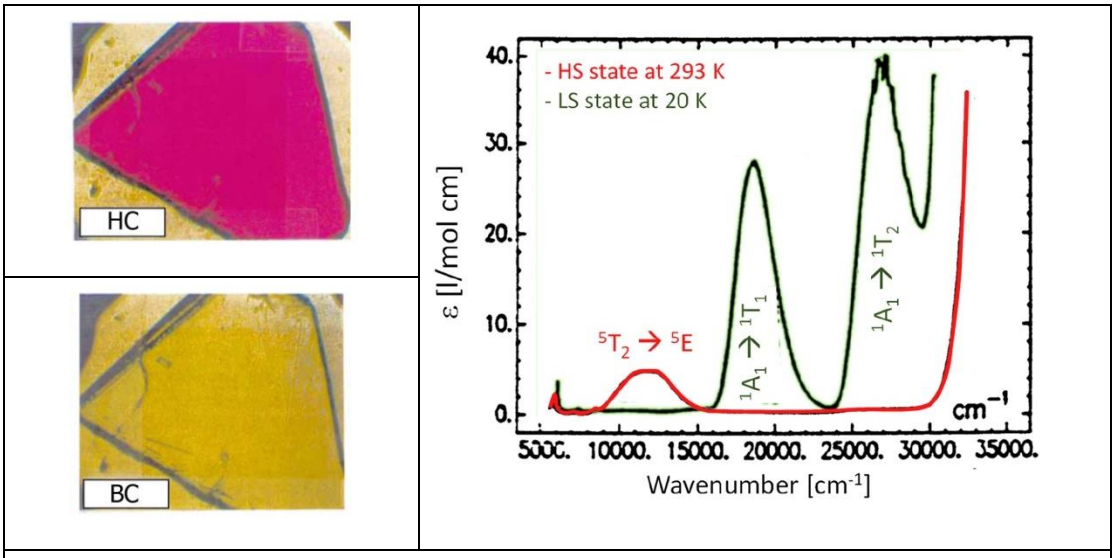

Figure 1.19. Pictures of a single crystal of $[Fe(ptz)_6](BF_4)_2$ at 20 K (top, LS state) and at 293 K (bottom, HS state), and the corresponding single-crystal optical absorption spectra [Hauser 1991].

The extinction coefficients associated with these ligand-field absorption bands in the Vis-NIR spectral region, are generally relatively low (typically in the range of α = 10–100 cm^{-1}) because these d-d transitions are forbidden by the selection rules of Laporte. However, it is worth to mention that more intense charge-transfer (metal-to-ligand or ligand-to-metal) bands ($\alpha = 10^4$–10^5 cm^{-1}) generally appear in the UV range [Hauser 2004b], and exhibit a pronounced spin-state dependence (generally a displacement to higher energy for the HS species). This blueshift of the charge-transfer bands arises from a larger metal-ligand bond length in the HS state, which results in a poorer overlap

between metal-centered and ligand-centered orbitals as compared to the LS state. For some compounds, such intense charge-transfer transitions may also appear in the visible range. These absorptions mask the weaker ligand-field transitions and make the compound highly colored, at least in one spin state. This is for example the case of the compound $[Fe(pic)_3]Cl_2 \cdot EtOH$ (pic=2-picolylamine), whose absorption spectrum in the LS state is dominated by an MLCT band around 480 nm, which is several orders of magnitude more intense (of the order of 10^4 l mol^{-1} cm^{-1}) than is typical for ligand-field transitions (Figure 1.20).

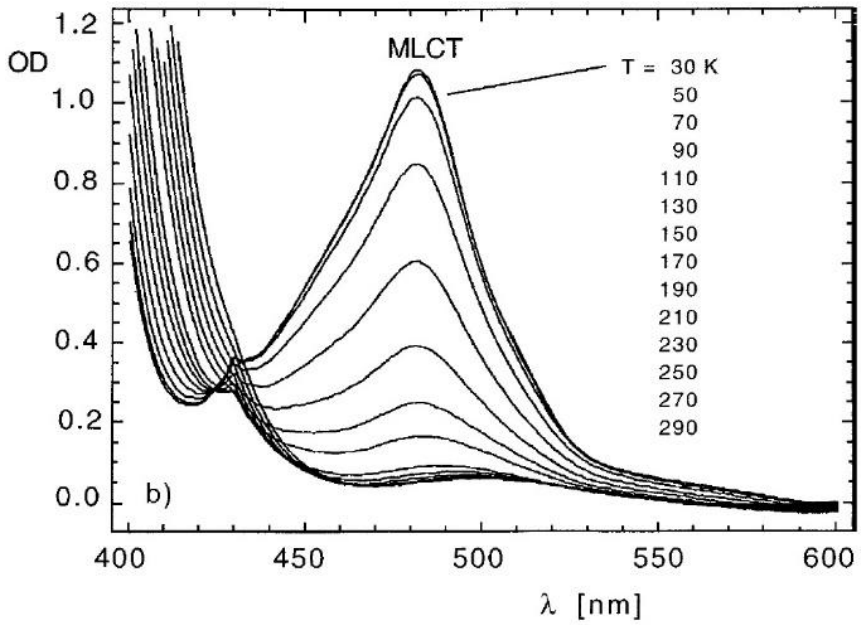

Figure 1.20. Variable temperature single-crystal absorption spectra of the compound $[Zn_{1-x}Fe_x(pic)_3]Cl_2 \cdot EtOH$ (x = 0.0005) [Vef 1994].

Based on this color-change property, a common way to quantitatively characterize the spin-transition phenomenon in non-opaque, homogeneous (with low scattering) SCO samples, such as single crystals, thin films or transparent solutions, is to measure the optical transmittance T – or the derived quantity called absorbance (or optical density) $A = -\log_{10}(T)$ – across the sample, in the UV-Vis-NIR spectral domain using a spectrophotometer. Indeed, according to the Beer-Lambert law, as A is proportional to the concentration of absorbing species within the sample, the absorbance measured at a well-chosen wavelength scales with the fraction of LS or HS molecules. Based on this

principle, time-resolved optical microscopy has recently emerged as a powerful, non-invasive imaging tool for the real-time observation of the spatiotemporal dynamics of the spin transition in SCO single crystals [Ridier 2017]. Optical absorption measurements enabled also monitoring with a sub-picosecond time resolution the switching dynamics in single crystals [Lorenc 2009], nanoparticles [Bertoni 2016] and nanometric SCO films [Ridier 2019]. As shown in Figure 1.21, fs laser excitation of a thin film of $[Fe(HB(tz)_3)_2]$ at room temperature, allows to photoswitch ca. 1-3 % of LS molecules to the HS state. The HS fraction remains then constant up to ca. 1-10 ns. Then, depending on the excitation energy, temperature and film thickness, the photoswitched molecules either return to the LS state within a few hundreds of ns, or alternatively an additional, thermally-activated increase of the HS fraction occurs at the timescale of a few tens of ns, which is then followed by relaxation to the LS state on the µs time scale [Ridier 2019]. Overall, these result highlight an ultrafast (<ps), though moderately efficient (< 5 %), light-pulse-induced switching in SCO films, followed by a relaxation on the sub-µs timescale, denoting a potential for optical modulation with >MHz bandwidths.

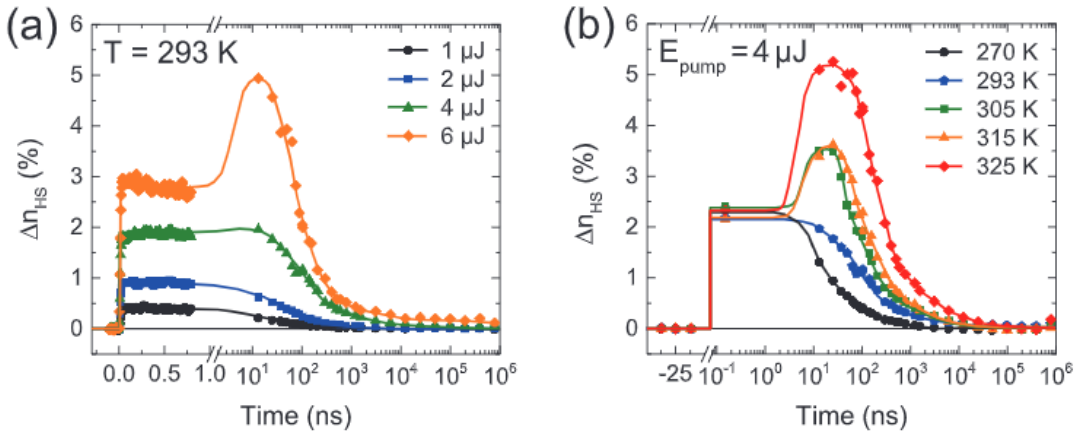

Figure 1.21. Photo-response of the thin films of $[Fe(HB(tz)_3)_2]$ on the ps–ms time range. (a) Time evolution of Δn_{HS} at room temperature in a 100 nm thick film following a femtosecond laser pulse excitation with various energies. (b) Time evolution of Δn_{HS} in the same film following a 4 µJ laser pulse at various temperatures between 270 and 325 K [Ridier 2019].

The first optical device using SCO compounds was developed by Kahn et al. for

information storage and display applications in the 90ies. The compound $[Fe(NH_2trz)_3](NO_3)_{1.7}(BF_4)_{0.3}$ was synthesized by a "molecular alloy" approach, which consists of using a mixture of counter-anions (or alternatively a mixture of ligands) with the aim of fine-tuning the spin transition temperature. The evolution of the transmittance of this compound as a function of the temperature (see Figure 1.22a) shows a ca. 60 K wide hysteresis loop centered around room temperature. Importantly, the hysteresis loop was reproducible over several dozen of thermal cycles. Then, display devices were fabricated using this spin-transition compound as an optically active material (see Figure 1.22b). Before writing (LS state), the material is violet, due to a ligand-field absorption around 520 nm. However, when the system is switched to the HS state, the material turns white. To store the information, the system needs to be kept at a temperature within the hysteresis loop; to erase the signal, the system must be cooled down, which can be achieved with a Peltier element. [Kahn 1992; Kahn 1998]

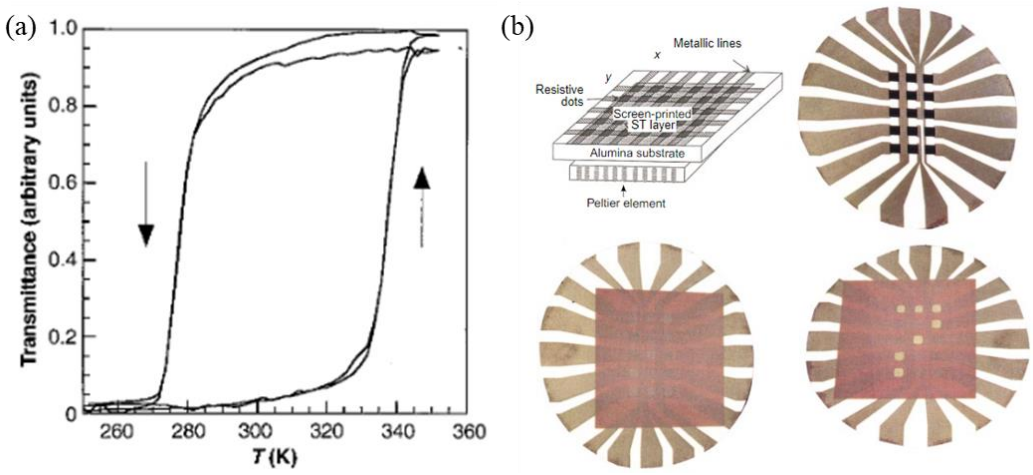

Figure 1.22. (a) The evolution of transmittance with temperature at 520 nm for the compound $[Fe(NH_2trz)_3](NO_3)_{1.7}(BF_4)_{0.3}$ encapsulated in a polymer. (b) A reversible display based on the SCO phenomenon. The substrate consists of an alumina plate, on which resistive dots and connecting electrodes were previously screen printed. A layer of the active material is deposited on the substrate. This is done by screen-printing technology, using an ink consisting of the material in suspension in a resin (bottom left). The dots, when electrically addressed, act as heat dissipators. [Kahn 1998]

These pioneering devices were using microcrystalline samples and were based on absorbance readout and thermal addressing, which are conceptually contradictory

principles in terms of device size. As discussed above, due to the low absorption coefficient of SCO compounds in the Vis-NIR range, and as the optical absorbance is inversely proportional to the optical path length, the optical contrast between the two spin states often becomes extremely low at nanometric sizes. Thus, in this spectral range, this incompatibility between nanometric size and optical contrast constitutes a significant impediment for the development of applications based on optical absorption change. To illustrate this shortcoming, the expected change of absorbance in a 100-nm-thick film associated with a ligand-field band ($\Delta\alpha_{SCO} \approx 100$ cm^{-1}) is typically of the order of $\Delta A_{SCO} \approx 10^{-3}$, which is close to the detection limit achieved using standard, commercial variable-temperature spectrophotometers. On the other hand, it is often possible to detect and characterize the spin transition in such nanometric samples by probing charge-transfer bands (mainly in the UV range), which, in most cases, display sufficiently large variations in absorbance ($\Delta A_{SCO} \approx 0.1$ for 100 nm film thickness), but the UV domain is considered less relevant for photonic applications.

1.4.2 Changes in the refractive index

In addition to the change of the imaginary part (extinction coefficient) k of the complex refractive index $n^* = n + ik$, directly associated with the optical absorption change, the SCO phenomenon is also accompanied by a significant change of the real part n [Hauser 1993]. This change of the real part originates both from the change of the absorption properties of the material (i.e., the electronic polarizability of the molecules), especially for wavelengths in the vicinity of intense charge-transfer bands, but also from structural effects associated with the density (volume) change of the material upon the transition. Importantly, the volume change has the effect of modifying the refractive index over the whole optical spectral range and, thus, it becomes the dominant effect in the non- (or weakly-) absorbing spectral regions. Indeed, in the Vis-NIR region (i.e., away from any intense charge-transfer bands), the available experimental data show that the refractive index is consistently found to decrease by *ca.* 0.01–0.1 when going from the LS to the HS state [Molnar 2018]. These observations agree with the empirical Gladstone-Dale relation

$$\frac{\Delta n}{1-n} = \frac{\Delta V}{V} \quad (4)$$

which predicts a decrease of the refractive index in the range 0.01–0.1, as observed experimentally, due to the relative volume change, $\Delta V/V$ = 1–10 %, accompanying the LS-to-HS transition. This change of n can be detected in a straightforward manner by a variety of photonic methods, such as optical reflectivity [Ridier 2020], optical diffraction [Akou 2012], ellipsometry [Loutete-Dangui 2007], or surface plasmon resonance (SPR) spectroscopy [Félix 2011].

Up to now, only a few studies were dedicated to the refractive index switching of SCO compounds in the optical region. These investigations aimed either to use photonic principles to detect the occurrence of spin crossover phenomenon (sic 'photonics for SCO') or, the other way around, use the switchable optical properties of SCO molecules in active photonic devices (sic 'SCO for photonics'). To our best knowledge, the first investigation of refractive index changes at the SCO was reported by Hauser [Hauser 1993], who studied transient phase gratings, generated by means of four-wave-mixing, in single crystals of the compound $[Zn_{0.9}Fe_{0.1}(ptz)_6](BF_4)_2$. He concluded that the observed refractive index change reflects primarily the mass density change brought into by the spin-state switching. The first photonic device, a tunable Bragg filter, was constructed using a microcrystalline powder sample of $[Fe(NH_2\text{-}trz)_3]Br_2{\cdot}H_2O$ and operated in the sub-millimeter wavelength range [Mounaix 2006]. The optical properties of the same compound (in pellet form) were assessed in the UV-VIS range by spectroscopic ellipsometry, revealing a refractive index increase of $\Delta n = n_{LS}\text{-}n_{HS} \approx$ 0.06 in the VIS when going from the HS to the LS state (see Figure 1.23) [Loutete-Dangui 2007]. This refractive index change could be then exploited to detect the occurrence of SCO at the single particle level using differential interference microscopy (DIC) [Arnaud 2009] and surface plasmon resonance microscopy (SPRM) [Liu 2020]. Particles of $[Fe(NH_2\text{-}trz)_3]Br_2$ were also investigated in microemulsions and a refractive index change from 1.63 (HS) to 1.76 (LS) was assessed at 550 nm [Iazzolino 2015].

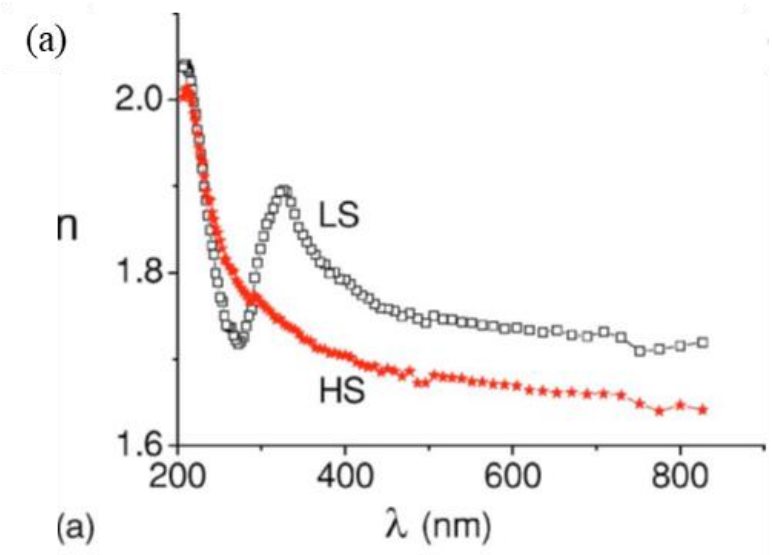

Figure 1.23. (a) Wavelength dependence of the real part of the refractive index *n* in the HS state (353 K) and in the LS state (263 K) for a pellet of the sample $[Fe(NH_2\text{-}trz)_3]Br_2$. [Loutete-Dangui 2007]

Overall, these studies highlight that the possibility to modulate the refractive index via the SCO phenomenon opens up interesting prospects for manipulating light propagation. To integrate photonic devices, however, it is necessary to work with high quality, low-loss SCO films over large area and thickness ranges, which should be also patterned in order to enlarge the scope of their integration into different types of devices (waveguides, resonators, gratings, etc.). From this perspective, nanometric thin films of the compound $[Fe(hptrz)_3](OTS)_2$ have been studied using high sensitivity refractive index sensing methods, such as surface plasmon resonance (SPR) spectroscopy [Félix 2011], optical diffraction [Akou 2012] and localized surface plasmon resonance (LSPR) spectroscopy [Akou 2013], revealing consistently a refractive index change of $\Delta n \approx 0.01$. For example, SPR spectroscopy – due to its high sensitivity to refractive index change – has shown to be extremely promising for detecting and investigating the SCO in ultrathin films (< 10 nm) [Félix 2011], i.e., at a size scale where most laboratory characterization techniques fail. Surface plasmon polaritons (SPPs) are guided electromagnetic waves propagating at the interface between metal and dielectric layers under the excitation of light, which can be coupled to the impinging light by means of a prism (see Figure 1.24a).

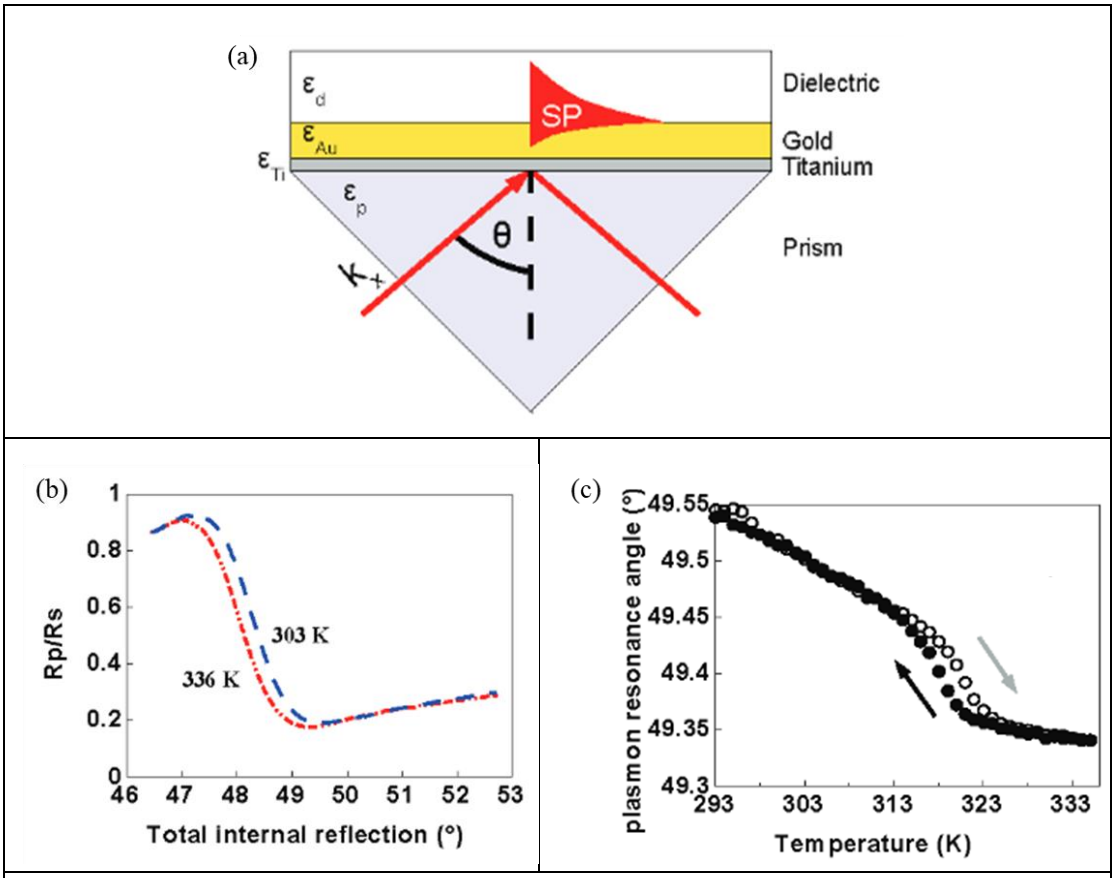

Figure 1.24. (a) Scheme of the multilayer glass/Ti/Au/SCO setup. (b) Angle-dependent reflectance spectra of a glass/Ti (5 nm)/Au (45 nm)/$[Fe(hptrz)_3](OTs)_2$ (30 nm) multilayer at 303 K (LS state) and 336 K (HS state) (λ= 660 nm). Rp and Rs refer to reflectance of p- and s-polarized light, respectively. (c) Temperature dependence of the plasmon resonance angle (reflectance minima) of the multilayer in the heating and cooling modes (dT/dt= 2 K/min) [Félix 2011].

A multilayer sample, consisting of glass/Ti (5 nm)/Au (45 nm)/$[Fe(hptrz)_3](OTs)_2$ (30 nm) was fabricated. The angular reflectivity spectra showed obvious shift of the "SPR dip" (the corresponding angle is called the "plasmon resonance angle",θ_{SPR}) in the LS and HS states (see Figure 1.24b). The temperature dependence of the θ_{SPR} revealed a spin transition around 320 K accompanied by a ~3 K hysteresis loop (see Figure 1.24c). The shift of plasmon resonance angle was attributed to the refractive index change using transfer matrix calculations [Félix 2011]. Based on this refractive index change, an active, photothermal tuning of the LSPR resonances by ca. 6 nm was demonstrated for a gold nanopattern coated with a $[Fe(hptrz)_3](OTs)_2$ film [Abdul-Kader 2013]. Later, making use of the higher refractive index change in the complex $[Fe(Htrz)_2(trz)]BF_4$,

LSPR resonance modulation up to ca. 35 nm could be achieved [Palluel 2020]. Refractive index sensing was also implemented in SCO-based gas sensors, wherein lithographically patterned diffraction gratings of the compound {Fe(bpac)[M(CN)$_4$]} were developed to assess ppm level concentrations of volatile organic compounds [Bartual-Murgui 2015].

Since the real part of n^* plays an important role in optical phenomena at interfaces (e.g., reflection, refraction, diffraction), the possibility to modulate n via the SCO opens up interesting prospects for manipulating light propagation at optical interfaces, and more generally for photonic applications, which aim at achieving independent control of the phase and amplitude of travelling light waves. In this context, and as mentioned above, an appealing characteristic of many SCO materials is their low optical absorption losses in both spin states in a large (Vis-NIR) spectral range, which therefore implies a small change in the absorption coefficient ($\Delta\alpha$ < 100 cm^{-1}) and in the associated extinction coefficient ($\Delta k \leq 10^{-3}$-10^{-4}) of the material upon the spin transition. As a result, a widely used figure of merit (FOM), which characterizes the decoupling of refractive index and absorption losses changes, can be given as:

$$FOM1 = \frac{\Delta n}{\Delta k} \tag{5}$$

Δn and Δk being, respectively, the change of the real and imaginary parts of refractive index induced by the phase transition, can typically reach FOM values between 10-1000 for SCO materials in the whole Vis-NIR range. This characteristic makes SCO compounds particularly promising as optical phase-change materials (O-PCM) for a large variety of applications, such as low-loss optical switches, modulators, beam steering, and so forth. With this idea in mind, in the next chapter we present different optical resonators incorporating SCO molecules, used for resonance tuning in the visible spectral range. Then, in the third chapter, we come back to the investigation of absorbance changes, but in a fundamentally new context, wherein the molecular absorbance is used to achieve tunable strong light matter coupling of SCO molecules to cavity resonances.

CHAPTER 2: Tunable multilayer optical resonators based on SCO refractive index switching

Chapter 2: Tunable multilayer optical resonators based on SCO refractive index switching

In this Chapter, utilizing the change of the real part of the refractive index accompanying the spin-transition phenomenon, we aim to demonstrate the possibility of using thin films of SCO materials as active elements in tunable optical devices operating in the visible wavelength domain. In particular, two SCO-based optical resonators, with different geometries, were considered and investigated. The first resonator is a multilayer Fabry-Perot cavity in which the SCO layer is sandwiched between two Ag mirrors, while the second is an Ag/SCO bilayer resonant structure excited using a coupling prism (operating in total internal reflection (TIR) conditions). The spectroscopic characteristics of these SCO-based resonators were investigated as a function of the incident angle and temperature (i.e. spin state), and their thermal tunability was characterized using selected figures-of-merit. To carry out these investigations, we selected the SCO compound $[Fe(HB(1,2,4\text{-triazol-1-yl})_3)_2]$ which has the advantages of exhibiting an extremely robust and reproducible spin transition above room temperature, and which is a sublimable complex under vacuum, meaning that it can be deposited in the form of high-quality, homogeneous thin films by vacuum thermal evaporation.

2.1 Phase change materials for active optical devices

In the vast fields of optics and photonics, tunability, reconfigurability and adaptability are major assets, which are highly demanded for various applications [Kang 2019; Ko 2022]. These include, for example, displays, optical memories, spatial light modulators (SLMs), photonic integrated circuits (PICs), optical neural networks, and other approaches for optical computing. Notably, there has been recently an explosion of interest in active functionalities for a controlled modification of the phase and/or the amplitude of optical wavefronts in SLMs (e.g., beam steering, holographic displays, distortion correction) [Efron 2001], or for routing light through PICs (e.g., optical

switches, modulators, filters, limiters) [Coldren 2012].

Fundamentally, there are two ways to achieve active or adaptive optical properties, which comprise (i) changing the geometry of the structure by mechanical displacement(s) (e.g. micro mirrors, deformable mirrors), and (ii) using materials with controllable refractive indices. The latter strategy calls, self-evidently, for materials, displaying large changes of their dielectric function in response to an external stimulus (e.g. heat, voltage bias or light irradiation). This is readily observed in a number of materials exhibiting electro/thermo/photo-refractive properties. In practice, the most widespread approaches are based on liquid crystals, charge injection into semiconductors, Pockels cells and ordinary thermoreflectance phenomena [Ko 2022].

More recently, a particular attention has been focused on compounds, which undergo electronic and/or structural phase transitions, coined as phase change materials (PCMs) [Yang 2011; Karvounis 2016; Stegmaier 2016; Miller 2017; Miller 2018; Ryckman 2012; Williams 2020]. (N.B. It is worth to note here that in different scientific communities, the term PCM may refer exclusively to chalcogenide alloys, or to materials used for latent heat storage, but here we use it for all kinds of solid-solid phase transitions.)

Among the different PCM families, the technologically most relevant materials are chalcogenide alloys, whose main application field is the rewritable optical storage technology, such as CD-RW, DVD-RW and Blu-ray discs [Zuliani 2015; Wuttig 2017]. For example, the prototypical PCM chalcogenide alloy, the compound $Ge_2Sb_2Te_5$ (GST), can be switched reversibly from an optically transparent and electrically resistive amorphous state to an optically opaque and electrically conductive crystalline state (see figure 2.1a) [Williams 2020]. The two states are non-volatile as switching in both directions requires energy input, which can be achieved by heating the material with current or laser pulses to different temperatures (ca. 150 and 600 °C) [Raoux 2010]. As an example, Pernice et al. fabricated a GST-based integrated optical memory element, in which GST was deposited on a microring resonator coupled to nanophotonic waveguides (see figure 2.1b). The transition of GST from the amorphous

to the crystalline state results in a change in transmittance from 0 % to 90 % and an extinction ratio of more than 10 dB in the NIR spectral region (see Figures 2.1c and 2.1d), which is mainly due to the change in the degree of crystallization of GST, accompanied by changes in the refractive index and the material absorption. The reversibility of the device requires reamorphization of the crystalline GST, which is achieved by heating the device above the crystallization temperature, followed by rapid quenching. Note that the ultimate speed is determined by the thermal relaxation time. In summary, the device presents an all-optical, but photothermally operated non-volatile memory [Pernice 2012].

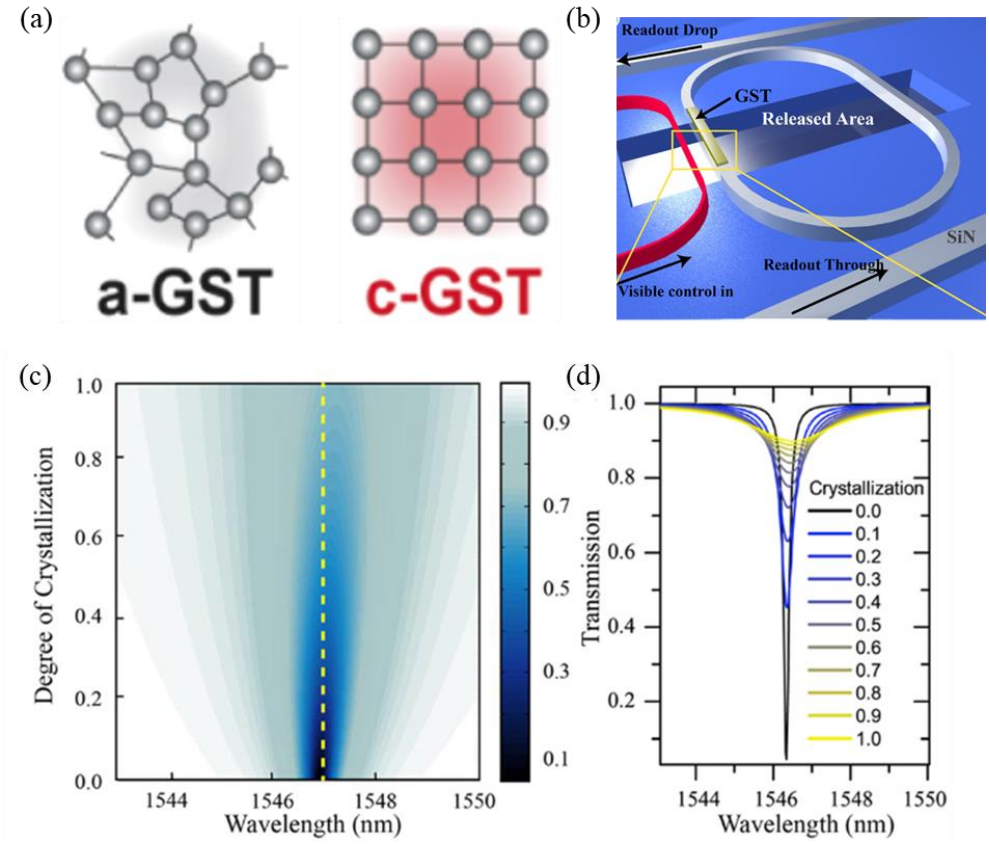

Figure 2.1. (a) Schematic structures of $Ge_2Sb_2Te_5$ (GST) in the amorphous (A) and crystalline (C) phases [Williams 2020]. (b) Schematic overview of the proposed GST-based integrated optical memory element. Light from a control port (red) is coupled evanescently to the ring resonator to perform the switching operation of the GST through photothermal heating. (c) The calculated transmission past the ring resonator as a function of the wavelength and the degree of crystallization of the GST. (d) The transmission at the cross-sectional line in (c), showing the increase in transmission as the ring shifts into the weakly coupled regime [Pernice 2012].

This non-volatility is indispensable for applications in optical memories, but becomes a less desired asset in some other applications, such as signal modulation. More recently, transition metal oxides displaying metal-insulator transition have been also considered in the 'active photonics' context [Liu 2017]. The prototype example, VO_2, exhibits concomitant electronic and structural transitions from an optically transparent, electrically insulating monoclinic form to an optically opaque, electrically conducting tetragonal structure around 68 °C (depending on the stoichiometry) (see Figure 2.2a). In ambient conditions, the tetragonal structure is volatile, making VO_2 appealing for low-power signal modulation [Haglund 2015].

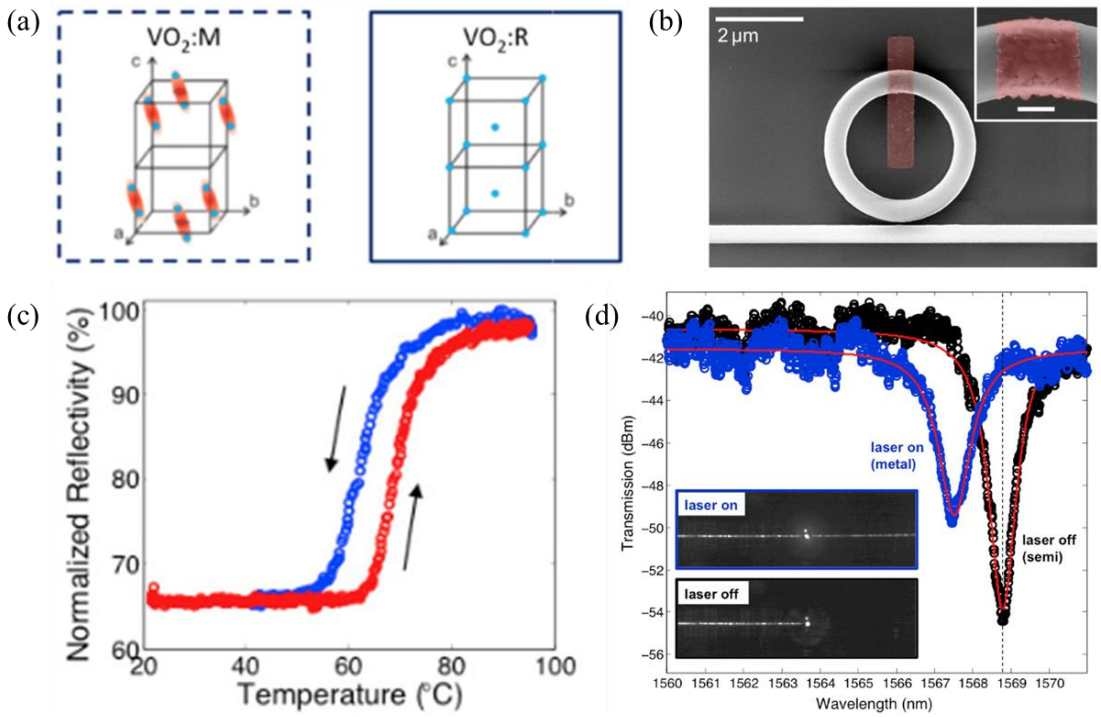

Figure 2.2. (a) Schemes of the low temperature, monoclinic (left) and high temperature, rutile (right) crystal structures of VO_2 [Miller 2018]. (b) Scanning electron microscopy image of a hybrid Si-VO_2 micro-ring resonator with 1.5 μm radius. The lithographically placed VO_2 patch is highlighted in false-color. (Inset scale bar is 250 nm). (c) White-light reflectivity versus temperature data for the 70-nm-thick VO_2 film. (d) Optical transmission of the 1.5 μm radius hybrid Si-VO_2 ring resonator as a function of wavelength, before and after triggering the phase transition with a 532 nm pump laser. Inset: IR camera images revealing ON/OFF switching of light propagation at a fixed probe wavelength of λ = 1568.78 nm [Ryckman 2012].

For example, photothermally induced optical switching of ultra-compact hybrid Si-VO_2 ring resonators was reported by Ryckman et al. [Ryckman 2012]. The device consists of a ~560 nm-long and ~70 nm-thick patch of VO_2 straddling a small portion of the silicon ring with a radius of 1.5 µm. Its scanning electron microscopy image is shown in Figure 2.2b. The reflectivity of the 70-nm-thick VO_2 film deposited on Si(100) substrates as a function of temperature (see figure 2.2c) demonstrates a dramatic change in reflectance accompanied by a hysteresis loop around 63 °C due to the insulator-to-metal transition of VO_2. The transmission spectra of the hybrid Si-VO_2 ring resonator are shown in figure 2.2d, where the black curve shows the transmission spectrum when VO_2 is in the insulating state. When switching the material to the metallic state (by a 532 nm laser), the resonance wavelength displayed a sizeable shift of $\Delta\lambda$ = -1.26 nm and an associated optical modulation of ca. 10 dB.

It is important to recognize that the requirements for a PCM material are not the same for different photonics applications and a single material cannot meet all specific needs and constraints. The most important characteristics typically expected for a PCM in different applications fields are coarsely outlined in Table 2, following an enlightening discussion published in ref. [Simpson 2022]. Besides the obvious requirement for large refractive index modulation (>100 %), other potentially important assets comprise (i) high refractive index (>2-3), (ii) fast switching speeds in both directions (< ns), (iii) low energy consumption, (iv) good reversibility over a large number of switching cycles (>10^9), (v) processability/integrability and, in some cases, (vi) non-volatility and associated long storage stability (>10 years).

While most of these requirements can be readily fulfilled by existing PCMs, an important bottleneck arises due to the high insertion losses. Indeed, one of the key points for integrated optics is the low absorption and/or scattering losses: while thin films can exhibit low absorption as the propagation length is low, equal to the layer thickness (< 1 µm), in integrated optics the propagation lengths are high (~ cm) and an excellent transmittance of the materials used becomes mandatory.

Table 2. Typical requirements for optical PCM materials in different applications

	Optical memories	Displays	SLMs	PICs
Large modulation depth	Medium	Medium	High	High
High refractive index	Low	Low	High	High
Fast switching speed	Medium	Low	High	High
Low switching energy	Medium	Medium	Medium	Medium
High switching endurance	Medium	Medium	High	High
Fabrication precision	Medium	Medium	High	High
Non-volatility	High	Low	Low	Low
Information storage stability	High	Low	Low	Low
Low insertion losses	Low	Medium	High	High

However, both VO_2 and $Ge_2Sb_2Te_5$ are low bandgap materials exhibiting high extinction coefficients ($k > 0.5–1$) in at least in one of the two states through the entire visible - near infrared (Vis-NIR) spectral ranges. In fact, not only these two materials, but most of the known PCM materials remain unsuited for operation in the sub-µm spectral domain. The development of new PCMs with high transparency in the Vis-NIR appears therefore vital for a broad range of applications. In this context, the performance of an active material used for phase modulation purposes in optical switches/modulators, can be quantified through the following figure-of-merit [Zhang 2018]:

$$FOM2 = \frac{\Delta n}{k_{min}} \tag{6}$$

where Δn is the refractive index change induced by the phase transition, while k_{min} denotes the extinction coefficient of the active material in its low-absorbing phase. The refractive index and extinction coefficient values of GST and VO_2 are shown in Figure 2.3a and 2.3c, respectively. A large value of k_{min} necessarily implies high insertion losses, which thus constrains the achievable optical modulation depth of the device. While this FOM2 is around 25 and 6 at 1550 nm for GST and VO_2, respectively, it falls to < 2 in the visible domain for both compounds, due to high values of k even in the

weakly absorbing phase (k_{min} > 0.5). By way of comparison, as mentioned in Chapter 1, SCO materials, due to their high transparency in both spin states, can exhibit a FOM2 greater than ca. 10-100 over the whole Vis-NIR wavelength domain, indicating that they could possibly surpass commonly used PCMs in terms of phase modulation capabilities in low-loss devices.

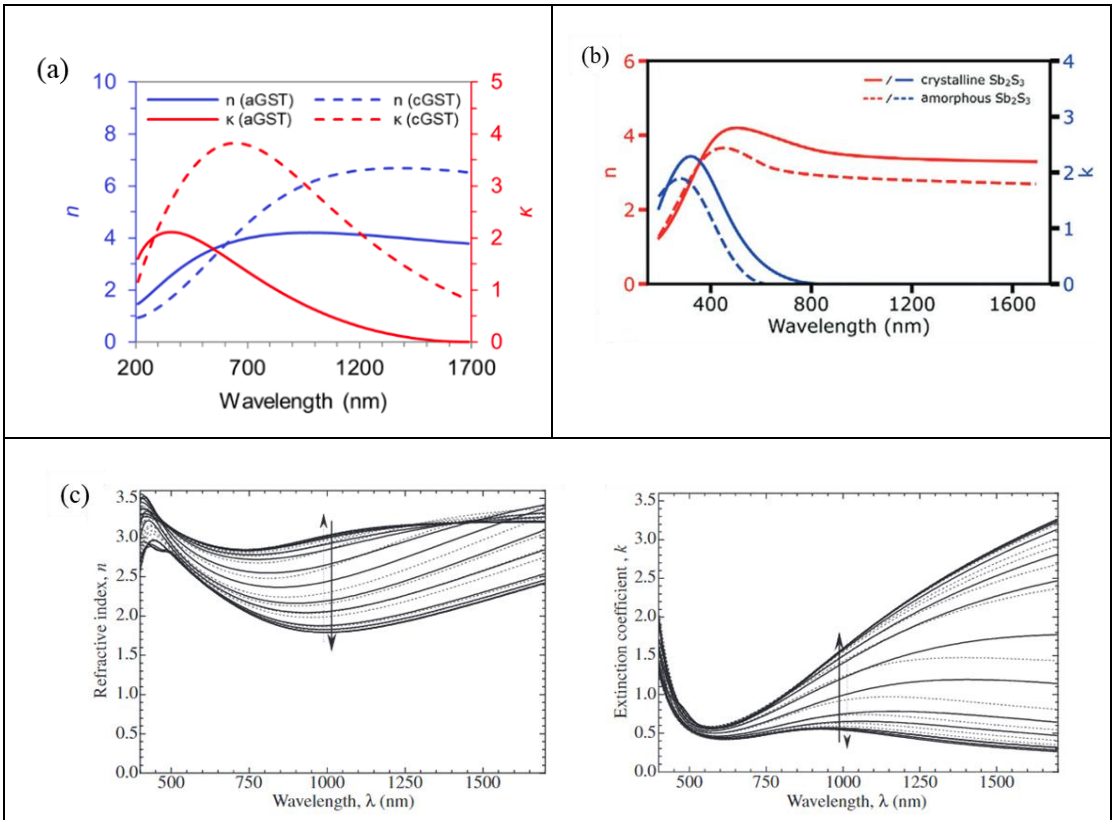

Figure 2.3. Optical properties of GST, VO_2 and Sb_2S_3 in the Vis-NIR spectral range. (a) and (b) are the complex refractive index of GST and Sb_2S_3, respectively, as a function of wavelength in both amorphous and crystalline phases. [Zheng 2018; Delaney 2020] (c) Refractive index and extinction coefficient of VO_2 as a function of wavelength, respectively, at various temperatures between 25 and 120 °C. Solid and broken curves indicate the data obtained during the rise and drop in temperature, respectively. [Kakiuchida 2007]

Some improvements have been demonstrated using sulfide and selenide based chalcogenides (instead of tellurides) [Dong 2019; Delaney 2020]. As an example, Dong et al. [Dong 2019] reported that the wide bandgap PCM, Sb_2S_3, can be reversibly switched between crystalline and amorphous states on a nanosecond time scale (see Figure 2.4a), and both states are stable at room temperature, enabling non-volatile

programming. More interestingly, compared with other PCMs, Sb_2S_3 exhibits not only a large change of refractive index (see Figure 2.3b), but also relatively low absorption in the NIR spectral range and, to some extent, in the VIS range as well (see Figure 2.3b). These appealing assets of Sb_2S_3 were then exploited in a Al/Si_3N_4/Sb_2S_3/Si_3N_4/Al stacked structure (displaying largely tunable resonances in the visible spectral range see Figure 2.4). Another interesting candidate in this context is the compound $Ge_2Sb_2Se_4Te_1$ (GSST), which has been recently proposed as a low-loss alternative to GST in the NIR, but it still suffers from poor FOM2 (< 3) in the visible domain [Zhang 2018; Zhang 2019].

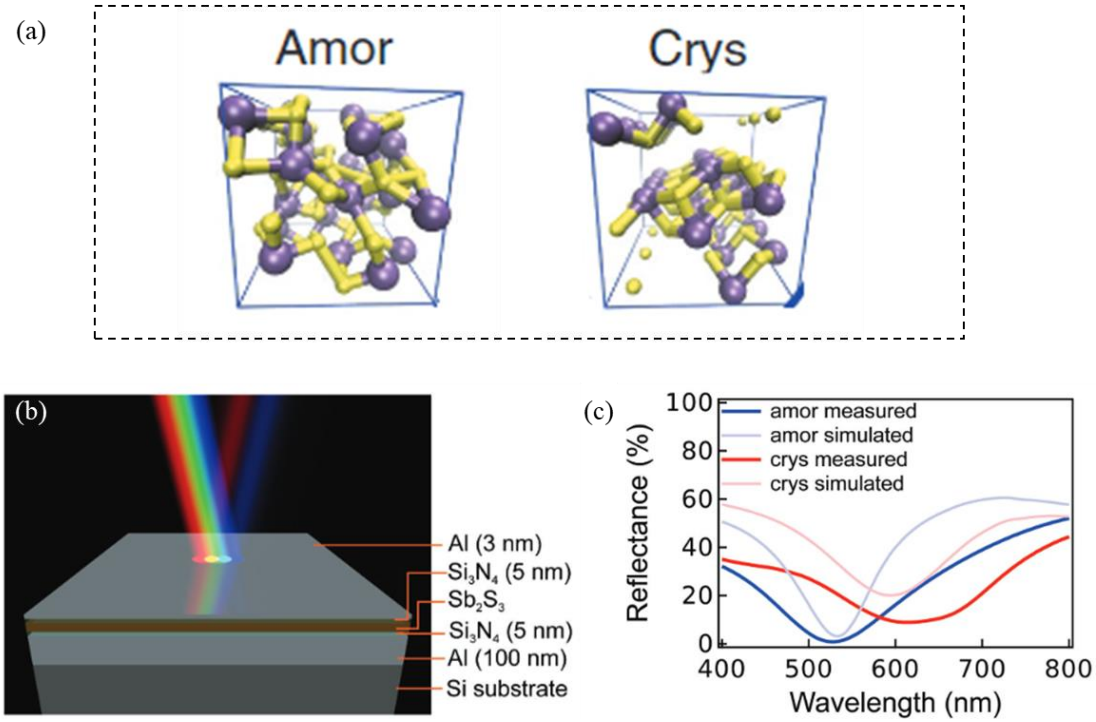

Figure 2.4. (a) Schematic structures amorphous (Amor) and crystalline (Crys) structures of Sb_2S_3. (c) Experimentally measured and simulated reflectance spectra of the structure shown in (b) with a 24 nm thick Sb_2S_3 layer in the amorphous and crystalline states [Dong 2019].

Although this material FOM2 does not reflect the universal applicability of PCMs in photonic devices, it however predicts that SCO materials, due to their extremely low optical absorption (in both spin states), can be superior to well-established PCMs for specific applications (e.g. phase modulation), requiring broadband transparency in the

Vis-NIR spectral domain. In addition, it is worth mentioning that SCO compounds may also offer other significant advantages over conventional PCMs such as both volatile and non-volatile operation (i.e. spin transition with or without hysteresis loop), low power consumption and the possibility of fast all-optical modulation. It is fair to say, however, that the price to pay is a lower refractive index change exhibited by SCO compounds in comparison to other PCMs.

2.2 Fabrication and characterization of [Fe(HB(1,2,4-triazol-1-yl)$_3$)$_2$] thin films

The molecular structure of the SCO complex [Fe(HB(1,2,4-triazol-1-yl)$_3$)$_2$] **1**, considered in this study, is shown in Figure 2.5a. As displayed in Figure 2.5b, the bulk powder of **1** exhibits abrupt spin crossover between the LS and HS states above room temperature ($T_{1/2} \approx 333$ K) with a small hysteresis loop ($\Delta T \approx 1$ K) [Rat 2017].

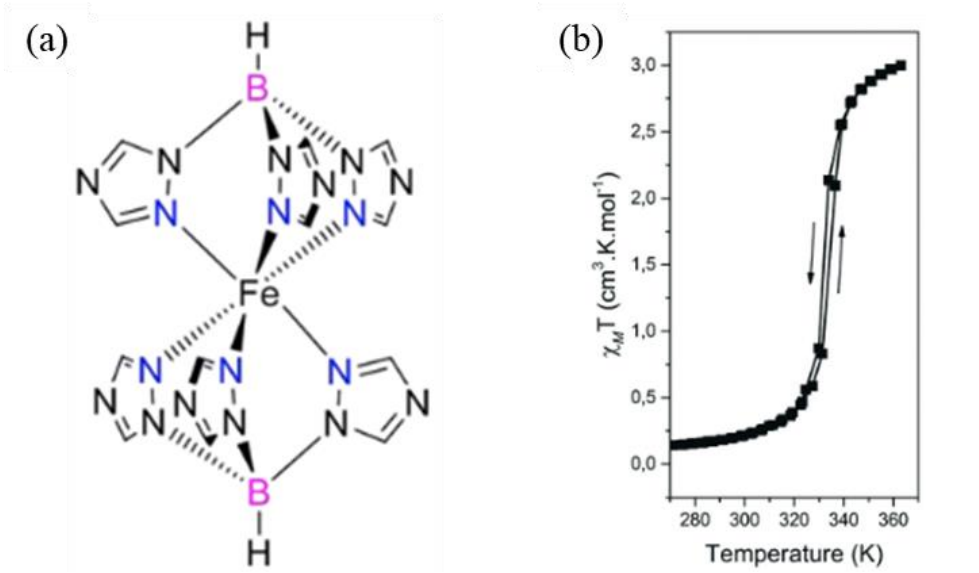

Figure 2.5. (a) Molecular structure of SCO complex **1**. (b) Variable temperature magnetic measurements for the bulk powder of **1** [Rat 2017].

Importantly, complex **1** is sublimable, which means that thin films can be deposited by thermal evaporation in a vacuum thermal deposition system. In our case, this was achieved, using a PREVAC system (see figure 2.6), at a base pressure of 2×10^{-7} mbar.

The system is equipped with a rotating substrate holder to improve film thickness uniformity, typically rotating at a rate of 0.4 rad/s. The films were deposited on silicon and fused silica substrates. These substrates were first washed successively with acetone and ethanol (>99.8 % purity) for 5 min under sonication to remove the contaminants, and finally dried by an argon or nitrogen gas flow. The bulk powder of **1** was then heated to 250 °C in a quartz crucible and evaporated onto the substrates at a rate of 0.05 Å/s. Film thicknesses were monitored in situ using a quartz crystal microbalance, and ex situ by spectral reflectance measurements (Filmetrics, F20). It is worth noting that the as-deposited films of **1** are amorphous, leading to a lack of stability. To overcome this problem, the as-deposited films can be recrystallized by means of solvent-vapor annealing. Specifically, for films of **1**, it is achieved by placing the as-deposited films in a sealed box with a humidity of *ca.*75–80% at room temperature, resulting in their efficient and fast crystallization [Shalabaeva 2017a]. It is worth to note that solvent annealing does not significantly change the film thickness.

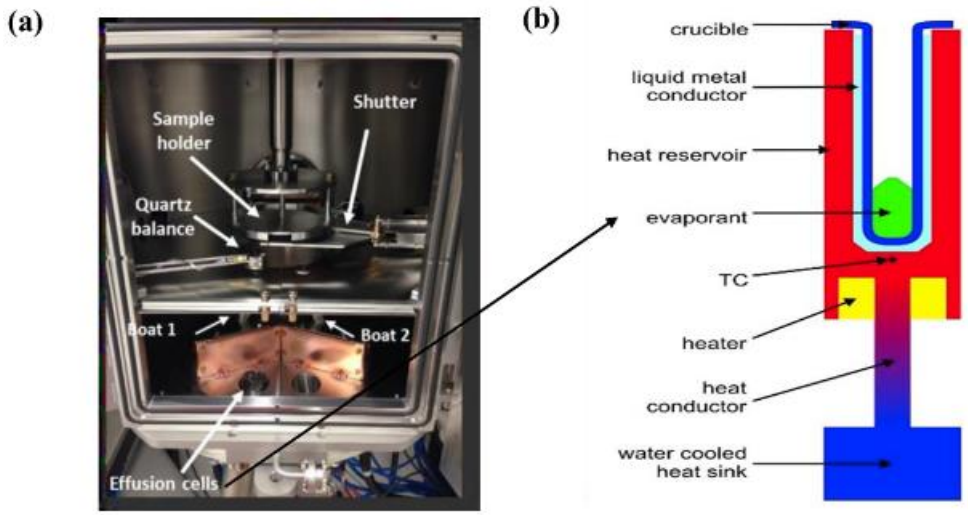

Figure 2.6. (a) Photograph of the vacuum chamber of the PREVAC thermal deposition system. (b) Scheme of the organic material effusion cell used in this system.

The structural characterization of the recrystallized films was achieved by using grazing-incidence X-ray diffraction (GIXRD), which was conducted in ambient conditions by means of a PANalytical X'Pert PRO MPD system using Cu-Ka radiation with a parallel-beam configuration. As shown in Figure 2.7, the typical diffraction

pattern of the as-deposited films shows no obvious diffraction peak indicating the film is amorphous.

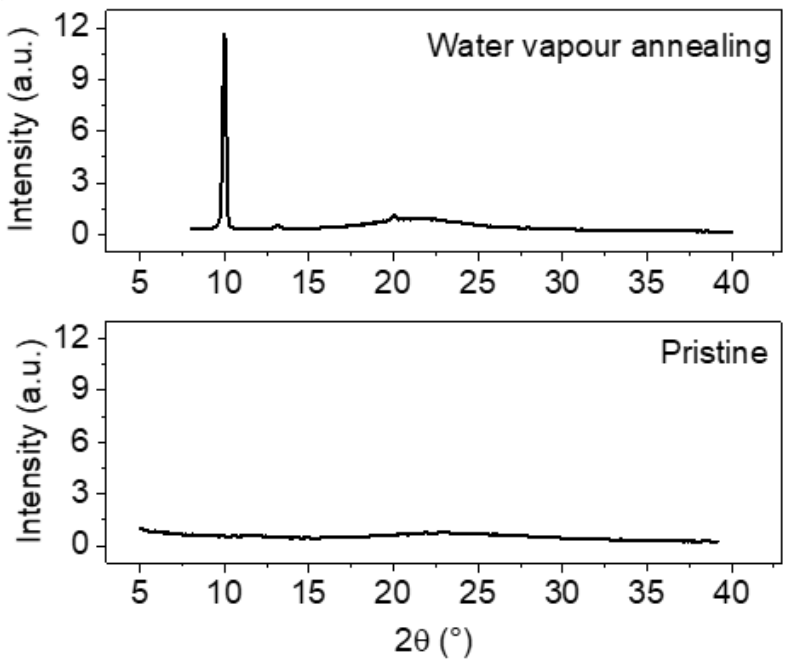

Figure 2.7. GIXRD spectrum of the pristine (as-deposited) and that of the recrystallized film of complex **1** [Shalabaeva 2017a].

On the other hand, for the recrystallized film, one observes a strong peak at 2θ = 10.02° indicating crystallinity and a preferential crystallographic orientation. Indeed, from previous investigations [Shalabaeva 2017a] we know that this peak corresponds to the 002 reflection, which indicates the c-axis of the orthorhombic unit cell of the crystallites is perpendicular to the plane of the substrate. In addition, a weak and broad peak appears at 2θ = 20–25°, which is typical for amorphous fused-silica substrates. The morphology of the films was characterized by atomic force microscopy (SmartSPM, Horiba) in tapping mode in ambient conditions. The roughness of different areas of the film is slightly different, which is probably due to impurities, imperfection of the substrate and other reasons that lead to a certain degree of heterogeneous nucleation and growth. Typically, the roughness (Ra) is lower than 2.5 nm for a 150-nm-thick film and no pinholes are observed on relatively large areas (several mm^2) (see Figure 2.8).

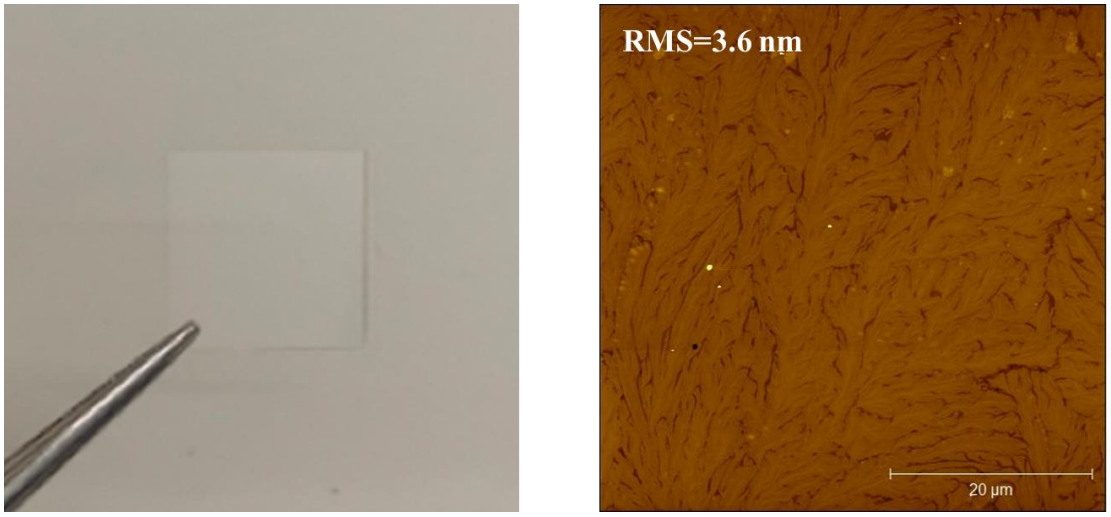

Figure 2.8. Photograph and AFM topography image of the recrystallized film of complex **1**.

The spin-transition properties of the thin films were explored by using variable-temperature UV-Vis spectrophotometry, which requires the combined use of a Cary 50 (Agilent Technologies) spectrophotometer and a Linkam FTIR-600 liquid nitrogen cryostat (equipped with UV-transparent fused-silica windows). In agreement with previous results [Shalabeava 2017a], the absorbance spectra of the films of **1**, deposited on fused-silica substrates, exhibit intense, SCO-dependent absorption bands in the UV spectral range (see Figure 2.9a). Specifically, at room temperature (in the LS state), complex **1** exhibits three bands around 272, 305 and 317 nm. Considering the high absorption coefficients associated with these peaks (*ca.* 10^4 cm^{-1}), they presumably correspond to charge-transfer (metal-to-ligand and/or ligand-to-metal) transitions. As shown in Figure 2.9a, these absorption bands are completely bleached upon heating the film above the spin-transition temperature, the HS being fully transparent within the 250-800 nm spectral range. By following the temperature evolution of the optical absorbance at the peak wavelength (λ = 317 nm) (Figure 2.9b), we observe that films of **1** exhibit an abrupt spin transition centered around 64 °C, spanning over a temperature range of *ca.* 12 °C.

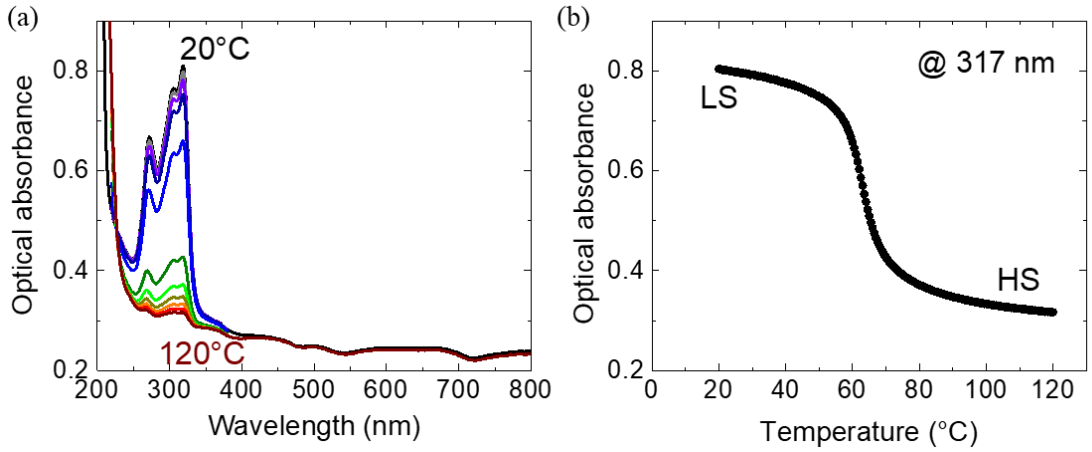

Figure 2.9. (a) Optical absorbance spectra of a 138-nm-thick film of the complex **1**, acquired at selected temperatures between 20 and 120 °C. The films were deposited on fused-silica substrates. (b) Thermal spin-transition curves of the film extracted from the temperature variation of the optical absorbance at the peak wavelength (λ = 317 nm).

Importantly, the vacuum-deposited films of **1** are known to display strong resilience and exceptionally high switching endurance upon repeated cycling. Indeed, in a recent study [Ridier 2020], it was shown that the spin-transition properties of thin films of **1**, deposited on top of Joule-heated microwires, remain virtually unchanged after more than 10 million thermal switching events in ambient air (see Figure 2.10). It may be worth to note also the good storage stability of these films.

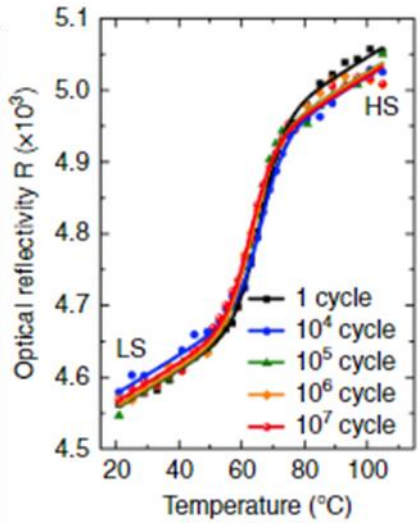

Figure 2.10. Thermal evolution of the optical reflectivity (λ = 452 nm) of a 200-nm-thick film of **1** on top of a gold microwire after 1, 10^4, 10^5, 10^6, and 10^7 thermal cycles in ambient air induced by Joule heating [Ridier 2020].

To better analyze the optical properties of compound **1**, Figure 2.11 displays the evolution of the real part (n) and the imaginary part (k) of the complex refractive index of films of **1**, as a function of the wavelength and the temperature. The refractive index, n, was obtained from previously published ellipsometric data [Zhang 2020], while the extinction coefficient, k, is deduced from our spectrophotometric measurements.

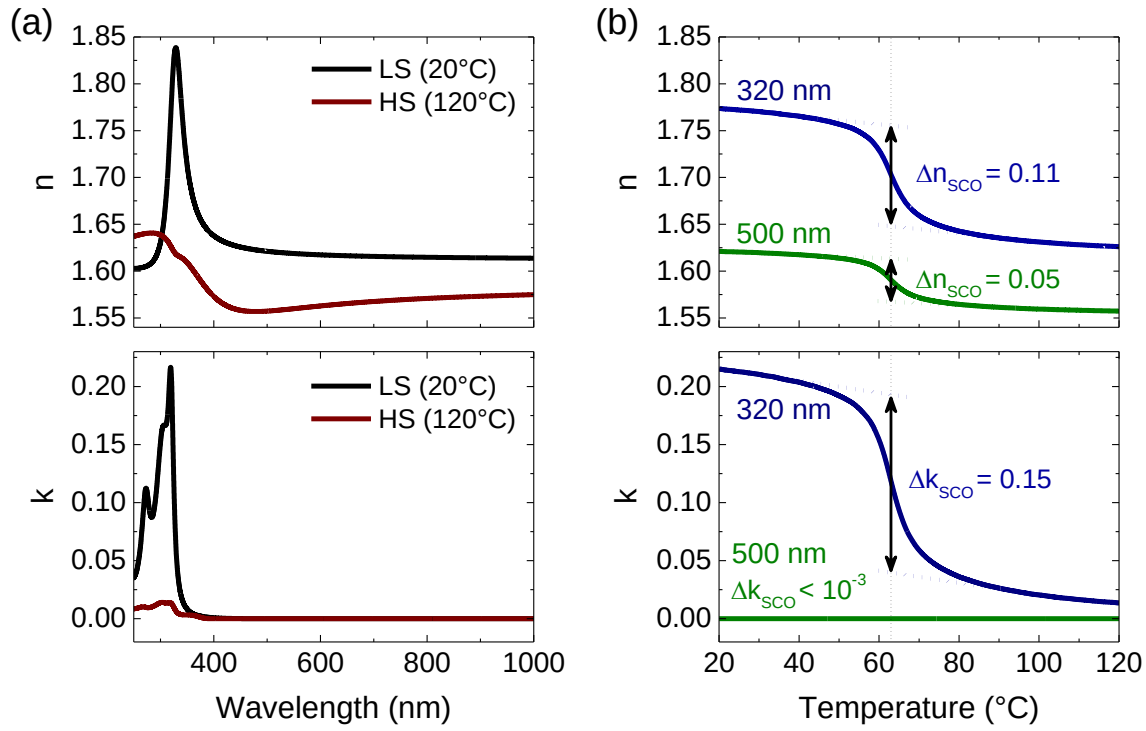

Figure 2.11. Optical indices of compound **1**. (a) Real (n) and imaginary (k) part of the complex refractive index of **1** as a function of the wavelength in the LS (20 °C) and HS (120 °C) states. (b) Evolution of n (top panel) and k (bottom panel) as a function of the temperature at two given wavelengths (320 and 500 nm

While the refractive index change between the LS and HS state is relatively large in the UV range (associated with a notable change of the absorption properties of the material), we observe that Δn reaches about 0.05 at 500 nm due to the sole SCO phenomenon. On the other hand, these measurements reveal that, apart from the relatively intense charge-transfer absorption bands observed in the UV spectral domain ($k = 0.22$ in the LS state at 320 nm), absorption and scattering losses remain very low ($k \leq 10^{-3}$) in both spin

states at any wavelength above 350 nm. In detail, complex **1** only exhibits a weak Laporte-forbidden ligand-field absorption band centered around 535 nm in the LS state [Ridier 2019] associated with an absorption coefficient of $\alpha \approx 200$ cm^{-1} (which corresponds to a maximum extinction coefficient of $k \approx 9 \times 10^{-4}$). Everywhere else, the extinction coefficient virtually becomes negligible ($k < 10^{-4}$) in both spin states. Therefore, in the whole visible spectral range, films of **1** show a typical change of the refractive index of $\Delta n_{SCO} = 0.05$ upon the spin transition, while the extinction coefficient is extremely low and remains virtually unchanged in both phases (k and $\Delta k_{SCO} \leq 10^{-3}$). The relevant figure-of-merit (FOM2, equation 6) is thus ca. 50 near 535 nm and reaches even higher values far from the ligand-field absorption band.

The transition in **1** is volatile, opening prospects for fast optical modulation. Indeed, as discussed in Chapter 1, ultrafast optical spectroscopy investigations revealed the possibility of very reproducible, sub-ps, photo-switching with pulse energies of the order of 20 mJ cm^{-2}, followed by a photothermal switching and back relaxation on the ns and µs time scales (Fig. 1.21), respectively, enabling a possible light-induced modulation of the spin state in the 1–10 MHz frequency range [Ridier 2019]. Recently, these appealing assets of films of **1** have been then exploited in our team by inserting them into multilayer Ag/**1**/Ag Fabry-Pérot cavities [Zhang 2020]. These cavities were designed with resonances in the green spectral region (at normal incidence) and quality factors Q of *ca.* 30. Switching the spin state of the SCO film from the LS to the HS state gave rise to a reversible blue-shift of the cavity resonance (up to 8 nm) in response to the refractive index modulation, providing proof for the spectral tunability conferred to the device by the SCO phenomenon.

Based on these previous achievements, in a first time we have fabricated a new series of Ag/**1**/Ag Fabry-Perot cavities, incorporating a thin film of compound **1**, with the aim of conducting a more in-depth study of the optical properties of this resonator and of its thermal tunability. The next section presents the optical characterization of this device in transmission mode, as a function of wavelength, incident angle, temperature and light polarization, using a new custom-built optical bench specially set up for this purpose.

2.3 Ag/SCO/Ag Fabry-Perot cavities

2.3.1 General principles of Fabry-Perot cavities

A Fabry-Pérot cavity can be composed of two parallel semi-transparent mirrors and a dielectric layer sandwiched between them, also known as plane-parallel cavity, and its structure is shown in Figure 2.12a [Bitarafan 2017]. The incident light is reflected back and forth between the two mirrors, and each transmitted wavefront obviously undergoes an even number of reflections. Only electromagnetic waves with constructive interference will form standing waves, i.e. resonance modes, inside the cavity. The formula related to the resonance wavelength is given by:

$$m\lambda = 2nL\cos\theta \tag{7}$$

where n is the refractive index of the dielectric layer, L is the thickness of the dielectric layer, θ is the incident angle, λ is the central wavelength of the transmitted light and m = 1,2,3.... is an integer representing the mode order. According to this formula, the resonance wavelength can be adjusted by the following ways: firstly, changing the refractive index of the dielectric layer; secondly, changing the thickness of the dielectric layer; finally, changing the angle of the incident light.

In a typical transmittance spectrum as shown in figure 2.12b, the peaks correspond to resonance wavelengths, and the frequency separation between two adjacent resonance peaks is the free spectral range (FSR), which is calculated as:

$$FSR = \frac{c}{2nL\cos\theta} \tag{8}$$

where c is the speed of light in vacuum. An ideal cavity confines light infinitely, therefore its resonant wavelengths should have exact values. Deviations from ideal conditions are described by the quality factor (Q factor) defined as:

$$Q = \frac{E_{cav}}{\Gamma_{cav}} \tag{9}$$

where E_{cav} and Γ_{cav} are the energy and the resonance width (i.e. the FWHM) of the cavity, respectively.

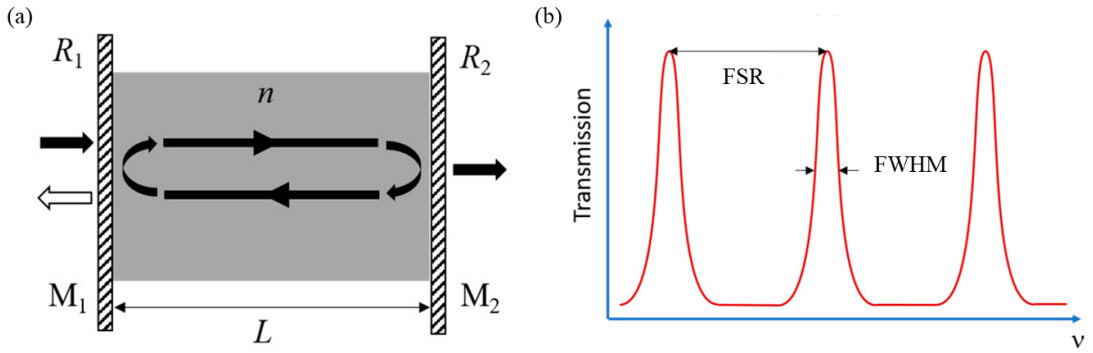

Figure 2.12. (a) Scheme of a Fabry-Perot resonator consisting of parallel mirrors M_1 and M_2 with reflectances of R_1 and R_2, respectively, separated by a cavity medium of refractive index n and thickness L. Light introduced from one side undergoes multiple reflections, leading to partial transmission from the other side. (b) Typical transmission spectrum of a planar Fabry-Pérot cavity depicting frequency spacing (i.e., the FSR) of adjacent longitudinal modes and the full-width at half-maximum (FWHM) of an individual modal peak [Bitarafan 2017].

2.3.2. Fabrication and characterization of Ag/SCO/Ag cavities

In this chapter, the SCO complexes **1** is embedded as a dielectric layer in the Fabry-Pérot cavity with Ag as mirrors (see figure 2.13), and the change of the refractive index of the complex **1** is used to render the resonance(s) of this cavity wavelength-tunable. The Ag layers were chosen as mirrors because silver is an excellent and easy-to-fabricate mirror in the Vis-NIR region. The most commonly used method to explore the optical properties of multilayer stacks is the transfer matrix method. In brief, if the thickness of each layer of the multilayer stack and the corresponding refractive indices are known, the transmittance and reflectance at each specific incident angle and wavelength can be calculated by repeatedly using the Fresnel equations [Windt 1998]. The numerical algorithm of this method is implemented in the software of our Filmetrics instrument, but more in-depth simulations were also conducted in collaboration with Karl Ridier (LCC-CNRS) and Stéphane Calvez (LAAS-CNRS, Toulouse). As it can be expected, by increasing the thickness of the Ag layer, the

resonance width decreases, leading to an increase in the Q factor of the cavity, but at the same time, the intensity of the resonance peak decreases, which is not ideal for optical modulation. To reach a compromise between these two tendencies, a 40-nm-thick Ag film was prepared. Furthermore, the resonance wavelength depends on the thickness of the SCO layer, therefore, to achieve a wavelength-tunable device working in the green spectral region (at normal incidence), the calculated SCO film thicknesses was 142 nm.

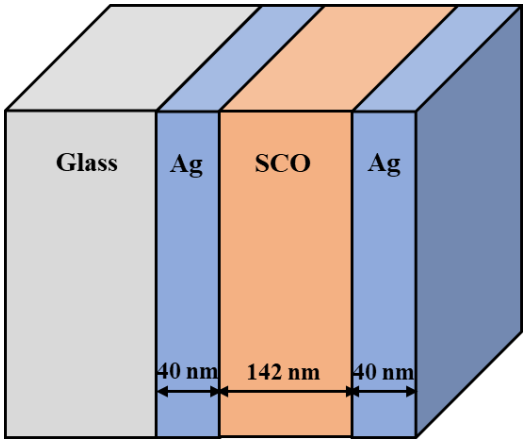

Figure 2.13. Scheme of the Ag (40 nm)/ **1** (142 nm)/Ag (40 nm) Fabry-Pérot cavity.

Both **1** and the Ag layers were deposited by vacuum thermal evaporation (typically) at 5×10^{-7} Torr base pressure. To reach a high degree of crystallinity the as-deposited SCO film was annealed as described above. Film thicknesses were monitored in situ using a quartz crystal microbalance and ex situ by AFM for the Ag layers and by spectral reflectance measurements (Filmetrics, F20) for the SCO layer. The Ag (40 nm)/**1** (142 nm)/Ag (40 nm) stacks were deposited on thin, rectangular ($10\times10\times0.5$ mm^3), double side polished, UV grade, fused silica substrates (MicroChemicals, ref. JGS1). Then, this cavity was characterized for its optical properties using a custom-built optical bench (see figure 2.14) allowing the acquisition of both the transmittance and the reflectance of the sample as a function of the wavelength (200–1000 nm), angle (0–80°) and polarization of the incident light beam as well as the temperature (20–120 °C).

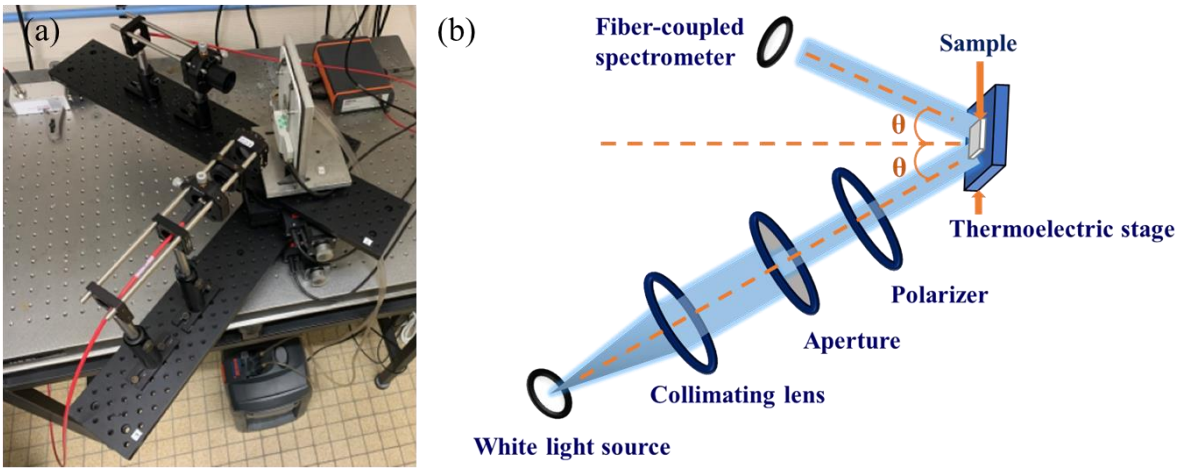

Figure 2.14. (a) Photograph and (b) scheme of our home-made optical bench used to characterize both in transmittance and reflectance the fabricated photonic cavities as a function of the temperature, light polarization, wavelength and angle of incidence.

A pulsed xenon lamp (Avalight-XE-HP, Avantes, 6 W, 150 Hz) is used as a white light source. The light beam is directed from the source to the sample by using fiber optics. Before reaching the sample, the light propagates through a collimating lens, a polarizer and an iris diaphragm, allowing the control of the beam intensity and size. The sample is attached onto a thermoelectrical heating-cooling stage (PE120, Linkam Scientific), equipped with a center hole (in order to keep air as the last dielectric layer), allowing for temperature scans at controlled rates (±2 °C/min). The transmitted light is relayed to a spectrometer (Avaspec ULS2048CL-EVO-UA-50, Avantes, 2.5 nm spectral resolution) using an optical fiber (of core diameter 600 µm and numerical aperture NA = 0.22). The angles of incidence and collection are adjusted using two independent, high precision rotation stages (position accuracy ~1 mrad) driven by a microprocessor controlled stepping motor (HDR50 and BSC202, Thorlabs).

2.3.3 Optical properties and thermal tunability of Ag/SCO/Ag cavities

The evolution of the s- and p-polarized transmittance of the Ag (40 nm)/**1** (142 nm)/Ag (40 nm) Fabry-Perot cavity, measured at different incident angles at room temperature, as a function of the wavelength is shown in figures 2.15a and 2.15c, respectively, and the corresponding 3D dispersion curves are shown in figures 2.15b and 2.15d,

respectively. As the incident angle increases, the resonance wavelength is blue-shifted, which is completely consistent with equation 7. In addition, as the incident angle increases, the transmittance of the s-polarized mode decreases, while that of the p-polarized mode increases. Finally, for a given angle of incidence (especially at large angles), it is clearly demonstrated that the shift of the resonance wavelength for the s-polarized mode is larger than for the p-polarized mode.

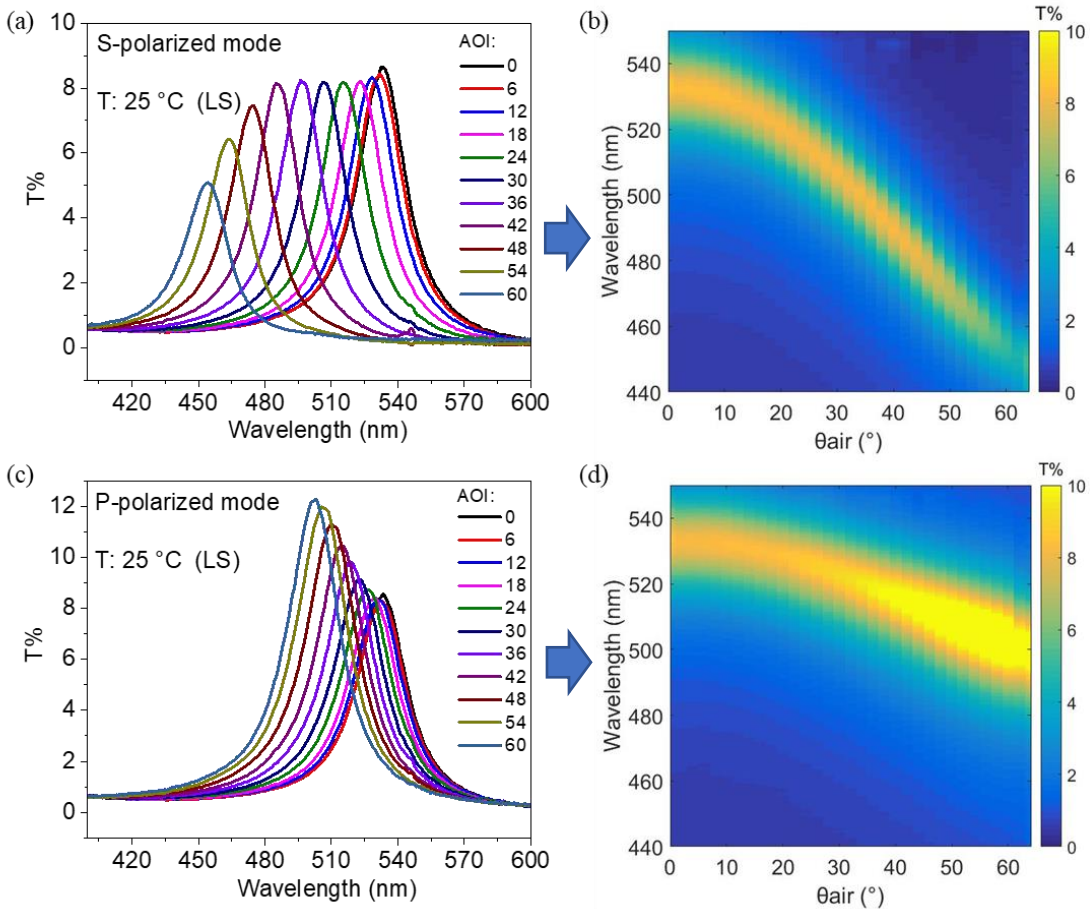

Figure 2.15. (a) S- polarized and (c) p-polarized transmittance spectra recorded for the Ag (40 nm)/**1** (142 nm)/Ag (40 nm) Fabry–Pérot cavity at room temperature (25 °C) for different angles of incidence and the corresponding 3D dispersion curves (b) and (d), respectively.

To get a first insight into the spin state dependence of the resonance wavelength of the cavity, we have also assessed angle and polarization dependent spectra at 120 °C. Figure 2.16 compares the dependence of the resonance wavelength on the angle of incidence (AOI) in the HS (120 °C) and LS (25 °C) states for both s- and p- polarized modes. For

both polarized modes, one can observe a difference in resonance wavelength between the LS and HS states, which is however more important for the s-polarization and increases as the incident angle increases. To better follow the effect of the thermally induced spin transition, figure 2.17a displays the temperature evolution of the s-polarized mode of the cavity at a fixed angle of incidence $\theta = 60°$, both in heating and cooling modes. The LS to HS spin transition in the cavity gives rise to an abrupt drop of the resonance wavelength near 65 °C, which is fully reversible upon cooling. Figure 2.17b displays the transmittance spectrum of this cavity for the s-polarized mode at a fixed angle of incidence ($\theta = 60°$) at 25 °C (LS) and 119 °C (HS). From this figure one can depict a ca. 8 nm shift of the resonance wavelength between the LS and HS states, which gives rise to a transmittance modulation of ca. 3 % (at maximum). Clearly, this small modulation results from the relatively high FWHM of the resonance peak (ca. 23 nm) and, more importantly, from the low peak transmittance (ca. 6 %). One shall note that the resonance intensity is the same in the two spin states, which signifies clearly that the modulation is exclusively linked to the change of the real part of the refractive index upon the SCO.

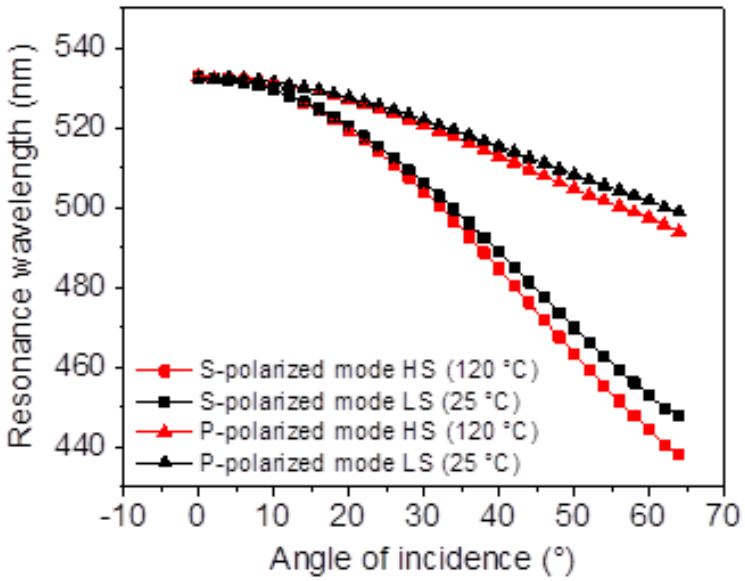

Figure 2.16. Dispersion curves of the Ag (40 nm)/**1** (142 nm)/Ag (40 nm) Fabry–Pérot cavity in the LS and HS states for s- and p- polarized modes.

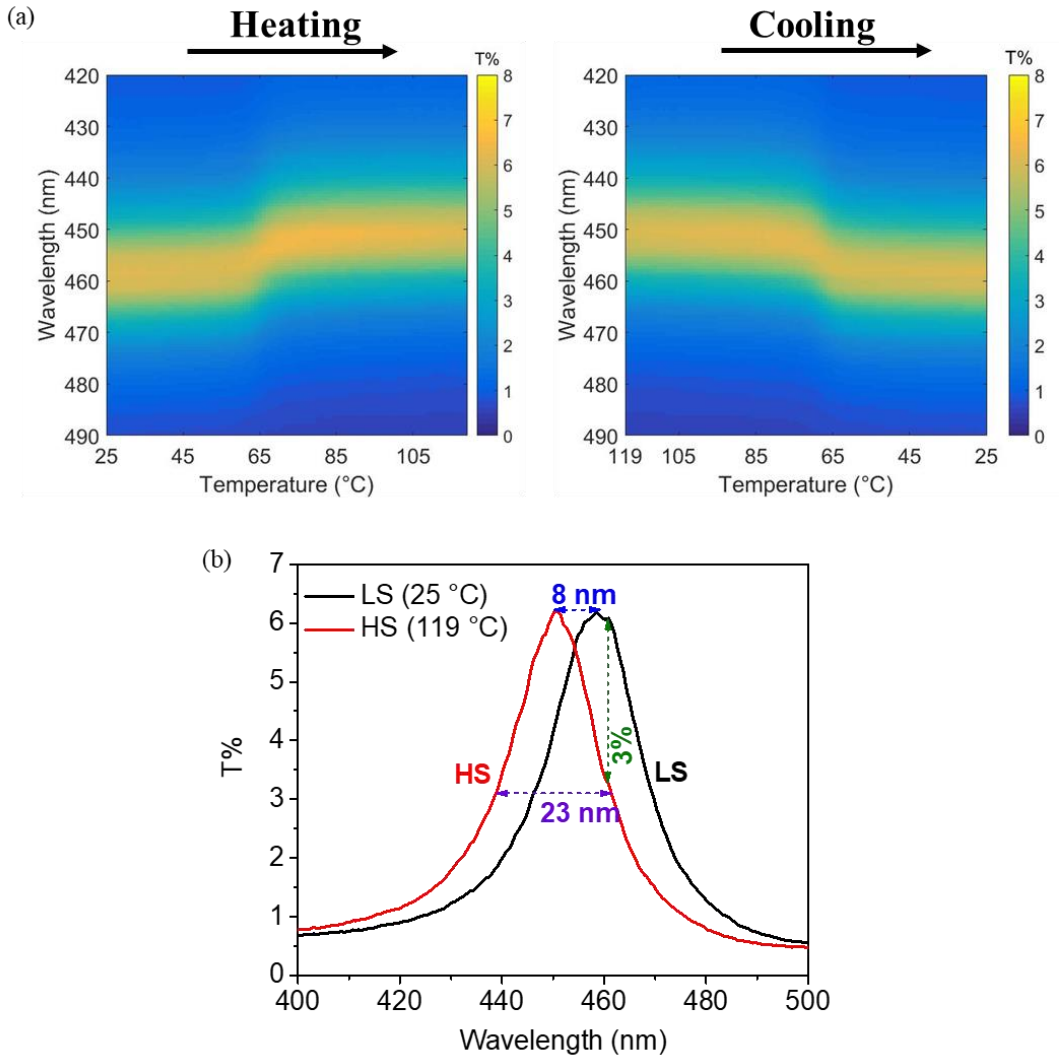

Figure 2.17. (a) Evolution of the s-polarized resonant mode of the Ag (40 nm)/**1** (142 nm)/Ag (40 nm) cavity, measured at a fixed angle of incidence θ= 60°, as a function of the temperature, upon heating and cooling between 25 and 119 °C. (b) S- polarized transmittance spectra recorded for the same cavity at a fixed angle of incidence θ = 60° in the LS and HS states.

As shown in figure 2.18, the variation of the resonance wavelength as a function of the temperature is the result of two phenomena: ordinary thermal expansion and SCO, which are superimposed, resulting in a total shift of the resonance wavelength of 8 nm. Far from the spin transition, the thermal expansion of the SCO film leads to a slight decrease in the refractive index (n) and an increase of the cavity length (L), which have opposed effects on the resonance wavelength (see equation 7). The experimental result in figure 2.18 shows a slight, linear blue-shift of the resonance for increasing

temperatures (both in the LS and HS states), highlighting that the dominant effect is the variation of the refractive index. More importantly, the drop of the resonance wavelength becomes abrupt near 65 °C, which is obviously the signature of the spin transition. The associated resonance shift (ca. 6 nm) is again a result of two opposed effects: the decrease of the refractive index (see the ellipsometry data in Fig. 2.11) and the increase of the film thickness (see the XRD data in Fig. 1.17) in the HS state. Again, the former effect prevails on the latter.

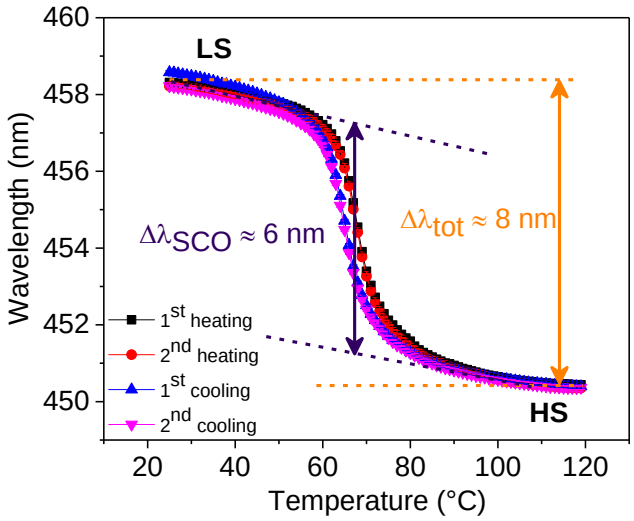

Figure 2.18. Resonance wavelength as a function of temperature at a fixed angle of incidence ($\theta = 60°$) for the s-polarized mode over two complete thermal cycles between 20 and 120 °C acquired at a rate of 2 °C/min for the Ag (40 nm)/**1** (142 nm)/Ag (40 nm) Fabry-Pérot cavity.

2.3.4 Figures-of-merit

From an applicative point of view, in addition to the study of the shift of the resonance wavelength upon the SCO, other important parameters must be considered as well. The most widely used figure of merit for resonance tuning is given by the expression:

$$\text{FOM3} = \Delta\lambda/\text{FWHM} \qquad (10)$$

This FOM3 highlights that it is not only the magnitude of the resonance shift that matters, but also the resonance width, i.e. the quality factor of the cavity. Figure 2.19a (top panel) shows the temperature dependence of FOM3 (the initial position of the

resonance at 25 °C being considered as the reference) at an angle of incidence of 60° for the s-polarized mode of our Fabry-Perot cavity. FOM3 reaches a maximum value of 0.35, which means that the resonance shift caused by the SCO is smaller than the resonance linewidth, which in obviously an undesired feature. To further characterize the thermal sensitivity, the thermal evolution of the temperature derivative of $\Delta\lambda/FWHM$ (always given at an angle of $\theta = 60°$ for the s-polarized mode) is plotted in the bottom panel of figure 2.19a. The derivative $d(\Delta\lambda/FWHM)/dT$ reaches a maximum value of -0.2 $°C^{-1}$ near the spin transition temperature, indicating a substantial increase in sensitivity due to the SCO phenomenon.

Another important parameter is the maximum transmittance change ($\Delta Tr = Tr_{(LS)}-Tr_{(HS)}$), i.e. the highest optical modulation the device can reach. (N.B. At this point, we shall note that in the literature the authors usually do not give the absolute value of the transmittance (or reflectance) change. Instead, they describe the optical modulation by the relative change $Tr_{(HS)}/Tr_{(LS)}$, often given in decibels, i.e. on a logarithmic scale. In the context of the present work, we use ΔTr, because this quantity is more relevant whenever transparency is an important criterion.) Figure 2.19b displays the optical modulation of the Ag (40 nm)/**1** (142 nm)/Ag (40 nm) Fabry–Pérot cavity as a function of the temperature at an angle of incidence of 60° and a wavelength of $\lambda = 461$ nm for the s-polarized mode. As mentioned before, ΔTr reaches a maximum value of only -3 % in this device. The associated derivative $d(\Delta Tr)/dT$, shown in figure 2.19b (bottom panel) indicates that the spin-state switching involves a maximum thermal sensitivity of -0.2 % $°C^{-1}$.

To conclude about the work on the Ag/**1**/Ag resonators, we have demonstrated that taking advantage of SCO complexes with low extinction coefficients and large refractive index changes between the two spin states, active optical devices can be fabricated and used in the visible spectral range. Notably, the multilayer stack [Ag (40 nm)/**1** (142 nm)/Ag (40 nm)] exhibits a resonance wavelength shift up to 8 nm. However, the achievable transmittance contrast remains relatively low (ca. 3 %), which is not favorable for practical applications. Some further improvements could be

certainly obtained by increasing the quality of the films and thus concomitantly reducing the FWHM and increasing the transmittance of the resonance peak. Nevertheless, for the rest of our work we decided to turn our attention to a different resonator design.

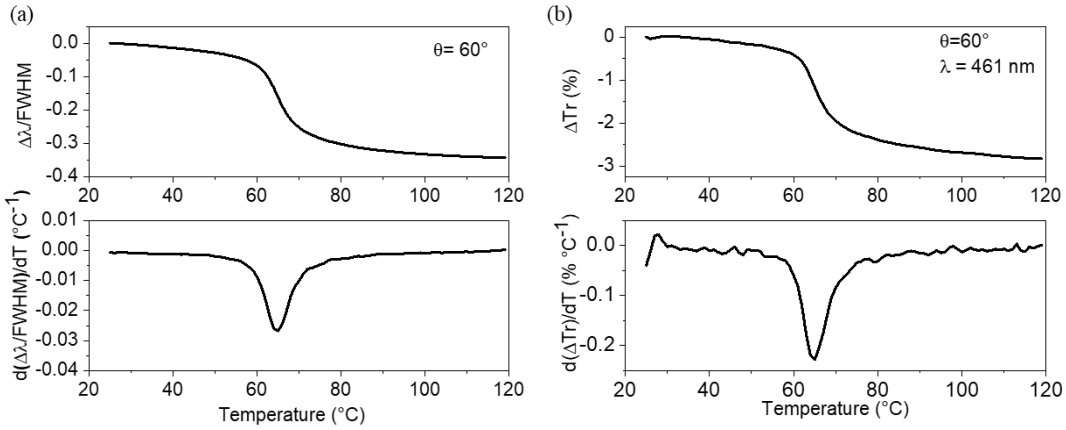

Figure 2.19. Main figures-of-merit (FOM) of the Ag (40 nm)/**1** (142 nm)/Ag (40 nm) Fabry–Pérot cavity. (a) Thermal evolution of the ratio $\Delta\lambda/FWHM$ (top panel) and of its derivative with respect to the temperature (bottom panel), for the s-polarized mode of the Ag (40 nm)/**1** (142 nm)/Ag (40 nm) Fabry–Pérot cavity at an angle of incidence of 60°. (b) Thermal evolution of the transmittance change ΔTr (top panel) and of its derivative with respect to the temperature (bottom panel), at an incident angle of 60° and a wavelength of λ = 461 nm for the s-polarized mode.

2.4 Ag/SCO bilayer resonators

In order to overcome the issue of low optical modulation, in the next step, we have designed and fabricated a new type of optical resonator, which consists of a simple Ag/**1** bilayer structure, excited using a coupling prism, and operating in total internal reflection (TIR) geometry. We demonstrate that this bilayer structure is not only easy to fabricate, but also provides a higher sensitivity to refractive index change, showing a larger spectral shift of the resonant mode ($\Delta\lambda_{SCO} \approx 30$ nm) upon SCO and, ultimately, a higher optical reflectance contrast (ΔR = 70 %) compared to the Ag/**1**/Ag device. Interestingly, we show that this Ag/**1** bilayer resonator can also be used to realize optical limiting applications, because the large thermal tunability of the device gives rise to a photothermal nonlinearity.

2.4.1 Device fabrication and characterization

The base of a right-angle, glass (N-BK7) prism was successively coated by a 35-nm-thick layer of Ag and a 162-nm-thick film of **1** by vacuum thermal evaporation at *ca.* 5 × 10^{-7} Torr base pressure. To reach a high degree of crystallinity the as-deposited film of **1** was annealing as described before. The film thicknesses were monitored in-situ using a quartz microbalance and verified ex-situ using AFM for the Ag film and optical reflectance data in combination with transfer-matrix calculations for the film of **1**. The optical properties of the fabricated bilayer resonator were investigated by spectroscopic reflectometry measurements using the same optical bench as shown in Figure 2.14, allowing the acquisition of reflectance data as a function of wavelength (200–1000 nm), incident angle (16–80°), light polarization (s and p) and temperature (20–120 °C).

Resonances in our Ag/SCO bilayers can be excited only under wavevector matching conditions, which we achieved using the Kretschmann method (see Figure 2.20), employing a glass prism as a coupling medium [Kretschmann 1968]. One shall note that, contrary to conventional SPR spectroscopy, the presence of the dielectric SCO layer (with a relatively large thickness, 162 nm) affords for the resonant excitation of electromagnetic modes with both p- and s- polarized light when passing through the glass prism under TIR conditions. Indeed, for a bare metallic film only a p-polarized resonance can be excited, while the presence of an ultrathin dielectric coating merely leads to a shift of this resonance (either in wavelength or in angle, depending on the method of interrogation), which is the basis of the well-known SPR sensor applications. However, beyond a critical thickness of the dielectric layer, one can also observe a s-polarized resonance, and upon a further increase in thickness, higher order p- and s-polarized resonances appear as well. In practice, coupling the incident light to the electromagnetic modes of the resonator thus gives rise to several sharp dips of the TIR intensity for different combinations of wavelength and angle of incidence, which fulfill the resonance conditions (i.e., simultaneous energy and wave vector matching).

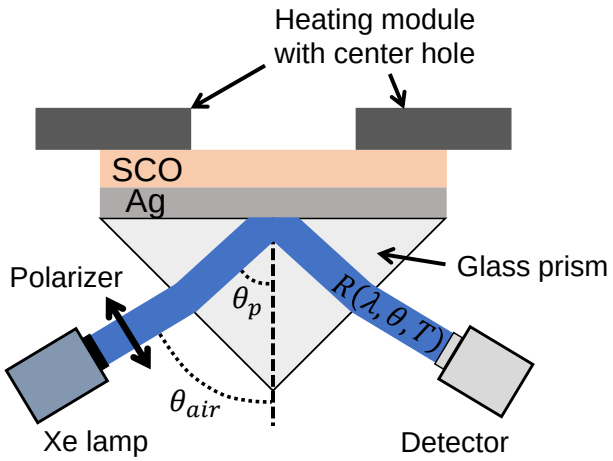

Figure 2.20. Scheme of the attenuated total internal reflection setup used to couple light to the resonator formed by the Ag (35 nm)/**1** (162 nm) bilayer deposited on a glass prism.

2.4.2 Optical properties and thermal tunability

A typical example of the resonance spectra obtained with our Ag (35nm)/**1** (162 nm) bilayer structure is shown in figure 2.21a at room temperature (25 °C) for various angles of incidence θ_{air}. To trace the curves in figure 2.21, spectra were recorded for both s- and p-polarized incoming light, allowing the results to be presented in terms of the ratio of these reflectances R_s/R_p. The obtained spectra show the existence of both s and p-polarized resonance modes, which appear, respectively, as dips and maxima in the R_s/R_p plots. Importantly, the film thicknesses were chosen (based on simulations) such that the s-polarized resonance mode spans the visible wavelength region as the incidence angle varies over the 42–80° range.

The reflectivity spectra and angular dispersion of the Ag/**1** resonators were simulated using conventional transfer-matrix calculations [Katsidis 2002], the cavity being modelled as a multilayer structure, which consists of semi-infinite space of glass, a layer of silver, a dielectric (SCO) layer and a semi-infinite space of air. The actual angles θ_p at which the incoming beam hits the Ag surface within the prism were obtained from the experimental incident angles in air, θ_{air}, taking into account the refraction of the light beam at the air-prism interface (Snell's law). Calculations were

performed including the known optical properties of N-BK7 glass and silver [McPeak 2015], while the complex refractive index of **1** was taken from Fig. 2.11.

Figure 2.21b and 2.21c show the overall reflectance (R_s/R_p) behavior of the Ag/**1** resonator obtained from experiments and simulations, respectively, in the visible wavelength range (down to the silver plasma frequency at *ca.* 320 nm) through the accessible range of TIR angles. These contour plots show the dispersion curves of both s- and p-type resonance modes, depicted as dark-blue and yellow bands, respectively. The simulated dispersion behavior closely matches the experimental one, albeit with considerably smaller linewidths. Indeed, by way of example, the experimental FWHM of the s-polarized resonance is found to be *ca.* 37 nm (Q-factor ≈ 12), which is much larger than the value predicted by simulations (8 nm). This broadening of the resonances stems from multiple reasons. First, the calculations apply for electromagnetic plane waves, which remains a crude approximation for the large, roughly collimated white light beam used in the experiments. In addition, small inhomogeneities in the film thickness and surface/interface roughness result in an effective increase of the linewidths. From a purely technical point of view, it would be possible to consider these different phenomena in the simulations and one could also use more advanced techniques for the film deposition to obtain a better homogeneity, but these efforts go beyond the scope of the present work.

Instead, our focus was on the investigation of the temperature-dependent (and then SCO-dependent) properties of our resonator, which we explored by assessing the angle- and wavelength dependent s-polarized reflectance of the device upon successive heating-cooling cycles between 25 and 120 °C. As shown in figure 2.22, within this temperature range, the angular dispersion of the s-polarized resonance mode shows a significant shift near the spin transition (between 60 and 80 °C), in particular at large incident angles.

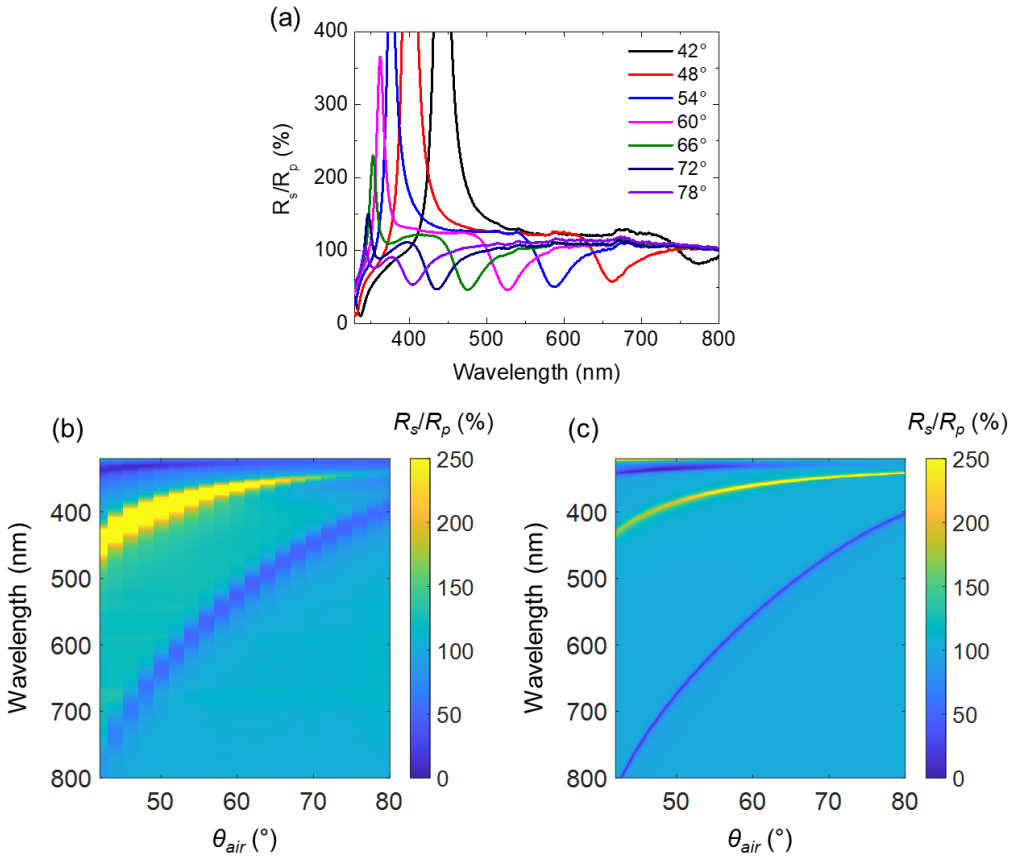

Figure 2.21. (a) Reflectance R_s/R_p spectra recorded at room temperature (25 °C, LS state) at different angles of incidence θ_{air}. Experimental (b) and simulated (c) angular dispersion of the resonator at 25 °C, showing both s (dark-blue band) and p (yellow band) resonant modes.

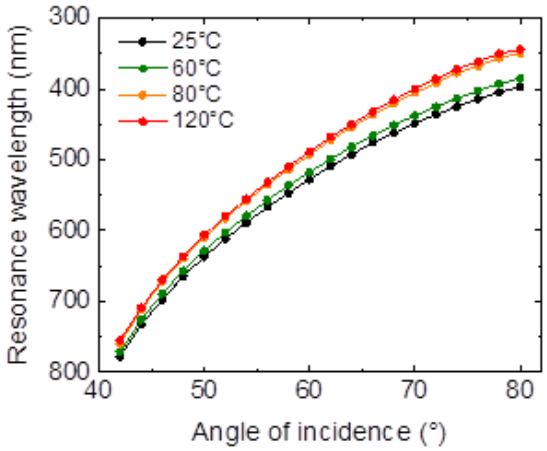

Figure 2.22. Angular dispersion curves of the Ag/**1** bilayer resonator acquired at selected temperatures (s-polarization).

As an example, figure 2.23a displays s-polarized reflectance spectra of the resonator recorded at a fixed angle of incidence, $\theta_{air} = 68°$, for selected temperatures. Importantly, we observe a sizeable blueshift (up to 46 nm) of the resonance peak upon heating from 25 to 120 °C, which, importantly, is found to be larger than the spectral linewidth of the resonant mode (*FWHM* = 37 nm). Besides, it is worth mentioning that most of this spectral shift occurs between 60 and 80 °C.

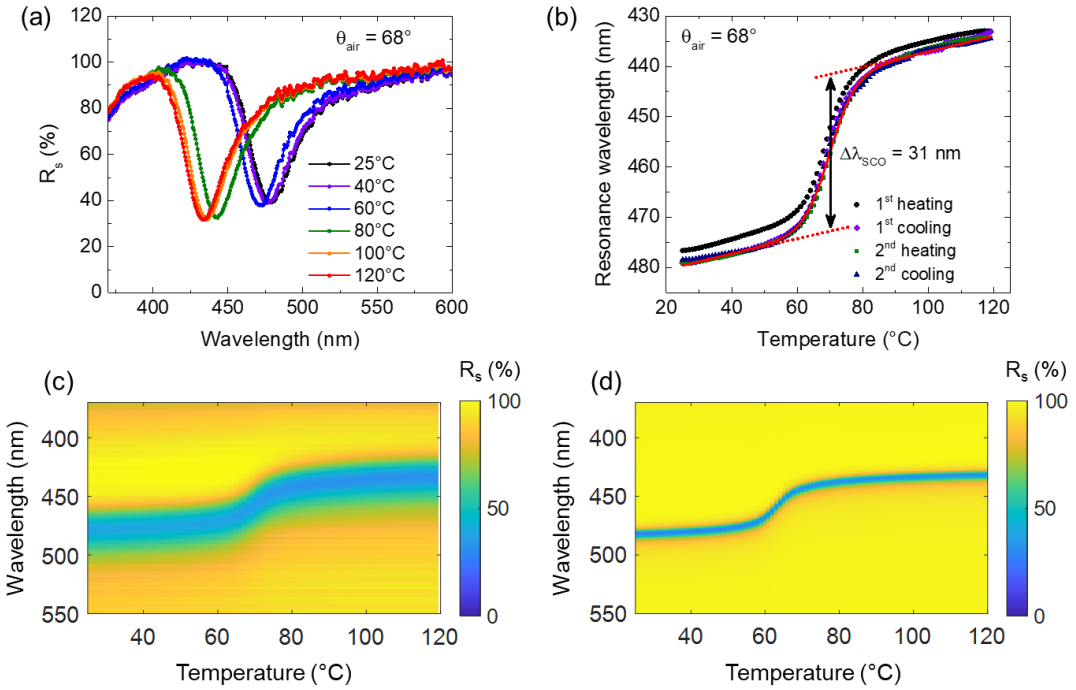

Figure 2.23. (a) Reflectance spectra acquired at selected temperatures (s-polarization, $\theta_{air} = 68°$) showing the blueshift of the resonance peak upon the LS-to-HS transition. (b) Temperature dependence of the resonance wavelength over two heating-cooling cycles (s-polarization, $\theta_{air} = 68°$). Experimental (c) and simulated (d) wavelength-temperature maps of the reflectance, R_s, of s-polarized waves at an angle of incidence of $\theta_{air} = 68°$.

The origin of this phenomenon becomes obvious in figure 2.23b, which shows the detailed variation of the resonance wavelength as a function of temperature at the same angle of $\theta_{air} = 68°$. When heating the device from room temperature, one first observes a small linear blueshift of the resonance, followed by a more abrupt variation (with an inflection point around 70 °C) and, finally, a slowdown above *ca.* 80 °C. Whereas the

smooth linear resonance shifts at low and high temperatures denote ordinary thermoreflectance effects, the abrupt change can be unambiguously ascribed to the SCO phenomenon. (Note that the temperature inflection point is found to be ca. 6 °C higher than the transition temperature of films deposited on bare substrates, certainly due to the occurrence of a thermal lag arising from the large thermal inertia of the prism.) From this figure, one can thus clearly assess the resonance shift, which is associated solely with the spin-state switching ($\Delta\lambda_{SCO} \approx 30$ nm) without any background thermal effects. One may also notice that after the first heating, which is always somewhat anomalous, the next heating-cooling curves overlap closely, denoting a good switching reversibility.

A more complete picture of the temperature dependence of the reflectance R_s of the device can be depicted in figure 2.23c, from which we clearly observe that the SCO-induced shift of the resonance is comparable with the spectral linewidth, thus resulting in spectrally well-separated resonance peaks in the LS and HS states. By injecting refractive index data from Fig. 2.11 into the transfer-matrix calculations, the resonance shifts could be reproduced in our numerical simulations with reasonably good accuracy (see figure 2.23d). One shall note, however, that a quantitative agreement between experiment and theory can be reached only if one takes into account both the refractive index and film thickness changes, accompanying the spin transition. Indeed, the sole decrease of the refractive index of films of **1** by 0.05 upon the LS-to-HS transition is expected to result in a *ca.* 47-nm shift of the resonance wavelength, which considerably exceeds the experimentally observed value of 30 nm. However, if one also takes into account the expansion of the film thickness by 4.7 % upon heating [Rat 2017], the simulations predict a *ca.* 36-nm shift of the resonance wavelength in fair agreement with the experiments. Interestingly, the numerical simulations also revealed that the s-polarized mode used in our experiments provides several advantages in comparison with the p-polarized modes in the context of resonance tuning. Indeed, as shown in figure 2.24, s resonances are, in general, narrower and exhibit a larger shift at the SCO when compared to the p-polarized modes.

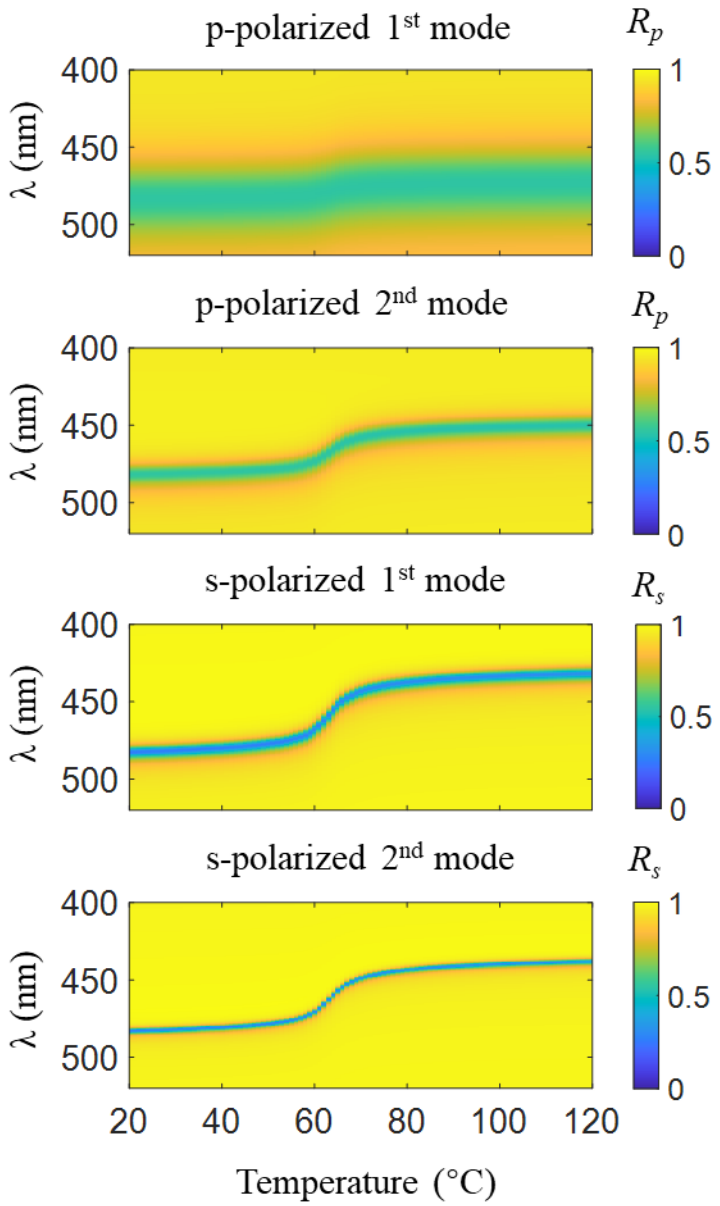

Figure 2.24. Temperature dependent behavior of various simulated Ag/**1** devices displaying different types of resonances near 480 nm (in the LS state) for an angle of incidence of θ_{air} = 68°. The thickness of the SCO layer was set to 31 nm (p, 1st), 285 nm (p, 2nd), 162 nm (s, 1st) and 417 nm (s, 2nd).

These differences are related (at least partly) to the fundamentally different electric field distributions associated with the two types of cavity modes. As discussed in refs. [de Bruijn 1991; Salamon 1997], for p polarization, the electromagnetic field intensity is always high near the metal/dielectric interface, which gives rise to higher damping (associated with metal optical losses), whereas for s polarization the field distribution

peaks within the dielectric layer thereby affording a higher refractive index sensitivity. It is also interesting to note that, in our experiments, we investigate the first-order s resonance of the cavity, which leads to the largest shift at the spin transition, but one might also exploit higher order s resonances, which still provide high sensitivity and strongly reduced linewidths.

2.4.3 Figures-of-merit

As discussed in Section 2.3.4, the shift of the resonance wavelength upon the SCO, $\Delta\lambda$, is an important characteristic of a thermally-tunable optical device, but, from an applicative point of view, other important parameters must also be taken into account, such as the resonance linewidth (*FWHM*), the achievable optical (here reflectance) contrast at a given wavelength, ΔR, and the dependence of these different parameters on any temperature change. Figure 2.25a (top panel) depicts the thermal evolution of the ratio $\Delta\lambda/FWHM$ (the initial position of the resonance at 25 °C being considered as the reference) associated with the s-polarized mode of our Ag/**1** resonator at an angle of incidence of 68°. While the variation of $\Delta\lambda/FWHM$ over the whole temperature range [25–120 °C] reaches a value of -1.22, a fit of the experimental data using a sigmoidal function allows to determine that the effect of the sole SCO induces a change by $\Delta\lambda_{SCO}/FWHM$ = -0.83. This variation, close to unity, means that the SCO-induced spectral shift of the resonance is virtually comparable to the resonance linewidth, which is an important feature to obtain a modulator exhibiting large optical contrast. Figure 2.25a (bottom panel) shows the thermal evolution of the derivative of $\Delta\lambda/FWHM$ with respect to the temperature, which characterizes the thermal spectral sensitivity of the device (always given at an angle of θ_{air} = 68°). Far from the spin-transition temperature, $\Delta\lambda/FWHM$ decreases linearly at a rate of -0.0045 $°C^{-1}$, but is then subject to a strong variation due to the SCO, indicating an increased gain in sensitivity. Indeed, around the spin-transition temperature, the derivative of $\Delta\lambda/FWHM$ reaches a maximum value of -0.065 $°C^{-1}$), which signifies that the thermal sensitivity of the device is multiplied by >10 near the transition temperature, in comparison with the normal shift induced by the ordinary thermal expansion. Another important FOM concerns the achievable

reflectance contrast of the device. As an example, figure 2.25b (top panel) displays the temperature evolution of the reflectance change, $\Delta R = R - R_{25°C}$, measured for s-polarized incoming light at an incident angle of 68° and a wavelength of λ = 434 nm. While the reflectance is virtually constant at low and high temperatures, we notice that most of the reflectance change takes place around the spin-transition. Thus, utilizing our resonator at an angle of 68° and a wavelength of 434 nm, the SCO induces a (s-polarized) reflectance change up to 70 %. The plot depicting the temperature evolution of $d(\Delta R)/dT$ (figure 2.25b, bottom panel) shows that the spin-state switching involves a maximum thermal sensitivity, in terms of reflectance change, equal to -5.2 % $°C^{-1}$.

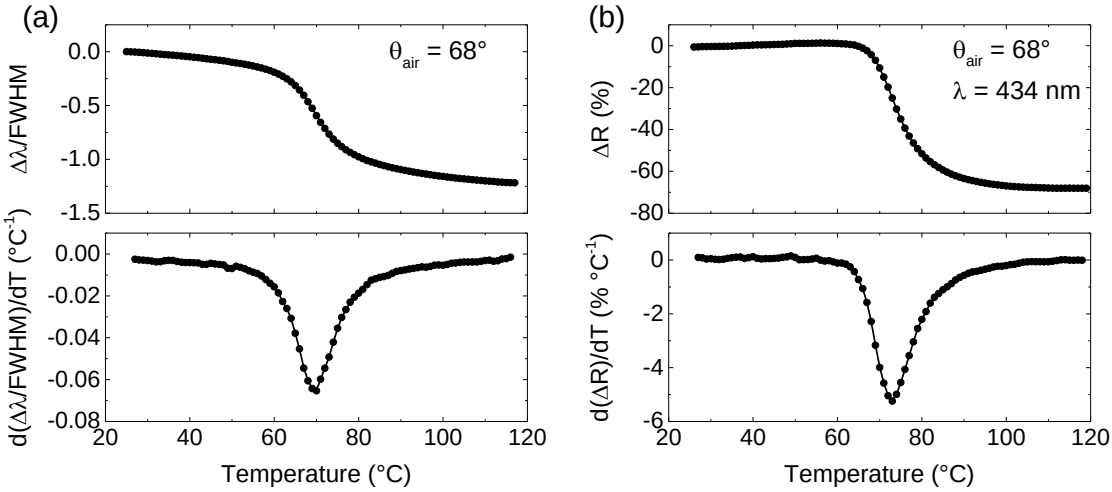

Figure 2.25. Main figures-of-merit of our Ag/**1** resonator. (a) Thermal evolution of the ratio $\Delta\lambda/FWHM$ (top panel) and of its derivative with respect to the temperature (bottom panel), for the s-polarized mode of our Ag/**1** resonator at an angle of incidence of 68°. (b) Thermal evolution of the reflectance change ΔR (top panel) and of its derivative with respect to the temperature (bottom panel), at an incident angle of 68° and a wavelength of λ = 434 nm.

2.4.4 Optical limiting application

In the following, we have taken advantage of the remarkable thermal tunability of our Ag/**1** resonator, to demonstrate its use for optical self-limiting applications in the visible domain. Optical limiters are self-adaptive devices, which exhibit a specific input-output power response. Their response is linear (open state) below a threshold power, but for

higher input powers, the output intensity rise slows down and becomes nearly constant (limiting state) [Parra 2021; Wan 2021]. The main use of optical limiters is the protection of devices and humans against hazardous high-power light beams, but they are also employed in optical computation and other domains, wherever their nonlinear response function can provide benefit [Wan 2021].

To demonstrate optical limiting application, the photothermal heating of the device was achieved by means of a continuous, frequency-doubled Nd:YAG laser (532 nm, incident laser powers between *ca.* 1–22 mW), whose emission was focused on the bilayer resonator by a lens to a diameter of *ca.* 50 µm, allowing incident power densities up to 1.1 kW/cm^2. The incident and reflected laser powers were measured using a photodiode power sensor (S130C, Thorlabs).

Figure 2.26a shows the angular reflectance spectra of our Ag/**1** resonant device recorded at 532 nm at selected temperatures, which basically reflects the same type of behavior as the wavelength spectra displayed in Figure 2.23a, i.e., a pronounced shift of the reflectance "dip" to lower angles when switching the SCO layer from the LS to the HS state. The device was then heated to 60 °C, i.e., only a few degrees Celsius below the spin-transition temperature, and the output optical power was recorded as a function of the input laser power for selected angles of incidence (shown by colored dots in Figure 2.26b on the angular spectrum measured at T = 60 °C). As shown in Figure 2.26c, at lower angles, the response is found to be linear, but for higher angles, a nonlinear behavior is observed and the output power saturates around 6–7 mW. This phenomenon can be clearly linked to the spin-state switching by tracing the reflectance of the device as a function of the input power at the different incident angles (see Figure 2.26d). Indeed, the observed limiting power corresponds to the reflectivity "dip" value ($R \approx 30$ %) measured at the resonance. Overall, the device behaves as a mirror, which limits, in certain conditions, the power of the reflected light below a threshold value (for example to 7 mW at T=60 °C and θ_{air} = 57.5° at λ = 532 nm).

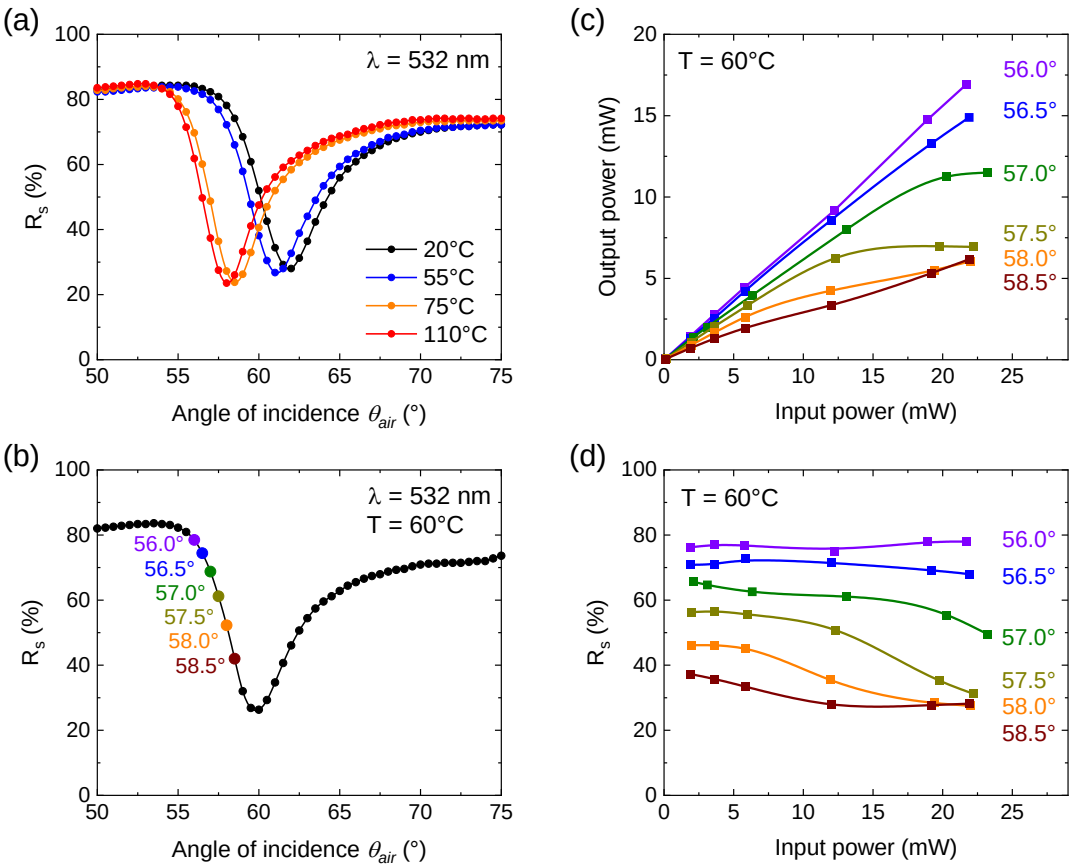

Figure 2.26. (a) Angular reflectance spectra (s polarization) of the Ag/**1** resonator recorded at λ = 532 nm at selected temperatures. (b) Angular spectrum at T = 60 °C displaying the experimental conditions (shown by colored dots) used for the optical limiting experiments. Reflected laser power (λ = 532 nm) (c) and corresponding optical reflectance (d) vs. the incident laser power measured at the different angles of incidence θ_{air} shown in (b) for the Ag/**1** stack held at 60 °C.

For comparison, we repeated the same experiment at 50 °C, i.e., *ca.* 14 °C below the spin-transition temperature, but only ordinary linear response could be observed (see figure 2.27), providing thus further evidence for the origin of the photothermal nonlinearity occurring at 60 °C.

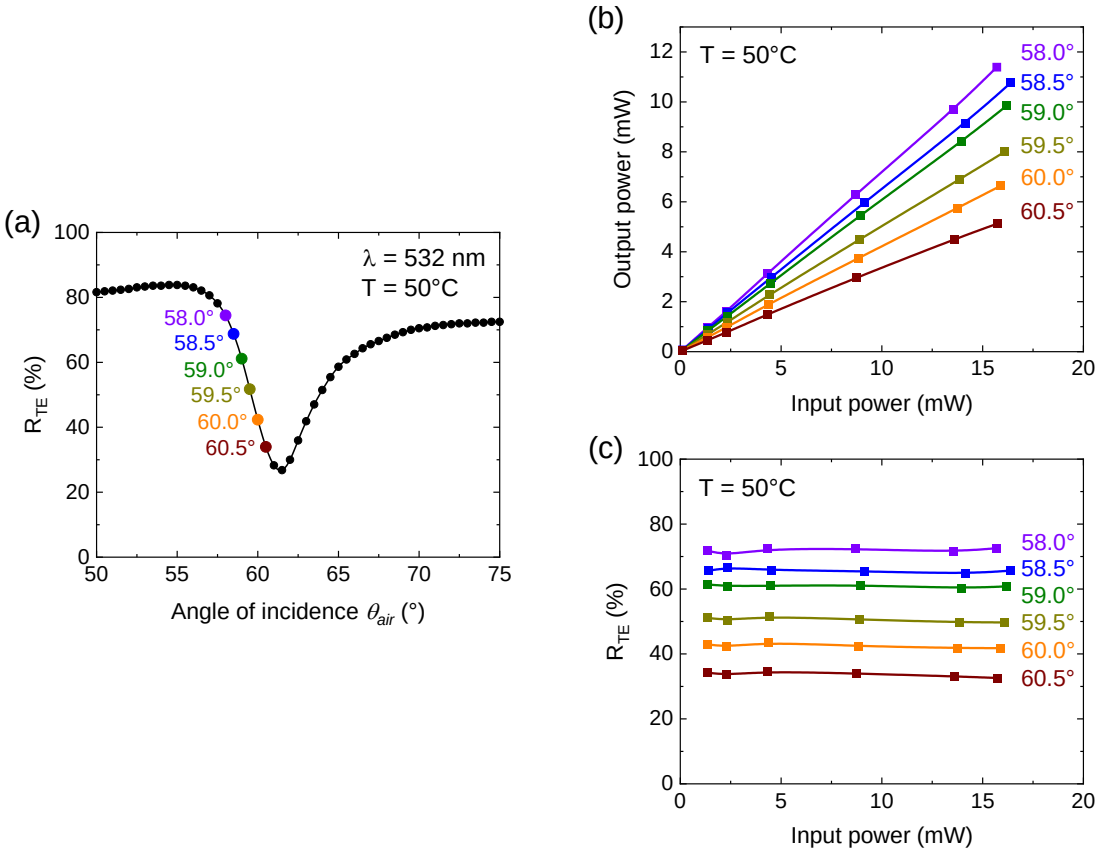

Figure 2.27. (a) Angular reflectance spectrum (s polarization) of the Ag/**1** resonator recorded at λ = 532 nm and T = 50 °C (i.e., *ca.* 14 °C below the spin-transition temperature). Reflected laser (λ = 532 nm) power (b) and corresponding optical reflectance (c) vs. the incident laser power measured at the different angles of incidence, θ_{air}, shown by colored dots in (a). For every angle of incidence, the reflected power is found to increase linearly with the input laser power (i.e., the measured reflectance is constant), indicating that, sufficiently far from the spin-transition temperature, no photothermal nonlinearity is observed (within the incident laser power range investigated).

2.5 Conclusion and discussion

If one compares the two investigated devices, i.e. the Ag (40 nm)/**1** (142 nm)/Ag (40 nm) Fabry–Pérot cavity and the Ag (35 nm)/**1** (162 nm) resonator, it appears that they have the same refractive-index-changing material and comparable conditions of fabrication. However the comparison of their optical tunability (see figure 2.28) reveals a 6 times higher refractive index sensitivity for the Ag (35 nm)/**1** (162 nm) resonator,

while keeping fairly similar values of quality factors. As for the optical contrast, the maximum transmittance change was found to be ΔTr = 3 % for the Ag (40 nm)/**1** (142 nm)/Ag (40 nm) cavity, compared to ΔR = 68 % for the Ag (35 nm)/**1** (162 nm) resonator. Overall, the different figures-of-merit measured for the Ag /**1** resonator to characterize its tunability are substantially superior to those obtained for the Ag/**1**/Ag cavity, incorporating the same SCO material. Thus, these considerations show that, for a given refractive-index-changing material and comparable conditions of fabrication, the design of the resonator is of great importance to obtain large optical contrast.

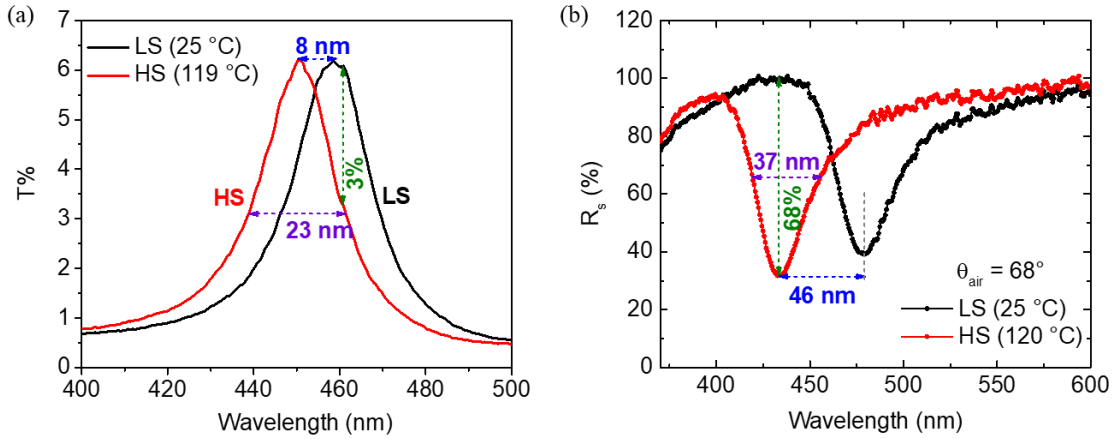

Figure 2.28. (a) Transmittance spectra acquired in the HS and LS states (s-polarization, θ_{air} = 60°) for the Ag (40 nm)/**1** (142 nm)/Ag (40 nm) cavity. (b) Reflectance spectra acquired in the HS and LS states (s-polarization, θ_{air} = 68°) for the Ag (35 nm)/**1** (162 nm) resonator. For both device, the resonance shifts, the resonance widths and the optical modulations are shown by dashed arrows.

The optical modulation performance of our SCO-based resonators can be tentatively compared with the characteristics of optical resonators incorporating other solid-solid PCMs, such as GST and VO_2. These two commonly-used materials have notably been employed as switching elements in silicon-based microring resonant cavities (see for example, Figures 2.1 and 2.2) [Briggs 2010; Pernice 2012; Ryckman 2012; Rudé 2013; Zheng 2018; Miller 2018], working in the telecommunication C-band (around λ = 1550 nm). In these devices, the phase transition of the PCM layer, deposited onto the microring resonator, modifies the effective complex refractive index of the hybrid

waveguide, enabling a controlled modification of the resonance conditions of the microring device. However, beyond the fact that these resonators have very different designs (compared with our SCO-based devices), a rigorous comparison of the optical performance is delicate because the modulation of the optical signal in GST and VO_2 resonators is based *both* on the switching of the real part of the PCM refractive index (phase modulation), and on the change of the extinction coefficient (amplitude modulation). Indeed, both GST and VO_2 exhibit a significant variation of n and k upon the phase transition (see Figure 2.3), so that the shift of the resonance wavelength is also accompanied by a strong modification of the absorption losses and quality factor of the cavity (see Figures 2.1 and 2.2). In some cases, the large absorption loss can even completely extinguish the cavity resonances in the absorbing phase [Briggs 2010]. The situation is different in our SCO-based resonator, since the films of **1** exhibit negligible optical absorption losses ($k < 10^{-3}$) in both spin states. As a consequence, it appears that all the observed optical changes are exclusively based on phase modulation of travelling optical waves, the resonator Q-factor being not affected by the SCO (see Figure 2.28). Bearing in mind these fundamental differences, a normalized shift of the resonance wavelength, $|\Delta\lambda|/FWHM$, within the range 0.5–0.8 was demonstrated in the reported GST- and VO_2-based resonators [Ryckman 2012; Rudé 2013], which appears to be similar (and even smaller) to what is observed in our SCO-based resonator. In fact, in these clad waveguide cavities, the spectral shift of the resonance is limited by the reduced confinement of the optical mode within the PCM layer, which results in a limited change of the modal effective index of the cavity upon the phase transition. On the contrary, in our SCO-based devices, the low extinction coefficient of **1** allows us to design a resonator, in which a large fraction of the optical field overlaps with the active SCO layer, enabling a high sensitivity of the device to the refractive index change accompanying the SCO. On the other hand, in GST- and VO_2-based resonators, optical modulation depths greater than 10 dB are achieved (arising from both phase and amplitude modulation) [Pernice 2012; Ryckman 2012; Rudé 2013; Zheng 2018], but, however, with relatively large insertion losses of ~2 dB (due to the residual optical

absorption of the PCM, even in the low-absorbing phase), which means that the maximum transmittance (reflectance) change is typically limited to only ~60 %. In comparison, the optical modulation depth in our resonator is smaller (5.2 dB, since *R* varies from 100 to 30 %), but the total variation of the reflectance is comparatively larger (70 %) due to negligible insertion losses.

In conclusion, we can say that the Ag (35 nm)/**1** (162 nm) resonator, designed to have a large modal overlap with the switchable molecular layer, allowed to reach high figures-of-merit in terms of resonance spectral shift and reflectance contrast tuning. The performance of our device is comparable with that reported for well-established phase-change materials, but with a major benefit, which is the seamless device operation in the visible wavelength range. As a proof-of-concept, we demonstrated optical limiting properties at 532 nm, arising from the photothermal nonlinearity of the resonator. However, more generally, the present work also opens appealing scopes for various reconfigurable and/or adaptive photonic applications, including spatial light modulators, photonic integrated circuits and tunable optical components – with particular relevance for the visible wavelength range wherein other families of PCMs fall short.

Chapter 3. Switching between ultra-strong and weak light-matter coupling using spin-crossover molecules

Chapter 3. Switching between ultra-strong and weak light-matter coupling using spin-crossover molecules

In the previous chapter, the fabricated optical resonators were designed in such a way as to obtain the resonant mode in the visible range, wherein our SCO compounds are fully transparent in both spin states. In this case, we have demonstrated the possibility to spectrally shift a cavity resonance (and then to modulate an optical signal) via the change of the refractive index of the SCO material upon the spin transition. In this chapter, we will implement, for the first time, an approach, which consists in designing an optical resonator in such a way that one optical mode falls in the UV wavelength domain, where our molecular compounds display intense, spin-state dependent absorption bands. In other words, the main idea now is to put in resonance a cavity mode with a molecular excitation, with the aim of achieving (and exploiting) a ***regime of strong light-matter coupling*** between the photonic structure and the SCO molecules. Since the molecular excitations (or absorption bands) are different in the two spin states, the spin transition is expected to offer a means to modulate the coupling strength between the molecules and the optical resonator. To explore this exciting new avenue, we used two isomeric SCO molecules with different spin transition properties: the complex [Fe(HB(1,2,4-triazol-1-yl)$_3$)$_2$] **1** and the complex [Fe(HB(1,2,3-triazol-1-yl)$_3$)$_2$] **2**, displaying abrupt and gradual SCO, respectively. We used a similar resonator as in Chapter 2, employing a prism as the coupling medium, coated with a metal/SCO bilayer. However, since the molecular resonances occur in the UV spectral region, we employed fused silica prisms (instead of glass) and we replaced silver with aluminium, which is the privileged metallic mirror in the UV.

3.1 Introduction to the strong light-matter coupling

A shown in Figure 3.1, when a molecular excitation comes into resonance with a cavity mode, rapid energy exchange (through the exchange of photons) can occur between the

optical cavity and the material. Especially, if this energy exchange becomes faster than any dissipation (cavity-photon leakage) or decoherence (molecular dephasing) process, then the so-called strong-coupling regime arises between matter and the surrounding electromagnetic (EM) field. In this case, new hybrid light-matter states (with mixed molecular and photonic character) – known as polaritons – are formed, with an energy separation (called Rabi-splitting energy, $\hbar\Omega_R$) being proportional to the coupling strength [Hutchison 2012; Törmä 2014]. The coupled {molecules + cavity} system must then be thought as a single entity with new energy levels, and exhibiting unusual physico-chemical properties. An appealing feature is that this light-matter hybridization occurs even in the absence of light (photons) inside the cavity ($n_{ph} = 0$), the coupling taking place with the vacuum fluctuations, i.e., the finite zero-point energy of the quantized EM field in the cavity [Ebbesen 2016]. Indeed, the Rabi-splitting energy, $\hbar\Omega_R$, is given by the following formula:

$$\hbar\Omega_R = \hbar\Omega_{VR}\sqrt{n_{ph} + 1} \tag{11}$$

where n_{ph} is the number of photons involved in the coupling process within the cavity, while $\hbar\Omega_{VR}$ is the so-called vacuum Rabi-splitting energy which is given by

$$\hbar\Omega_{VR} = 2\sqrt{N\left(\vec{d}\cdot\vec{E}\right)^2 - \frac{1}{4}(\Gamma_{cav} - \Gamma_{ex})^2} \tag{12}$$

where N is the number of molecules coupled to the same cavity mode, $\vec{E}$ is the confined electrical field, $\vec{d}$ is the material transition dipole moment, while Γ_{cav} and Γ_{ex} are the resonance linewidths of the cavity mode and the molecular excitation, respectively. Interestingly, from Eq. (12), we find that the Rabi-splitting energy is maximum when the cavity mode and exciton linewidths are equal $\Gamma_{cav} = \Gamma_{ex}$. In this case, as the electric field associated with a cavity mode is proportional to $1/\sqrt{V}$ (V being the mode volume), it appears that the vacuum Rabi-splitting energy is proportional to $\sqrt{N/V}$, i.e. proportional to the square root of the concentration C of absorbing molecules ($\hbar\Omega_{VR} \propto \sqrt{C}$) [Wang 2014].

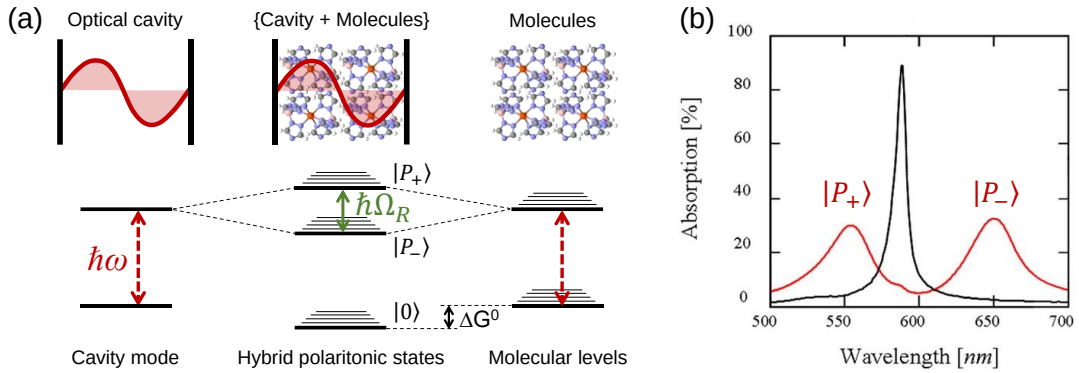

Figure 3.1. (a) Simplified energy landscape of a {molecules + cavity} system in strong-coupling regime. The resonance between the molecular excitation (electronic or vibrational) and the cavity mode $\hbar\omega$ leads to the formation of two hybrid light-matter (polaritonic) states, $|P_+\rangle$ and $|P_-\rangle$, separated by the so-called Rabi-splitting energy $\hbar\Omega_R$. Interestingly, the absolute energy of the ground level of the coupled system may also be modified (ΔG^0) by the strong coupling. (b) Experimental absorption spectrum of a cyanine dye molecule before (black curve) and after (red curve) undergoing strong light-matter coupling with a cavity [Ebbesen 2016].

From a spectroscopic point of view, the ***strong-coupling regime*** is said to be achieved when the splitting energy between the two polaritonic states is larger than the spectral linewidths of the cavity mode and of the molecular excitation, i.e. $\hbar\Omega_R > \Gamma_{cav}, \Gamma_{ex}$ [Ebbesen 2016; Garcia-Vidal 2021]. The later condition indeed indicates that the energy exchange rate between the cavity mode and the molecules is faster than the loss rates, which can arise both from the finite lifetime of photons in the cavity (given by Γ_{cav}) and/or from the finite lifetime of the molecular exciton (given by Γ_{ex}). In the opposite case, when $\hbar\Omega_R < \Gamma_{cav}, \Gamma_{ex}$, the exchange rate of energy is smaller than the loss rates (the excitation is lost before it can be shared between the molecule and the cavity), and the system is said to operate in the ***weak-coupling regime***. In the extreme case where the Rabi-splitting energy becomes a sizeable fraction (> 10 %) of the molecular excitation energy involved in the coupling, the system is said to enter the so-called ***ultra-strong coupling (USC) regime*** and the energy levels of the other states (including the ground state) are also modified (see Figure 3.1) [Canaguier-Durand 2013].

The field of polaritonic chemistry, wherein molecular systems are studied under the regime of strong light-matter coupling, has become the topic of intense experimental

and theoretical research over the past decade [Ebbesen 2016; Ribeiro 2018; Dovzhenko 2018; Hertzog 2019; Herrera 2020; Garcia-Vidal, 2021]. This field aims at manipulating chemical structures and reactions (aspiring to achieve novel molecular functionalities), through the formation of hybrid light-matter states between organic molecules and confined electromagnetic modes of optical nano-/micro-cavities. This regime of strong coupling can be achieved by placing an ensemble of molecules in a photonic structure or an optical cavity (e.g. Fabry-Pérot cavities, plasmonic structures, etc.), designed such that one of the cavity modes is resonant with a molecular excitation [Lidzey 1998], resulting in a coherent, oscillatory exchange of energy between the cavity and the material. In that regard, organic molecular systems are of particular interest because exceptionally large vacuum Rabi-splitting energies (hundreds of meV) [Schwartz 2011] can be achieved due to their large transition dipole moments (i.e. large absorption extinction coefficients) and high possible density of integration in the cavity. This allows the (ultra-)strong coupling regime to be achieved in relatively low quality-factor cavities ($Q \approx 10$) [Schwartz 2011; Hobson 2002].

The field of polaritonic chemistry is burgeoning both in interest and importance as it provides a fascinating tool to tune the energy landscape of the coupled system, and then to modify the physico-chemical properties of molecules or molecular materials [Ebbesen 2016; Ribeiro 2018; Dovzhenko 2018; Hertzog 2019; Herrera 2020; Garcia-Vidal 2021]. In the following, we illustrate this appealing potential of polaritonic chemistry through a few selected examples.

As a first example, it has been shown that strong light-matter coupling can significantly increase the electrical conductivity of organic semiconductors [Orgiu 2015]. This was demonstrated for thin films of the semiconductor PDI2EH-CN_2 deposited on top of a hexagonal array of holes milled in a 100-nm-thick Ag film, which gives rise to well-defined surface plasmon resonances that can be tuned by varying the period P of the array (Figure 3.2a).

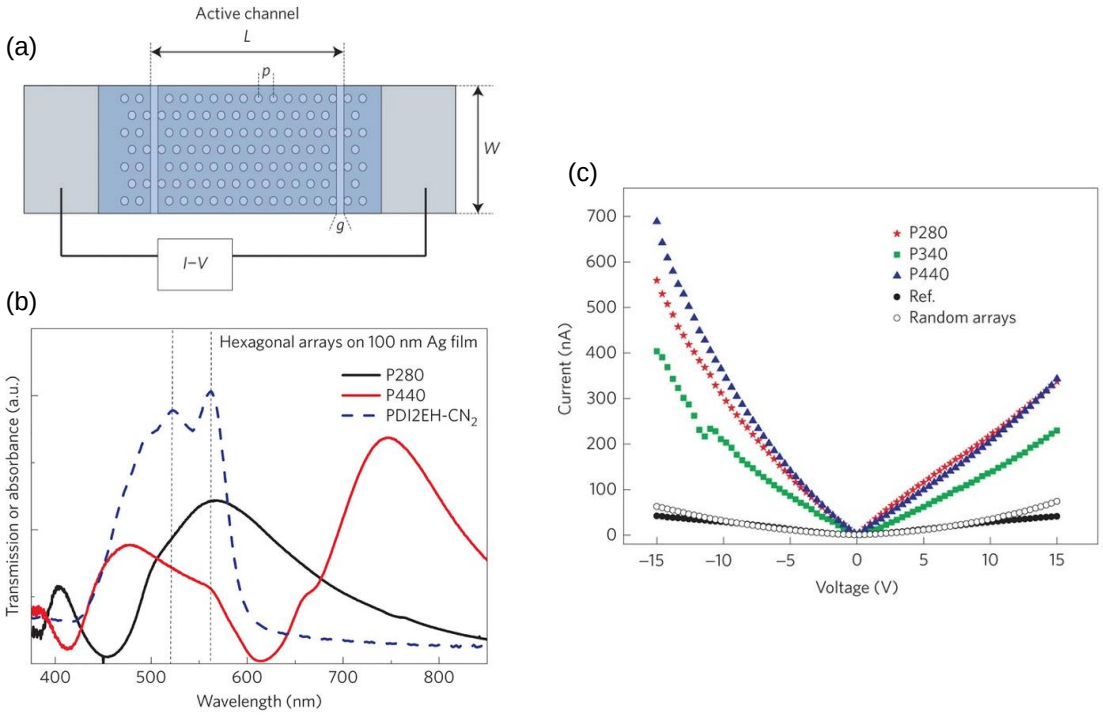

Figure 3.2. (a) Illustration of the configuration used to measure electrical conductivity using surface plasmon resonances generated by a hexagonal array milled in a 100-nm-thick Ag film (deposited on a glass substrate). This array was then coated with a film of the organic semiconductor (PDI2EH-CN_2). (b) Absorbance spectra of a thin film of PDI2EH-CN_2 (dashed blue) and examples of resonances of two hole arrays with different periods (named P280 and P440) whose resonance matches the material absorbance. (c) I-V curves for different hexagonal arrays (with selected periods) covered by PDI2EH-CN_2. A sizeable increase of the electrical current is observed in strongly-coupled systems (P280, 340 and 440) compared to an unstructured metal film (Ref.) and a system with random arrays of holes in which there are no well-defined plasmon resonances (Random arrays) [Orgiu 2015].

By coupling these surface plasmon resonance modes to the intense absorption bands of the organic semiconductor (see Figure 3.2b), it was shown that a sizeable increase of the electrical conductivity of the material can be achieved. Indeed, as shown in Figure 3.2c, a more than one order of magnitude increase of the electrical current is obtained when the organic semiconductor is strongly coupled with the surface plasmon modes, compared to uncoupled systems. This increase of the electrical conductivity was attributed to an enhancement of the charge carrier mobility under strong coupling, which in turn arises from the enhanced spatial delocalization (over lengths

corresponding to the mode volume) of the states induced by the light-matter hybridization. Indeed, polaritonic states are coherent states that can extend over as many as 10^5 molecules, in contrast to the 'normal' situation where the carriers are mostly confined to the molecular scale (or a few molecules).

Interestingly, light-matter hybridization is not limited to electronic excitations of molecules. Indeed, as shown in Figure 3.3a, molecular vibrations can also strongly couple to infrared (IR) EM fields leading to the formation of vibrational or phonon polaritons [Shalabney 2015; Thomas 2016; Hirai 2020; Nagarajan 2021]. This so-called vibrational strong coupling (VSC) offers exciting possibilities for the selective control of chemical bond energies, which has been recently much investigated for tuning chemical reactivity [Ebbesen 2016; Hertzog 2019]. Indeed, strong coupling of the vibrational mode entails a modification of the bond strength, which can be used to alter both the thermodynamics and kinetics of reactions. This effect of VSC on the reactivity of chemical bonds was demonstrated, for example, in the case of the deprotection reaction of an alkynylsilane, 1-phenyl-2-trimethylsilylacetylene (PTA), with tetra-*n*-butylammonium fluoride (TBAF) (see Figure 3.3b) [Thomas 2016]. The kinetics of this reaction was studied inside a microfluidic IR Fabry–Perot cavity, which consists of two parallel mirrors separated by a distance of around 6 µm, that was tuned to be in resonance with the stretching mode of the C–Si bonds of PTA around 860 cm^{-1}. As depicted in Figure 3.3c, the occurrence of the strong coupling regime was confirmed through the observation of a spectral splitting of the C–Si stretching mode with a Rabi splitting of 98 cm^{-1}. (Note that the C≡C vibrational mode at 2160 cm^{-1} also interacts with another cavity resonance (of higher order) but the weak splitting energy value does not meet the criterion for strong coupling.) As the reactant and products of the chemical reaction have different refractive indices, the kinetics of the reaction could be followed by measuring the shifts of the cavity resonances far from any vibrational absorption. Interestingly, as shown in Figure 3.3d, the reaction rate constant is found to decrease by a factor up to 5.5 under VSC, compared to the rate observed when the reaction takes place in an OFF-resonance cavity or outside the cavity. In other words, a

notable slowing down of the reaction kinetics is observed when the stretching mode of the C–Si bonds is strongly coupled to the cavity. Importantly, the relative change of the reaction rate under VSC was found to depend on the value of the Rabi-splitting energy.

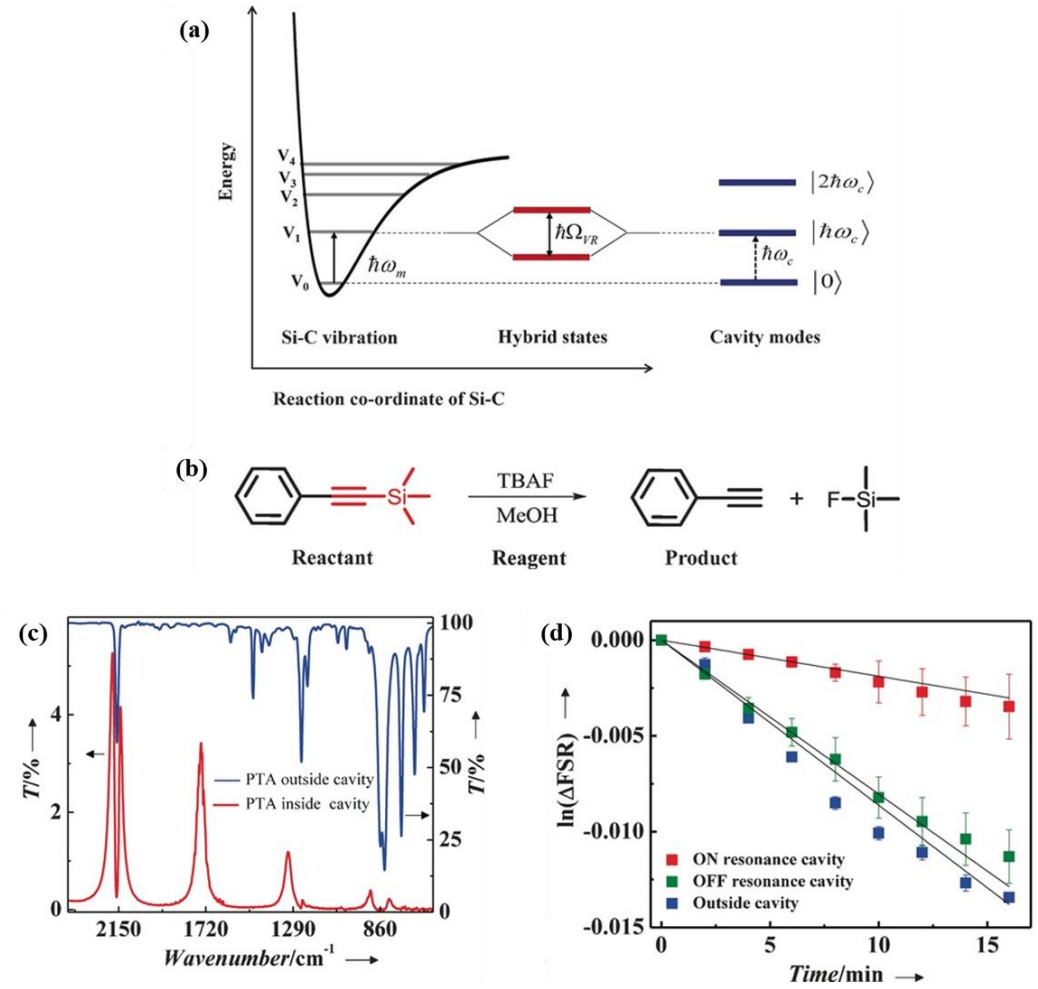

Figure 3.3. (a) Schematic illustration of the strong light-matter coupling between the Si−C stretching vibrational mode and a cavity mode resulting in the Rabi splitting. (b) The silane deprotection reaction of 1-phenyl-2-trimethylsilylacetylene (PTA) with tetra-*n*-butylammonium fluoride (TBAF) in methanol. (c) IR transmission spectrum of PTA inside (red trace) and outside (blue trace) the ON-resonance cavity. (d) Kinetics of the deprotection reaction, extracted from the temporal shifts of the higher-order cavity modes, in an ON-resonance cavity (red squares), outside the cavity (blue squares), and in an OFF-resonance cavity (green squares) [Thomas 2016].

3.2 Strong light-matter coupling in Fabry-Perot cavities incorporating Rhodamine B molecules

As a first step, to better assess the phenomenon of strong light-matter coupling in

photonic cavities and to validate our experimental setup for optical characterization, we have investigated the effect of light-matter hybridization in Ag-based Fabry-Perot cavities incorporating Rhodamine B (RhB) dye molecules dispersed into a poly(methyl methacrylate) (PMMA) polymer matrix. We have chosen RhB because it is a well-known, commonly-used dye, which exhibits an intense absorption band in the green spectral range at 556 nm (see Figure 3.4a). As shown in Figure 3.4b, the fabricated Fabry-Perot cavities consist in a PMMA:RhB layer (≈ 150 nm) sandwiched between two Ag mirrors (≈ 40 nm). Given the refractive index of PMMA (n_{PMMA} = 1.49), the thickness of the PMMA:RhB layer (150 nm) was chosen so as to bring the fundamental resonant mode of the cavity ($\lambda/2$ mode) at $\lambda \approx 600$ nm in normal incidence, i.e., a wavelength close to the absorption wavelength of RhB molecules. Four Fabry-Perot cavities were fabricated and characterized. Cavity **0**, which serves as a reference, is made of pure PMMA (without RhB). The three other cavities (cavities **1**, **2** and **3**) incorporate RhB in the PMMA layer with different concentrations (see Table 3).

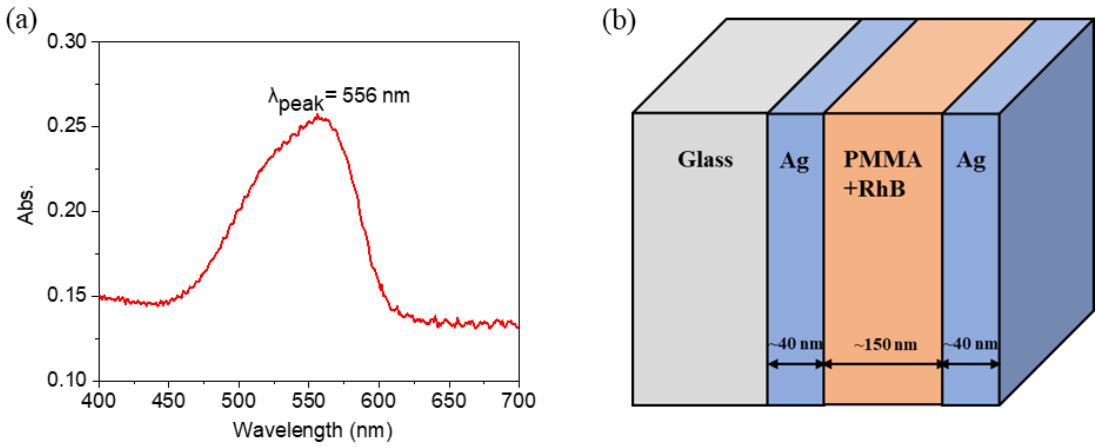

Figure 3.4. (a) Optical absorbance of a RhB film deposited on a fused-silica substrate. (b) Scheme of the fabricated RhB-based Fabry-Perot cavities.

The fabrication of the Fabry-Perot cavities was performed as follows. A first layer of Ag (40 nm) was deposited on fused-silica substrates by vacuum thermal evaporation. The film thickness was controlled by AFM (SmartSPM, Horiba). In the next step, PMMA films doped with RhB (with different concentrations) were deposited by spin coating. For this, different concentrations of PMMA (average molecular weight 35000)

in toluene and different concentrations of RhB in ethanol were prepared and mixed to obtain the following solutions:

Solution 0: 1.52 mM PMMA, 1000 μL;

Solution 1: 500 μL, 2.1 mM PMMA and 500 μL, 30 mM RhB were mixed uniformly under sonication to obtain a RhB solution with a concentration of 7.18 mg/mL;

Solution 2: 500 μL, 1.83 mM PMMA and 500 μL, 40 mMRhB were mixed uniformly under sonication to obtain a RhB solution with a concentration of 9.58 mg/mL;

Solution 3: 500 μL, 1.7 mM PMMA and 500 μL, 50 mM RhB were mixed uniformly under sonication to obtain a RhB solution with a concentration of 11.98 mg/mL.

The above four solutions were spin-coated (rate: 6000 rpm, time: 60 s) on the top of the first Ag layer to obtain a 150-nm-thick film. The samples were then placed in an oven at 105 °C for 3 minutes. The thickness of PMMA:RhB films was controlled by spectral reflectance measurements (Filmetrics, F20). Finally, a second layer of Ag (40 nm) was deposited on the organic layer.

Table 3. Concentrations of RhB in our four Fabry-Perot cavities

Fabry−Perot cavities	C_{RhB} (mg/ml)
Cavity **0**	0
Cavity **1**	7.18
Cavity **2**	9.58
Cavity **3**	11.98

The spectroscopic properties of the cavities were investigated at room temperature by acquiring transmittance and reflectance spectra, under s-polarized illumination, as a function of the incident angle θ_{air}. Figure 3.5a shows the angular dispersion of cavity **0** (incorporating only PMMA) measured in transmission mode. As expected, a well-defined resonance is observed around $\lambda \approx 600$ nm in normal incidence, with a quality factor of $Q = 22$. The resonance peak displays a blue shift upon increasing the angle of incidence, so that the cavity resonance spans the 500–600 nm wavelength range when

varying the angle between 0 and 60°.

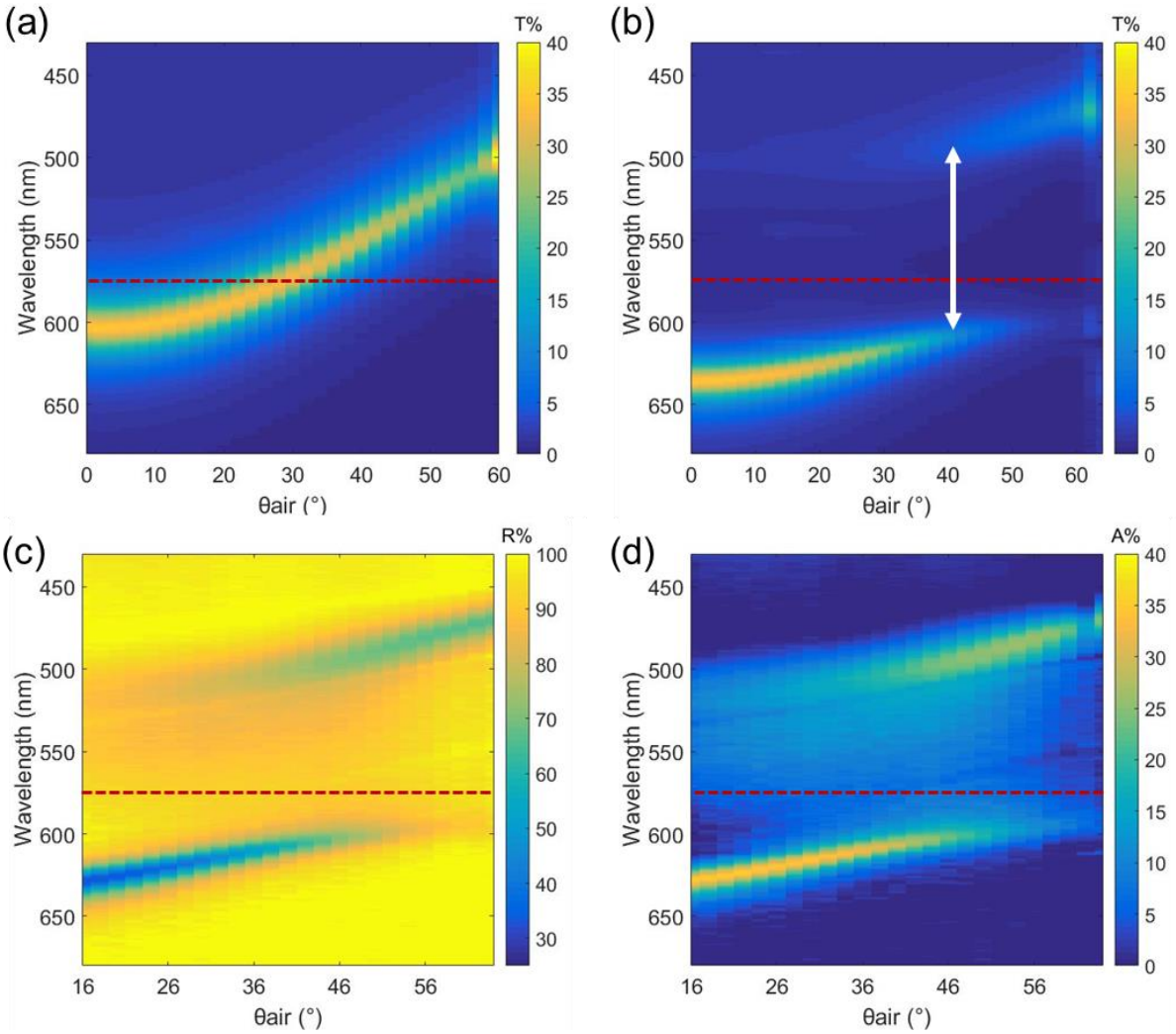

Figure 3.5. (a) Dispersion curve of cavity **0** (pure PMMA) for the s-polarized mode, measured in transmission. This shows the classical dispersion behavior of a Fabry-Perot cavity. **(b)** Dispersion curve of cavity **2** for the s-polarized mode measured in transmittance *T%*. The vertical double arrow indicates the polaritonic splitting for the s-polarized mode. (c) Dispersion curve of cavity **2** for the s-polarized mode measured in reflectance *R%*. (d) Absorptance *A%* spectra of cavity **2** (obtained as $A\% = 1 - T\% - R\%$). The absorption maximum of RhB at $\lambda = 556$ nm is depicted by the horizontal red dashed lines.

By way of comparison, Figures 3.5b, 3.5c and 3.5d display the angular dispersion of cavity **2** (incorporating RhB) measured in transmittance *T%* (Figure 3.5b), reflectance *R%* (Figure 3.5c) and absorptance *A%* (Figure 3.5d), the latter being deduced from the following relation: $A\% = 1 - T\% - R\%$. The absorption maximum of RhB is depicted

by the horizontal red dashed lines. On these graphs, we can clearly observe that the s-polarized photon mode of cavity **2** is split into two branches at a wavelength corresponding to the absorption peak of RhB molecules. Such a splitting (also called 'avoided crossing' or anticrossing) in the dispersion of the cavity is the typical feature of a strong light-matter coupling between the molecules and the cavity mode, the split bands corresponding to the hybrid polaritonic states P_+ and P_-. To examine the coupling strength and the value of the Rabi-splitting energy, we need to plot the measured angular spectra as a function of the in-plane wave vector k_x, the latter being related to the wavelength and the angle of incidence by the relation $k_x = (2\pi / \lambda) \sin(\theta_{air})$. In Figure 3.6, we have plotted the extrema energies of the transmittance and absorptance spectra (for the s-polarized mode) as a function of the in-plane wave vector for cavities **1**, **2** and **3**. As shown in Figure 3.6, a clear anticrossing behavior of the s-polarized cavity mode is observed at an energy $E \approx 2.3$ eV (marked by horizontal dashed lines), which corresponds to the main absorption band of RhB molecules. In order to evaluate the strength of the light-matter coupling, a quantum mechanical coupled-oscillator model was employed to fit the experimental dispersion curves, based on the following Hamiltonian:

$$\hat{\mathcal{H}} = \begin{pmatrix} E_{cav}(k_x) & \hbar\Omega_R/2 \\ \hbar\Omega_R/2 & E_{ex} \end{pmatrix} \tag{13}$$

where $E_{cav}(k_x)$ is the dispersion relation of the bare cavity mode, E_{ex} is the dispersionless exciton mode of the molecules and $\hbar\Omega_R$ is the Rabi-splitting energy. The in-plane dispersion of a photon mode in a Fabry-Perot cavity is typically given by [Hertzog 2019]:

$$E_{cav}(k_x) = \frac{\hbar c}{n_{cav}} \sqrt{{k_x}^2 + \left(\frac{m\pi}{L}\right)^2} \tag{14}$$

where n_{cav} is the background refractive index of the cavity, L is the cavity thickness (i.e. the distance between the metal mirrors) and m is the cavity mode number. The dispersion relation of the two polaritonic branches of the coupled system, noted E_+ and E_-, are given by the eigenvalues of the Hamiltonian (Eq. 13)

$$E_+(k_x) = \frac{E_{cav}(k_x) + E_{ex}}{2} + \frac{1}{2}\sqrt{(\hbar\Omega_R)^2 + (E_{cav}(k_x) - E_{ex})^2}$$
$$E_-(k_x) = \frac{E_{cav}(k_x) + E_{ex}}{2} - \frac{1}{2}\sqrt{(\hbar\Omega_R)^2 + (E_{cav}(k_x) - E_{ex})^2} \quad (15)$$

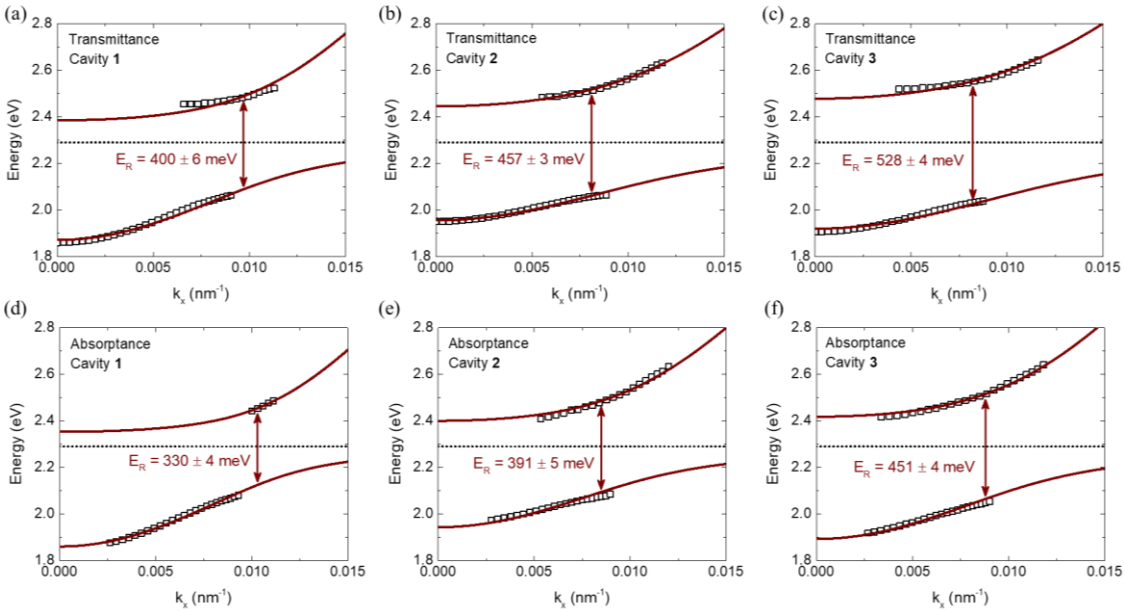

Figure 3.6. Dispersion (energy vs. in-plane wave vector) curves of cavities **1**, **2** and **3** (s-polarized mode), incorporating RhB. (a), (b) and (c) Measured dispersion curves of the three cavities obtained from transmittance measurements. (d), (e) and (f) Dispersion curves of the three cavities obtained from absorptance. The horizontal dashed lines at 2.3 eV indicate the dispersionless molecular excitation energy.

We used Eq. (14) and Eq. (15) to fit the dispersion curves of the coupled cavities shown in Figure 3.6 (red solid lines). For each cavity, this fitting procedure allows to extract a Rabi-splitting energy value $\hbar\Omega_R$. The Rabi-splitting energies of cavities **1**, **2**, and **3** extracted from the dispersion curves measured by transmittance are 400, 457, and 528 meV, respectively. Similarly, the Rabi-splitting energies of cavities **1**, **2**, and **3** extracted from the absorptance dispersion curves are found to be 330, 391 and 451 meV, respectively. Such a difference in the observed splitting energies extracted from transmittance and absorptance spectra is a known feature of Fabry-Perot cavities. Indeed, it is known that the splitting value depends on the type of measurement (e.g. transmittance or absorptance) [Savona 1995]. As the three cavities incorporate RhB molecules with different concentrations, it is possible to investigate the evolution of the

Rabi-splitting energy, extracted from the fitting procedure shown in Figure 3.6, as a function of the concentration C of RhB molecules inside the cavity. Interestingly, as displayed in Figure 3.7, the Rabi-splitting energy is found to be proportional to the square root of the concentration of RhB molecules, which is an expected feature of the strong coupling regime. Furthermore, as noted earlier, the splitting value extracted from transmittance measurements is systematically larger than the value obtained via the absorptance spectra.

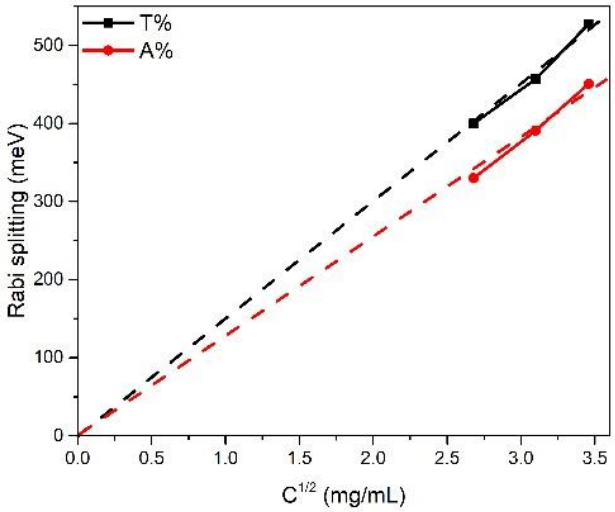

Figure 3.7. Evolution of the Rabi-splitting energy, extracted from the fitting procedure shown in Figure 3.6 (solid lines) for transmittance and absorptance spectra, as a function of the square root of the concentration of RhB in the three cavities.

3.3 Towards tunable light-matter coupling using switchable molecules

Within the field of polaritonic chemistry, the use of switchable, stimuli-responsive molecules as active materials offers an additional degree of freedom and opens up considerable perspectives to reversibly activate/deactivate the strong-coupling regime in a single photonic cavity and then modulate the cavity resonance conditions, which could provide appealing prospects for active tuning and dynamical device reconfiguration. Indeed, as the strong-coupling effect modifies the resonant conditions of optical cavities, it may be possible to use this phenomenon with the aim of modulating light propagation in photonic devices [Benz 2013], instead of using

conventional refractive index switching. More generally, the study of the strong-coupling phenomenon with switchable molecules also opens new perspectives to explore the synergetic effects that can exist between light-matter hybridization and molecular bistability. Examples for strong-coupling regime with switchable materials mostly include so far photochromic molecules (especially spiropyrans) [Schwartz 2011; Hutchison 2012; Hutchison 2013; Baudrion 2013; Lin 2016; Asamoah 2020; Thomas 2022], but also a few phase-change materials [Wang 2014b; Ashida 2020; Chang 2020]. In a pioneering work, Schwartz et al. [Schwartz 2011] studied the reversible switching of the ultrastrong light-matter coupling in multilayer Fabry-Perot cavities, incorporating photochromic spiropyran (SPI) molecules into a PMMA (polymethyl methacrylate) matrix. These molecules can undergo photoisomerization between the SPI state (transparent in the visible wavelength range) and the colored merocyanine (MC) state, which exhibits an intense absorption band at 560 nm (2.2 eV) (see Figure 3.8a). The switching from the SPI to the MC form (which is accompanied by conformational changes in the molecules) is induced by light irradiation in the UV range, while the reverse transformation can be achieved under visible light illumination. As shown in Figure 3.8b, while the cavity exhibits a single resonance peak centered around 560 nm when the molecules are initially in the SPI state (uncoupled system), a progressive splitting of this cavity mode is observed into two well-defined peaks (corresponding to the two hybrid polaritonic states) when converting the molecules into the MC state under UV light irradiation, indicating the emergence of a light-molecule hybridization. In the MC phase, a Rabi-splitting energy of ~700 meV was reported, corresponding to 1/3 of the molecular excitation energy (2.2 eV), which indicates an ultrastrong coupling regime. Interestingly, as shown in Figure 3.8c, this switching between weak and ultrastrong coupling regimes was found to be reversible, by switching back the molecules into their initial SPI state under visible light irradiation.

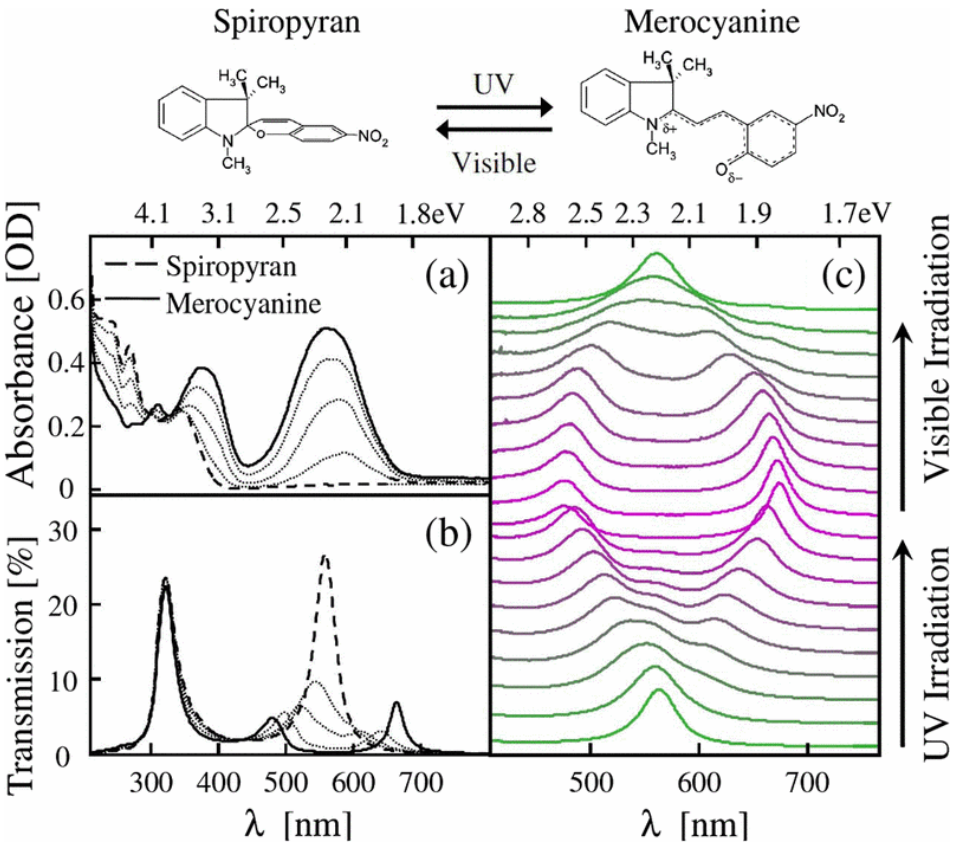

Figure 3.8. (a) Absorbance spectra of a neat film in the SPI (dashed line) and MC (solid line) forms. (b) Cavity normal-incidence transmission with the molecules in the SPI (dashed line) and MC (solid line) forms. The dotted lines in (a) and (b) were taken at a few intermediate states. (c) All-optical reversible switching of the strong light-matter coupling, by converting the molecules into the MC form and back into their initial SPI state, under UV and visible light irradiation, respectively [Schwartz 2011].

Interestingly, in a later study [Hutchison 2012] using the same Fabry-Perot structures incorporating SPI/MC molecules into PMMA, it was also shown that the kinetics of the photoisomerization reaction, from the SPI to the MC state, is significantly modified by the strong-coupling effect. Indeed, following the concentration of the photo-induced MC molecules as a function of irradiation time inside and outside the resonant cavity, it was observed, as shown in Figure 3.9, that the photoisomerization rate is substantially slowed down in the coupled cavity, due to the formation of the hybrid light-matter states. However, no change was observed in the rate of the thermally induced reaction between MC and SPI in the coupled cavity.

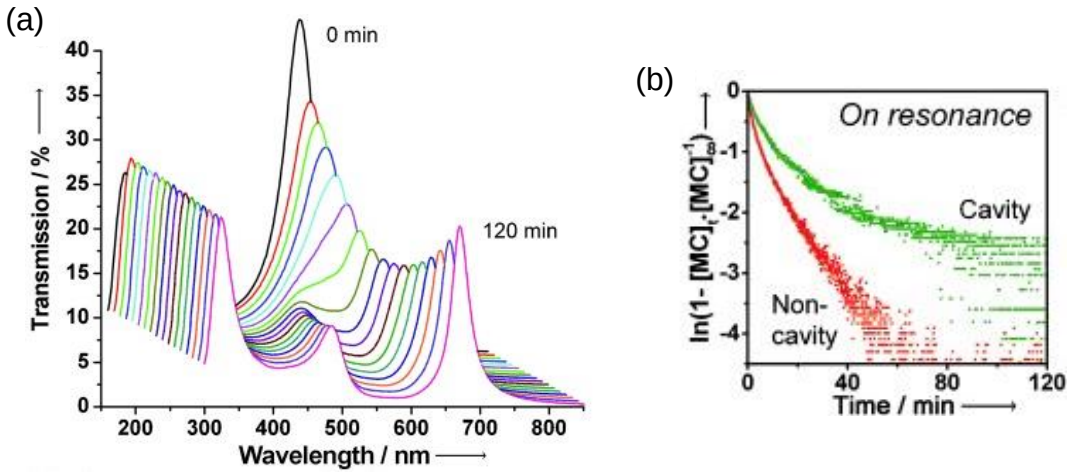

Figure 3.9. (a) Transmission spectra of a Fabry-Perot cavity (incorporating SPI/MC molecules into PMMA), tuned to match the MC absorption at 560 nm, as a function of irradiation time (λ = 330 nm) along the SPI to MC photo-induced reaction. The initial Fabry-Perot mode at *ca.* 560 nm (black curve) splits into two new modes (due to strong light-matter coupling) as the SPI to MC photoreaction proceeds. (b) Kinetics of the growth of MC concentration measured for the bare molecules (outside the cavity, red) and for the coupled system (inside the resonant cavity, green) [Hutchison 2012].

Inspired by these appealing results, in this chapter, we demonstrate that SCO molecules also constitute an attractive class of stimuli-responsive materials that can be strongly coupled to optical cavity modes, to form switchable hybrid light-matter states. Indeed, as mentioned in Chapter 1, SCO complexes commonly exhibit intense charge-transfer (metal-to-ligand or ligand-to-metal) absorption bands (mainly in the UV spectral range), which can possibly lead to the emergence of exceptionally large vacuum Rabi-splitting energies. From this point of view, it appears that there is no fundamental reason why we could not achieve strong coupling of SCO molecules to confined EM fields in optical cavities (even with modest quality factors). However, the regime of strong light-matter interaction involving switchable SCO molecules has never been reported so far. This is one of the main objectives of this thesis work to demonstrate and investigate, for the first time, a regime of strong light-matter coupling between SCO molecules and confined EM modes in photonic nanocavities. In particular, as the spin-state switching is followed by a drastic change of the optical absorption properties of the material, a key objective is to achieve controlled and reversible switching between coupled and

uncoupled regimes upon the SCO, within a single cavity, which could offer an unprecedented means to reach efficient and ultrafast optical modulation in active photonic devices. On the other way around, as the strong-coupling regime is known to involve a tuning of the ground-state energy landscapes of the coupled molecules [Canaguier-Durand 2013; Thomas 2019], we also aim to investigate the effect of the light-matter hybridization on the SCO properties and, more particularly, on the LS/HS phase stability and the spin-transition temperature.

In this chapter, we report on the observation of a light-matter hybridization (in the UV spectral range) between optical modes of purposefully designed nanocavities and electronic excitations of SCO molecules. For this purpose, we have considered two different vacuum-sublimable SCO compounds: the complex [Fe(HB(1,2,4-triazol-1-yl)$_3$)$_2$] **1**, which we have already used and studied in the previous chapter, and the complex [Fe(HB(1,2,3-triazol-1-yl)$_3$)$_2$] **2**, which was recently investigated for its SCO properties in our team [Horniichuk 2022a]. The latter compound, which is an isomer of [Fe(HB(1,2,4-triazol-1-yl)$_3$)$_2$] (they only differ by the position of an exodentate nitrogen atom in the triazolyl ring, see the molecular structure in Figure 3.10a), undergoes a gradual thermal spin transition above room temperature and has the property of being sublimable, i.e., it can be also deposited by vacuum thermal evaporation in the form of high-quality, homogeneous thin films [Horniichuk 2022b]. Indeed, while the thin films of **1** display an abrupt spin transition around 64 °C (spanning over a temperature range of only *ca.* 12 °C), the thin films of **2** comparatively exhibit a very gradual spin conversion, taking place from room temperature to *ca.* 220 °C. In the first part of this study, we selected compound **2** because it exhibits two intense, spectrally well-separated absorption bands in the UV domain (see hereafter), which makes this compound a textbook case to investigate the strong-coupling phenomenon.

3.4 Results

3.4.1 Fabrication and characterization of [Fe(HB(1,2,3-triazol-1-yl)$_3$)$_2$] thin films

The polycrystalline bulk powder of the SCO complex [Fe(HB(1,2,3-triazol-1-yl)$_3$)$_2$] **2**, whose molecular structure is shown in Figure 3.10a, exhibits a gradual spin conversion centered at around 373 K [Horniichuk 2022a]. This complex is sublimable and thin films of **2** were thus fabricated on silicon and fused silica substrates by vacuum thermal evaporation, by heating the bulk powder at 210 °C under a base pressure of 9 × 10^{-7} mbar (evaporation rate is *ca.* 0.04 Å/s).

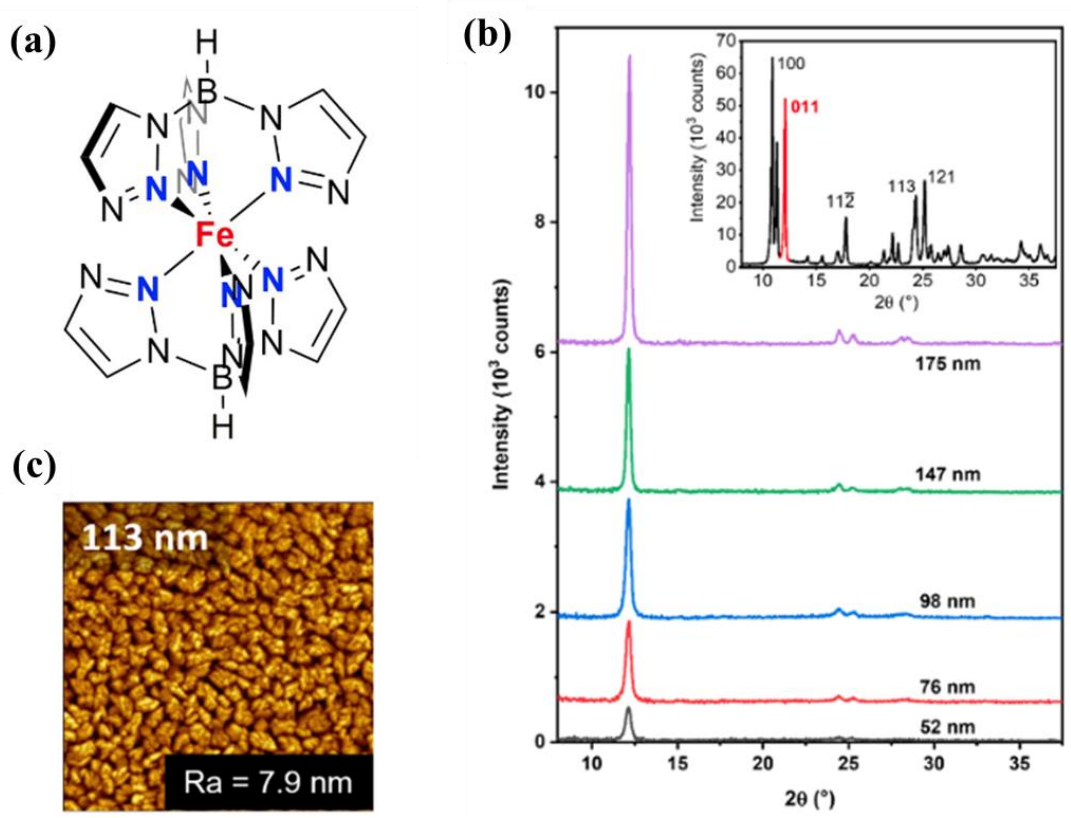

Figure 3.10. (a) Molecular structure of [Fe(HB(1,2,3-triazol-1-yl)$_3$)$_2$]. (b) XRD patterns of nanocrystalline thin films of [Fe(HB(1,2,3-triazol-1-yl)$_3$)$_2$] with various thicknesses, deposited on Si substrates. The inset shows the XRD pattern of the microcrystalline powder. (c) Representative AFM topography image of a 113-nm-thick film of [Fe(HB(1,2,3-triazol-1-yl)$_3$)$_2$] deposited on top of a silicon substrate.

The structural characterization of the thin films was achieved by using grazing-incidence X-ray diffraction (GIXRD). The GIXRD experiments were conducted in ambient conditions by means of a PANalytical X'Pert PRO MPD system using Cu-Ka radiation with a parallel-beam configuration. The XRD patterns exhibit an intense peak at 2θ = 12.15° corresponding to the 011 reflection (Figure 3.10b), which indicates that

the film is crystalline and the crystallites in the films grow preferentially with the [011] direction of the monoclinic unit cell normal to the substrate surface. As shown in Figure 3.10b, this crystallographic orientation was systematically observed in all deposited films, irrespective of the substrate material (silicon or fused silica) and the film thickness.

The surface topography analysis of the films was conducted in amplitude-modulation mode at room temperature using an AFM (SmartSPM, Horiba). As depicted in Figure 3.10c, the nanocrystalline surface morphology of the films is clearly observed in the AFM images and roughness average (Ra) values between 7 and 11 nm are typically extracted.

SCO properties of the thin films of **2** were also investigated by variable-temperature, UV-vis spectrophotometry measurements. At room temperature, the absorbance spectra show two distinct, well-separated absorption bands with maxima at 337 and 274 nm respectively. As the temperature increases, the intensity of these absorption bands decreases (see Figure 3.11a), the HS state being transparent within the 250-400 nm spectral range. As shown in Figure 3.11b, by following the temperature variation of the optical absorbance at the peak wavelength (λ = 337 nm), we find that thin films of **2** exhibit a gradual spin conversion between the LS and HS states, with an equilibrium temperature centered around 100 °C, similar to the one observed in the bulk powder [Horniichuk 2022a].

In summary, the dense, textured, nanocrystalline films of the molecular complex [Fe(HB(1,2,3-triazol-1-yl)$_3$)$_2$] are shown to maintain a gradual spin conversion above room temperature, between *ca.* 273 and 473 K, similar to the SCO observed for the bulk powder of this compound. In terms of optical properties, this compound shows a pronounced, spectrally well isolated, absorption peak around 337 nm, which makes thin films of this compound an extremely promising candidate for the study of the light-matter coupling phenomenon in optical cavities.

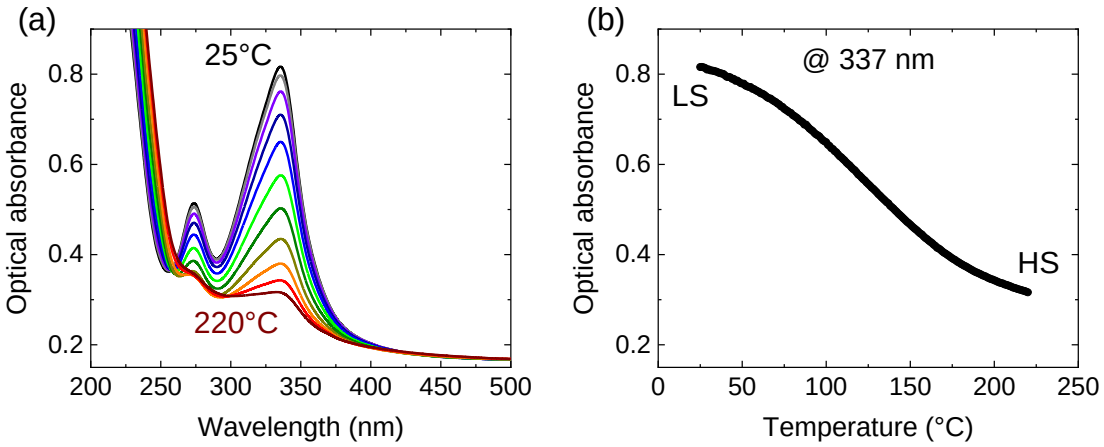

Figure 3.11. SCO properties of the thin films of [Fe(HB(1,2,3-triazol-1-yl)$_3$)$_2$]. (a) Optical absorbance spectra of a 153-nm-thick film on a fused silica substrate, acquired at selected temperatures between 25 and 220 °C. (b) Thermal spin-crossover curve of the same film extracted from the temperature variation of the optical absorbance at the peak wavelength (λ = 337 nm).

3.4.2 Switching between strong and weak coupling in a metal-dielectric bilayer resonator integrating [Fe(HB(1,2,3-triazol-1-yl)$_3$)$_2$]

To demonstrate and achieve for the first time a phenomenon of strong light-matter coupling with SCO molecules, we have fabricated metal-dielectric bilayer resonators (excited using a coupling prism), similar to those studied in Chapter 2, which were purposefully designed such that one of the resonant modes falls in the UV spectral region, near the main absorption band of the compound **2** in the LS state. For this purpose, the Ag layer deposited on the prism was replaced by an aluminum layer (16 nm), which is more suitable for working in the UV range, due to its relatively high value of the plasma frequency with respect to silver (or gold) [Gérard 2014]. The fabricated resonator [prism / Al (16 nm) / **2** (153 nm)] (hereafter denoted 'cavity **2**') was fabricated by successively depositing, by vacuum thermal evaporation, a 16-nm-thick film of aluminum on the base of a right-angle, fused-silica prism, followed by a 153-nm-thick layer of compound **2** (see Figure 3.12). The bulk powder of the SCO complex was heated at *ca.* 240 °C in a quartz crucible at a base pressure of 2 × 10^{-7} mbar. Film thicknesses were monitored in situ using a quartz crystal microbalance and ex situ by spectral reflectance measurements (Filmetrics, F20). As mentioned above, the as-

deposited films of **2** are dense and crystalline with a preferred [011] orientation of the monoclinic crystal lattice normal to the substrate surface [Horniichuk, 2022b].

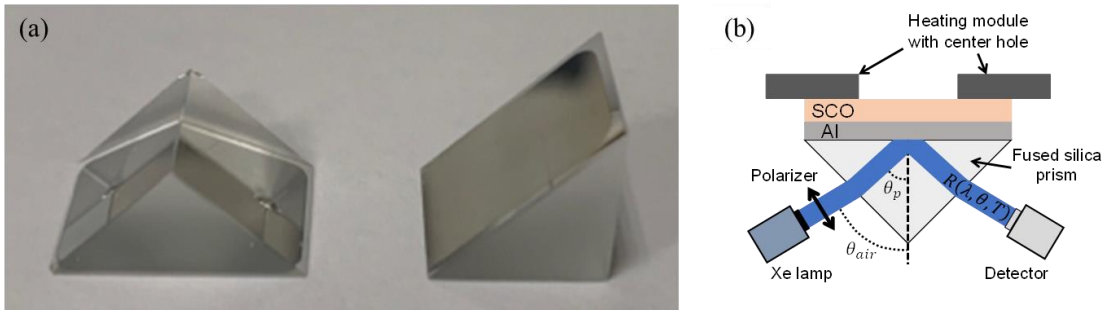

Figure 3.12. (a) Photograph of the right-angle, fused-silica prisms used. (b) Scheme of the fabricated SCO-based resonators formed by the Al (16 nm) / SCO bilayer deposited on a prism, and of the Kretschmann-type experimental setup used for their spectroscopic characterization.

The fabricated SCO-based resonators were investigated by spectroscopic reflectometry measurements, performed in the Kretschmann geometry, in the 200–1000 nm spectral domain and within an angular range of θ_{air} = 42–80° in air, which corresponds to incident angles in the range $\theta_p \approx$ 43–68° within the prism (taking into account the refraction of the light beam at the air/prism interfaces, see Figure 3.12b). The samples were illuminated by a pulsed xenon lamp (Avantes, AvaLight-XE-HP) and the incoming beam was collimated and spatially limited to a diameter of 5 mm with an aperture. A Glan-Laser α-BBO polarizer (adapted to UV light) is inserted in the path of the light source to obtain either s- or p-polarized light and the reflected light was collected by a fiber-coupled spectrometer (Avantes, AvaSpec-ULS2048CL-EVO). The temperature of the sample was controlled in situ by bringing the SCO layer in close contact with a heating stage (Linkam Scientific, PE120 or FTIRSP600), which presents a center hole in order to keep air as the last dielectric layer in the probe region of the cavity (see Figure 3.12b). To obtain absolute values of reflectance, spectra were recorded for both p- and s-polarized incoming light, allowing us to plot the ratio R_p/R_s. As already mentioned in Chapter 2, such bilayer resonators [prism / Al (16 nm) / dielectric (~150 nm)] display different transverse electric (s) and transverse magnetic (p) resonant modes, whose typical angular dispersion curves (calculated by transfer-

matrix methods) [Katsidis 2002], are shown, by way of an example, in Figure 3.13 in the specific case of a non-absorbing dielectric layer.

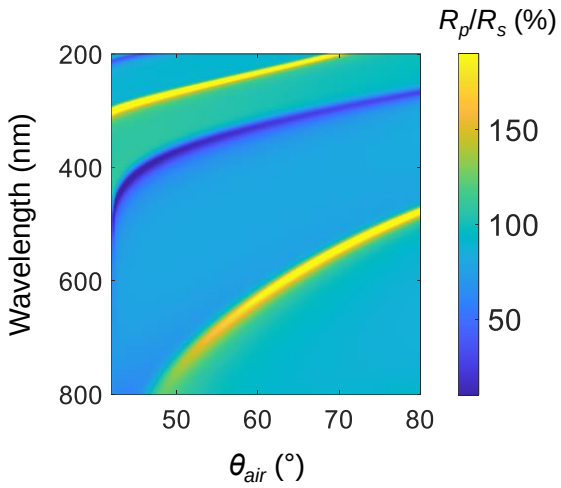

Figure 3.13. Typical angular dispersion curves of a [prism / Al (16 nm) / dielectric (150 nm)] resonator obtained by transfer-matrix simulations, showing the R_p/R_s reflectivity spectra as a function of the incident angle θ_{air}. The dielectric layer is described here as a non-dispersive and non-absorbing medium with a refractive index of 1.7. As shown here, such metal/dielectric bilayer resonators, operating in TIR geometry, exhibit a succession of s-polarized (yellow) and p-polarized (blue) resonance modes.

As a comparison, Figure 3.14b displays the angular dispersion of cavity **2**, measured by acquiring angle-dependent R_p/R_s spectra, at selected temperatures (between 25 and 220 °C). (As an example, the corresponding reflectivity spectra at 25 °C are shown in Figure 3.14a at selected angles of incidence.) The absorption maxima of the SCO complex in the LS state at λ_{1A} = 337 nm (E_{1A} = 3.68 eV) and λ_{1B} = 274 nm (E_{1B} = 4.52 eV) are depicted in Figure 3.14b by horizontal white dashed lines. At room temperature, we clearly observe that the dispersion curve of the s-polarized cavity mode (yellow band) is split into three branches at wavelengths λ_{1A} and λ_{1B}, corresponding to the main absorption bands of the complex. As for the p-polarized cavity mode (blue band), the spectra show, within the probed angular domain, two split peaks around λ_{1A}. Such splitting features in the dispersion are the typical signature of a light-matter hybridization between the molecules and the cavity modes, indicating the formation of hybrid light-exciton polaritonic states. As an example, for the p-polarized mode at room

temperature, the maximum splitting is achieved for an incident angle of 76°, where two spectrally well-separated, symmetrical peaks are observed with an energy difference of ΔE = 864 meV (see Figure 3.14a). This splitting energy is found to be larger than the spectral linewidth of the cavity modes ($\Gamma_{cav} \approx$ 300 meV, Q-factor ~12–16) and of the molecular absorption band ($\Gamma_{1A} \approx$ 420 meV), indicating the emergence of a strong-coupling regime [Törmä 2015; Thomas 2020]. Upon heating the sample above the spin-transition temperature, as the molecules are converted into the optically inactive HS state, we observe a progressive decrease of the splitting energies, until the dispersion curves (for both p- and s-polarized modes) virtually show only a single branch, as expected for a non-absorbing dielectric layer. As a result, at 220 °C, unsplit cavity resonances are observed with Q factors of ~16 and ~12 (values taken at 4.2 eV), for the s-polarized and p-polarized modes, respectively. To model the reflectivity spectra and the angular dispersion of the fabricated resonator, we used the transfer-matrix method [Katsidis 2002], the resonator being modelled as a multilayer structure, which consists of semi-infinite space of fused silica, a layer of aluminum, a dielectric (SCO material) layer and a semi-infinite space of air. The actual angles θ_p at which the incoming beam hits the Al surface were obtained from the experimental incident angles in air θ_{air} by taking into account the refraction of the light beam at the air-prism interface (Snell's law). Calculations were performed including the known optical properties of fused silica [Malitson 1965] and aluminum [McPeak 2015], while the frequency-dependent complex refractive index of **2** was obtained by fitting the measured absorbance spectra with a Drude-Lorentz oscillator model, where the two main absorption peaks were described by Lorentz oscillators at resonance energies E_{1A} and E_{1B} with temperature-dependent oscillator strengths and damping factors. As shown in Figure 3.14c, a good agreement is obtained between the experimental and calculated dispersion, considering thicknesses of 16 and 155 nm for the Al and SCO layers, respectively, which fits well the nominal experimental values.

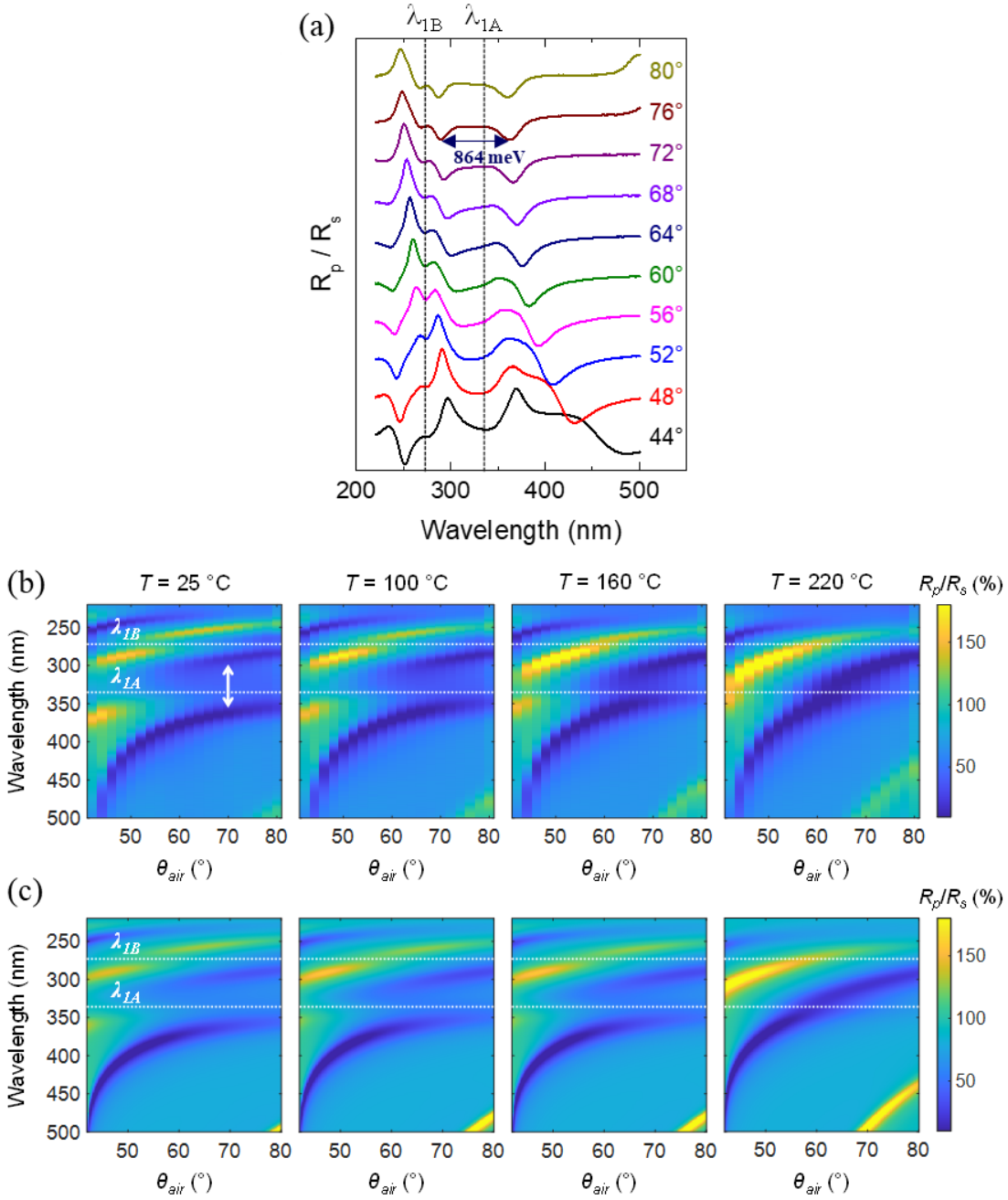

Figure 3.14. (a) Reflectivity R_p/R_s spectra recorded for cavity **2** at room temperature (25 °C) for different angles of incidence θ_{air} from 44 to 80°. The absorption maxima of the SCO complex **2** in the LS state at λ_{1A} = 337 nm and λ_{1B} = 274 nm are depicted by vertical dashed lines. The different spectra have been displaced vertically for clarity but are plotted on the same ordinate scale. (b) Experimental dispersion curves of cavity **2** at four different temperatures, showing R_p/R_s spectra within the angular range θ_{air} = 42–80°. (c) Simulated dispersion of the cavity (at the same temperatures) obtained from transfer-matrix calculations. The absorption maxima of the SCO complex in the LS state at λ_{1A} and λ_{1B} are depicted by horizontal white dashed lines. The vertical double arrow indicates, as an example, the polaritonic splitting for the p-polarized mode.

To better follow the effect of the thermally induced spin transition, Figure 3.15a displays the evolution of the R_p/R_s spectra at a fixed angle of incidence, θ_{air} = 64°, at selected temperatures upon heating and cooling between 25 and 220 °C. Remarkably, we find that the different splittings, initially observed (at room temperature) at λ_{1A} (for the p-polarized mode) and λ_{1B} (for the s-polarized mode), gradually decrease with temperature, until the cavity modes virtually take the form of single peaks at 220 °C. Even more clearly, Figure 3.15b shows the temperature evolution of the p-polarized mode of cavity **3.1** at θ_{air} = 64°, both in heating and cooling modes. We observe that the Rabi splitting associated with the p-polarized mode, which is coupled to the molecular excitation E_{1A} at room temperature, gradually decreases with temperature, until the two branches merge into a single peak at *ca.* 200–220 °C. As shown in Figures 3.15a and 3.15b, the process is found to be fully reversible since the initial Rabi splitting is fully recovered upon cooling back down to room temperature.

To further examine the coupling strength (at constant wave vector) between the optical modes of the cavity and molecular excitons, we have plotted in Figure 3.16 the extrema energies of the reflectivity spectra (extracted from a fitting procedure), for both s- and p-polarized modes, as a function of the in-plane wave vector k_x. The latter is given by $k_x = (2\pi / \lambda)\, n_p(\lambda) \sin(\theta_p)$ where $n_p(\lambda)$ is the refractive index of the fused silica prism and θ_p is the incident angle of the light on the Al layer (within the prism). Clear anticrossing behaviors, characteristic of the strong-coupling regime, are observed at energies corresponding to the maximum absorption of LS molecules. In order to evaluate the coupling strengths, we employed a quantum mechanical coupled-oscillator model to fit the experimental dispersion curves (solid lines in Figure 3.16), the polariton bands of the coupled system being given by the eigenvalues of the following Hamiltonian:

$$\widehat{\mathcal{H}} = \begin{pmatrix} E_{cav}(k_x) & \hbar\Omega_{RA}/2 & \hbar\Omega_{RB}/2 \\ \hbar\Omega_{RA}/2 & E_A & 0 \\ \hbar\Omega_{RB}/2 & 0 & E_B \end{pmatrix} \qquad (16)$$

where $E_{cav}(k_x)$ is the dispersion relation of the bare cavity mode, E_A and E_B are the dispersionless exciton modes of SCO molecules, and $\hbar\Omega_{RA}$ and $\hbar\Omega_{RB}$ are the corresponding Rabi-splitting energies.

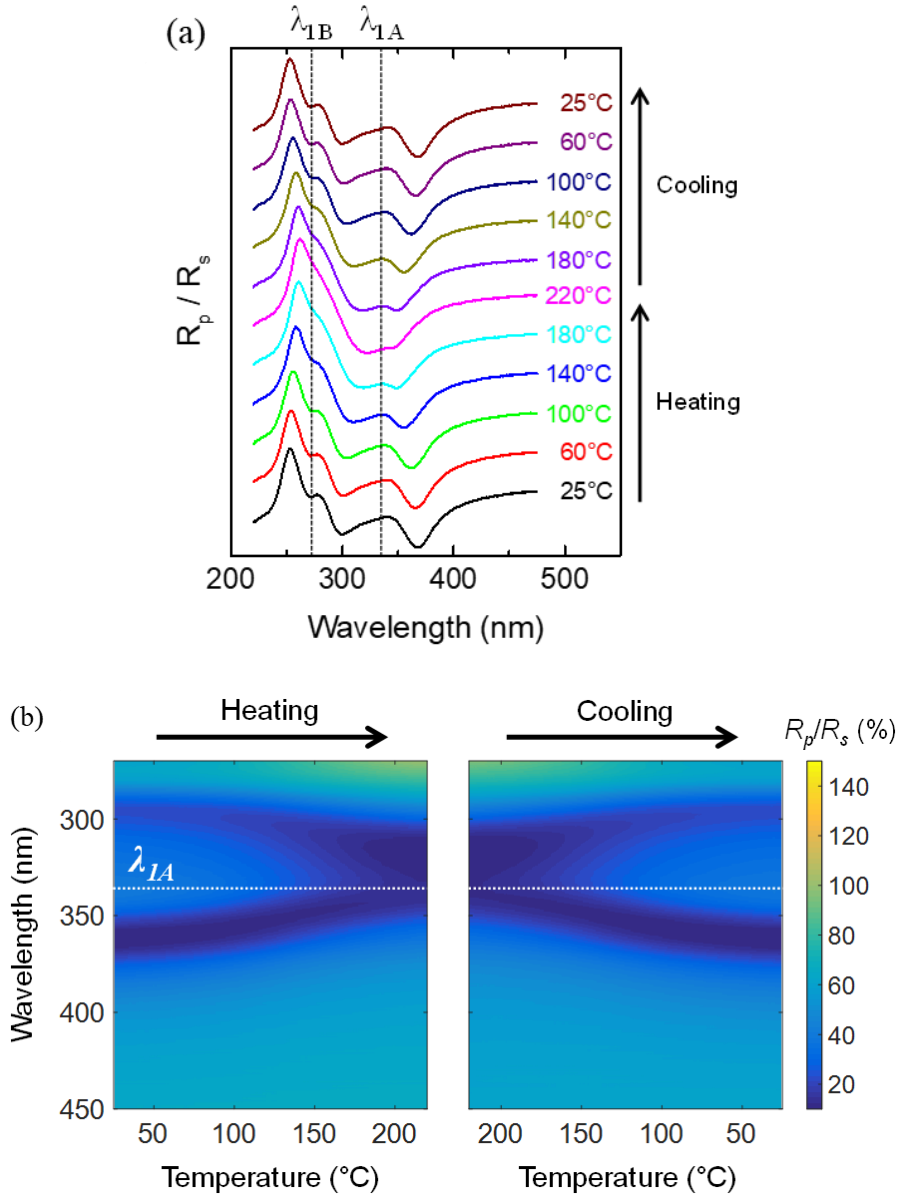

Figure 3.15. (a) Reflectivity R_p/R_s spectra recorded for cavity **2** at a fixed angle of incidence, θ_{air} = 64°, for selected temperatures upon heating and cooling between 25 and 220 °C. The absorption maxima of the SCO complex **2** in the LS state at λ_{1A} = 337 nm and λ_{1B} = 274 nm are depicted by vertical dashed lines. The different spectra have been displaced vertically for clarity, but are plotted on the same ordinate scale. (b) Evolution of the p-polarized resonant mode of cavity **2**, measured at θ_{air} = 64°, as a function of the temperature, upon heating and cooling between 25 and 220 °C. The horizontal dashed line at λ_{1A} = 337 nm indicates the absorption maximum of the SCO complex in the LS state.

Unlike the case of the Fabry-Perot cavities incorporating RhB molecules (described earlier in this chapter), which were involving coupling with a single molecular

excitation, the strong-coupling phenomenon observed here involves two molecular absorption bands (the Hamiltonian takes the form of a 3 × 3 matrix), so that the energies of the polaritonic bands cannot be calculated analytically, but by numerically diagonalizing the Hamiltonian given by Eq. (16). At room temperature (25 °C), for the s-polarized mode, the numerical fitting reveals that the resonances occur for k_x = 18.2 and 28.1 μm^{-1} (when the uncoupled cavity mode has the same energy as the molecular excitations 1A and 1B), with corresponding Rabi-splitting energies of 546 and 259 meV, respectively. As for the p-polarized mode, the coupling between the cavity and molecules at E_{1A} is characterized by a Rabi-splitting energy of 535 meV. These light-matter interaction energy values, which correspond (in the case of the molecular excitation 1A) to 15 % of the bare energy of the uncoupled systems, $\eta = \hbar\Omega_R / E_{1A} \approx 0.15$, signify that our SCO-based resonator is likely into the so-called ultrastrong-coupling (USC) regime [Frisk Kockum 2019; Forn-Díaz 2019] the latter being generally considered as established when the normalized coupling factor is $\eta > 0.1$.

This USC regime is currently the subject of intense investigations due to the potential emergence of intriguing physical effects and applications, including fast and protected quantum information processing, nonlinear optics, modified chemical reactivity, or the enhancement of various quantum phenomena [Frisk Kockum 2019]. Especially, this regime is particularly interesting since it implies that not only the excited states of the coupled system are disturbed but also the ground state [Ciuti 2005; Forn-Díaz 2010], which could have an effect on the thermodynamics of molecules and, therefore, on their switching properties [Wang 2014; Canaguier-Durand 2013; Climent 2019]. As shown in Figure 3.16, a clear diminution of the coupling strength is observed upon heating, and, at 220 °C (almost fully in the HS state), the maximum splitting energy is found to be 172 meV (for the molecular excitation 1A), which indicates that the system finally lies in the weak-coupling regime.

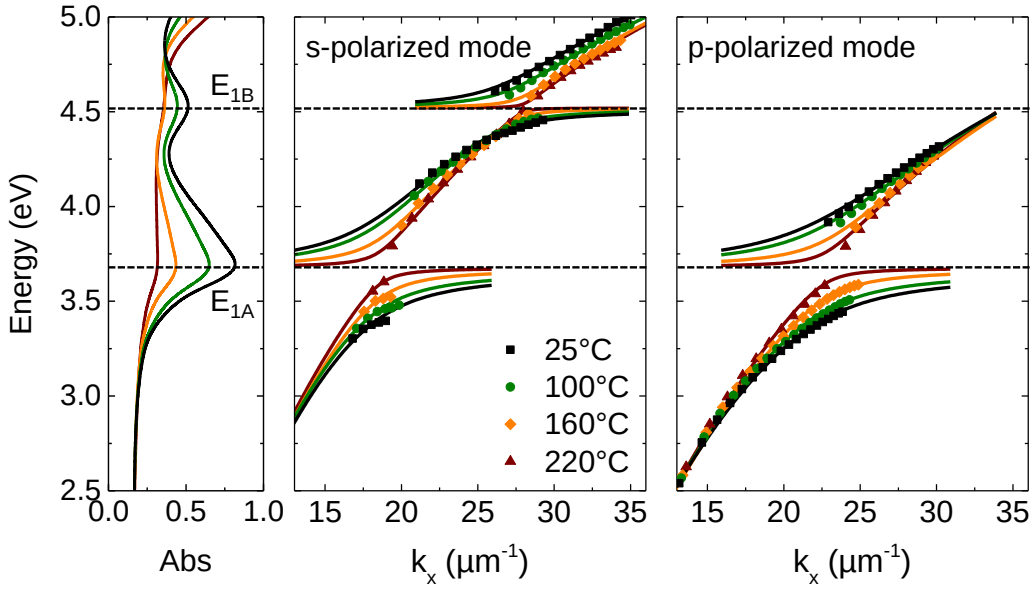

Figure 3.16. Measured dispersion (energy vs. in-plane wave vector) curves of cavity **2**, for both s- and p-polarized modes, at selected temperatures between 25 and 220 °C. The horizontal dashed lines at 3.68 and 4.52 eV indicate the dispersionless molecular excitation energies. The fits (solid lines) of the dispersion curves of the coupled system are obtained using a three-coupled oscillator model (Eq. 16).

As depicted in Figure 3.17, the Rabi-splitting energy extracted from the fitting procedure is found to be closely proportional to the square root of the SCO film absorbance (especially for the molecular excitation 1A), which is an expected feature since the Rabi splitting is known to scale with the square root of the concentration of coupled molecules (here LS molecules) within the cavity mode volume [Hertzog 2019]. Interestingly, the coupling strength of the cavity with the molecular excitation 1A is found to be identical (within the error bars) for both s- and p-polarized modes, meaning that the electric field amplitude distribution, averaged over the total thickness of the SCO layer, is similar for both s- and p-polarized cavity modes. However, noticeable differences are observed when comparing the coupling strength of the s-polarized cavity mode with the two molecular excitations 1A and 1B. Such differences presumably come from a greater mismatch between cavity and exciton linewidths in the case of the molecular excitation 1B, which has the effect, as predicted by Eq. (12), of reducing the Rabi-splitting energy and deviating the evolution of $\hbar\Omega_R$ with respect to $Abs^{1/2}$ from the linear behavior [Herrera 2020].

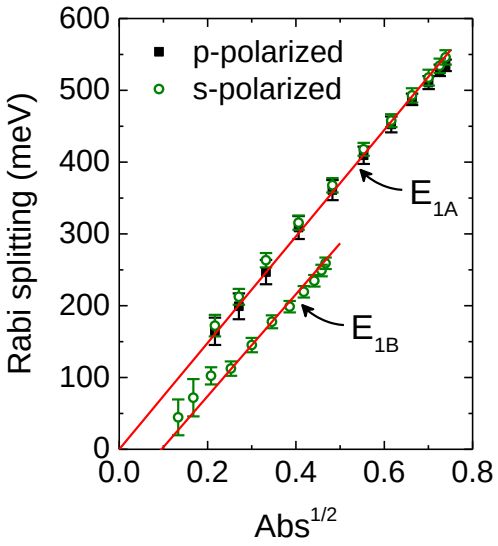

Figure 3.17. Evolution of the Rabi-splitting energies, extracted from the fitting procedure shown in Figure 3.16 (solid lines), as a function of the square root of the SCO film absorbance. Error bars represent one standard deviation of the fitted Rabi-splitting values.

3.4.3 Switching between strong and weak coupling in a metal-dielectric bilayer resonator integrating [Fe(HB(1,2,4-triazol-1-yl)$_3$)$_2$]

In a similar manner, we have then fabricated a second Al/SCO bilayer resonator incorporating this time a 138-nm-thick film of the complex [Fe(HB(1,2,4-triazol-1-yl)$_3$)$_2$] **1**. This newly designed resonator [prism / Al (16 nm) / **1** (138 nm)] (hereafter denoted 'cavity **1**') was fabricated using the same methods as cavity **2**. As mentioned in Chapter 2, it is noteworthy that the as-deposited film of **1** was recrystallized by a solvent-vapor annealing treatment, resulting in oriented, nanocrystalline thin films [Shalabaeva 2017a].

As already specified in Chapter 2, thin films of **1** exhibit intense, SCO-dependent absorption bands in the UV spectral range (see Figure 3.18). More specifically, at room temperature (in the LS state), this compound exhibits three main bands around 317, 305 and 272 nm. As shown in Figure 3.18, these UV absorption bands are completely bleached upon heating the film above the spin-transition temperature ($T_{SCO} \approx 65$ °C), the HS state being transparent within the 250–400 nm spectral region.

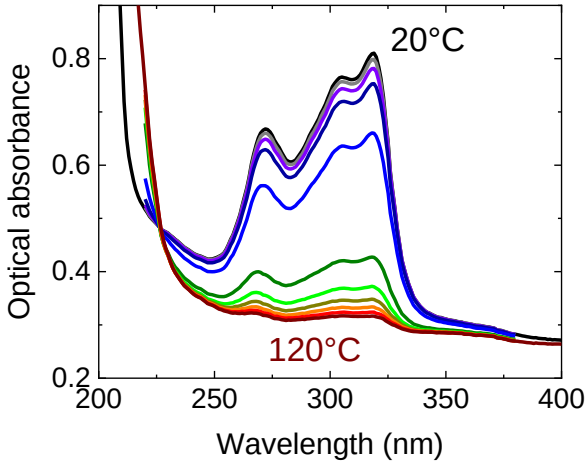

Figure 3.18. UV optical absorbance spectra of a 138-nm-thick film of complex **1** deposited on a fused-silica substrate, acquired a selected temperatures (every 10 °C between 20 and 120 °C).

As for cavity **2**, the spectroscopic characteristics of cavity **1** were investigated by reflectometry measurements. In the angular range studied, the experimental dispersion curves reveal that only a p-polarized mode of the resonator enters into resonance with the molecular excitations. As displayed in Figure 3.19b (see also the corresponding spectra in Figure 3.19a), at room temperature, this mode is split into three branches at wavelengths $\lambda_{2A} \approx 315$ nm ($E_{2A} \approx 3.93$ eV) and $\lambda_{2B} = 272$ nm ($E_{2B} = 4.55$ eV), corresponding to the two main absorption bands of the complex in the LS state (the effects of the two molecular excitations at 305 and 317 nm are experimentally indistinguishable due to their spectral proximity). When the sample is heated, a sudden decrease of the splitting energies is observed between 60 and 80 °C, corresponding to the spin-state switching of complex [Fe(HB(1,2,4-triazol-1-yl)$_3$)$_2$] from the LS to the HS state. As displayed in Figure 3.19c, a good agreement is found between the experimental and simulated dispersion curves obtained by transfer-matrix calculations, for the different temperatures. In these simulations, the complex refractive index of the compound **1** was obtained using a Drude-Lorentz oscillator model based on measured UV-vis absorbance spectra (Figure 3.18) and temperature-dependent ellipsometric data (Figure 2.11).

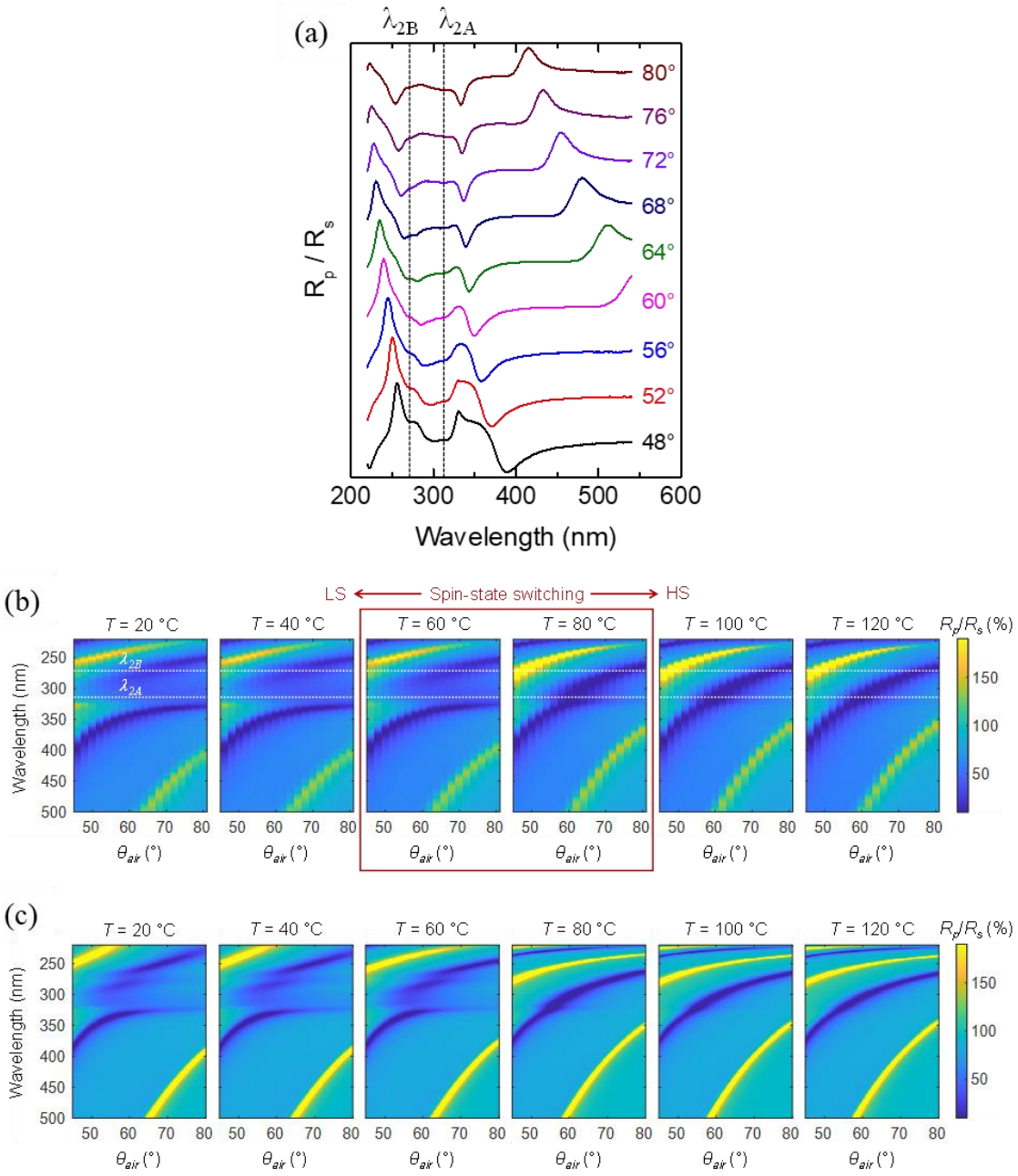

Figure 3.19. (a) Reflectivity R_p/R_s spectra recorded for cavity **1** at room temperature (20 °C) for different angles of incidence θ_{air} from 48 to 80°. The vertical dashed lines depict the two main absorption bands of the complex in the LS state at λ_{2A} = 315 nm and λ_{2B} = 272 nm. The different spectra have been displaced vertically for clarity but are plotted on the same ordinate scale. (b) Experimental dispersion curves of cavity **1** at six different temperatures, showing R_p/R_s spectra within the angular range θ_{air} = 46–80°. The absorption maxima of the SCO complex in the LS state at λ_{2A} and λ_{2B} are depicted by horizontal white dashed lines. (c) Simulated dispersion curves of the resonator at the same temperatures, obtained by transfer-matrix calculations.

The effect of the spin transition is shown in more detail in Figure 3.20a, which displays the evolution of R_p/R_s spectra at a fixed angle of incidence, θ_{air} = 74°, at selected temperatures upon heating and cooling between 20 and 120 °C. Clearly, we observe that the p-polarized mode of the resonator, which is initially split into peaks at room temperature (LS state), takes the form of a single peak above the spin-transition temperature (T_{SCO} = 65 °C), as it is expected for such a bilayer resonator integrating a non-absorbing dielectric layer. This effect is even more clearly displayed in Figure 3.20b, which shows the temperature evolution of the p- and s-polarized modes at θ_{air} = 74°, both in heating and cooling modes. On one hand, an abrupt decrease of the Rabi splitting is evidenced for the p-polarized mode around T_{SCO} = 65 °C, above which temperature only a single branch is observed. On the other hand, in the visible spectral range, the uncoupled s-polarized mode (at $\lambda \approx$ 445 nm) simultaneously exhibits a marked 30-nm blue shift due to the SCO phenomenon. This shift value (30 nm) is similar to that observed for the resonator Ag/[Fe(HB(1,2,4-triazol-1-yl)$_3$)$_2$], reported in the previous Chapter. As already discussed in Chapter 2, this blue shift is attributed to the substantial decrease of the refractive index of the SCO material (Δn_{SCO} = 0.05 in the visible domain) when switching from the LS to the HS state. Thus, in addition to the coupling/uncoupling process with molecular excitons, the cavity modes are also impacted by the refractive index change of the SCO layer upon the spin transition, providing a dual mode of tuning based on either the absorption or the refractive index change. In addition, as shown in Figure 3.20, all these SCO-induced processes are fully reversible upon cooling back down to room temperature.

Interestingly, the dispersion (energy vs. in-plane wave vector) curves of cavity **1**, shown in Figure 3.21, reveal Rabi-splitting energies up to 548 and 192 meV at room temperature (full LS state), at the resonance with the two main molecular absorption bands 2A and 2B, respectively. In this case, this maximum coupling energy value corresponds to 14 % of the molecular excitation energy, which indicates, as for cavity **2**, an ultrastrong coupling regime. Above 100 °C, no splitting is detectable as the SCO film is fully in the HS state.

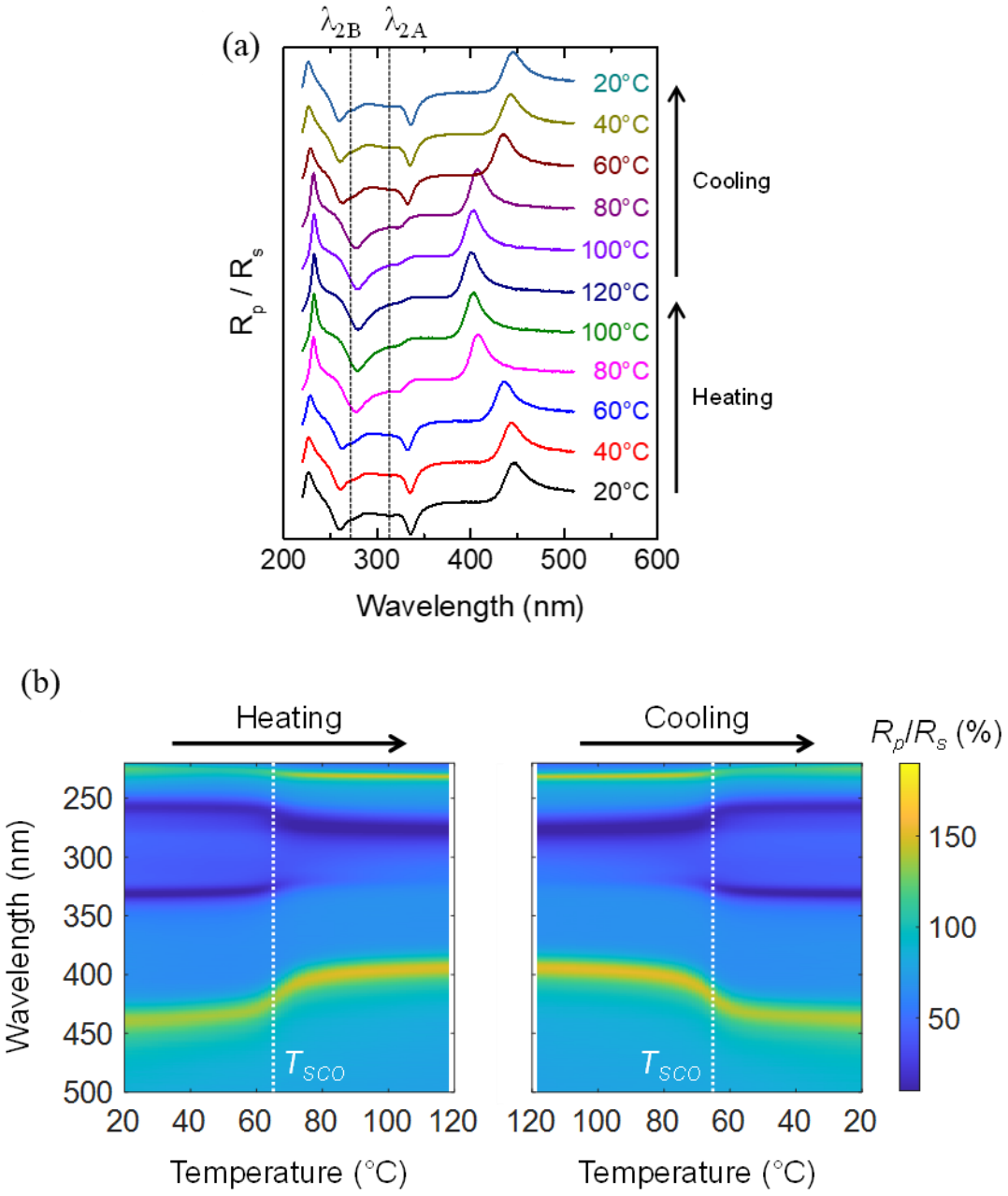

Figure 3.20. (a) Reflectivity R_p/R_s spectra recorded for cavity **1** at a fixed angle of incidence, θ_{air} = 74°, for selected temperatures upon heating and cooling between 20 and 120 °C. The vertical dashed lines depict the two main absorption maxima of the SCO complex in the LS state at λ_{2A} = 315 nm and λ_{2B} = 272 nm. The different spectra have been displaced vertically for clarity, but are plotted on the same ordinate scale. (b) Evolution of the p- and s-polarized modes of cavity **1**, measured at θ_{air} = 74°, as a function of the temperature, upon heating and cooling. The white dashed lines indicate the spin-transition temperature T_{SCO} = 65 °C.

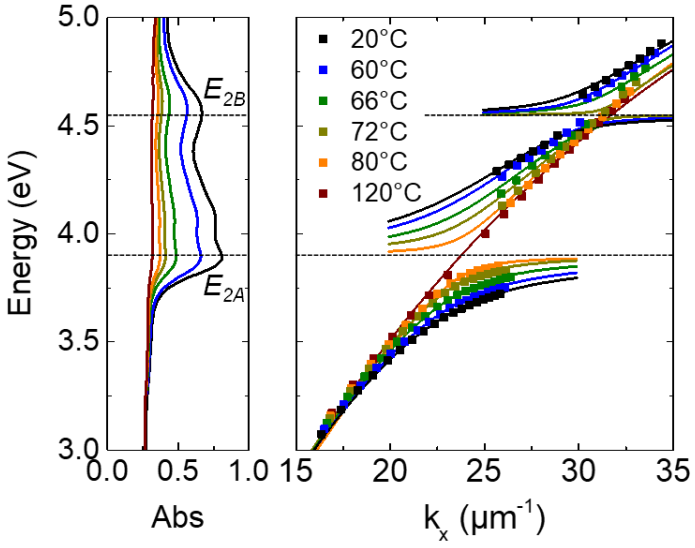

Figure 3.21. Dispersion curves (energy vs. in-plane wave vector) of cavity **1** (p-polarized mode) at selected temperatures between 20 and 120 °C. The horizontal dashed lines at E_{2A} = 3.93 eV and E_{2B} = 4.55 eV indicate the dispersionless molecular excitation energies. The fits (solid lines) of the dispersion curves of the coupled system are obtained using a three-coupled oscillator model (Eq. 16).

Finally, another important result in Figure 3.20 concerns the fact that both the abruptness and the temperature of the spin transition (*ca.* 65 °C), in the film coupled to the cavity, remain virtually unaltered, within our experimental uncertainty, in comparison with films deposited on bare substrates [Shalabaeva 2017b]. (Our experimental uncertainty is quite large (of about 5 °C), due to possible thermal lag arising from the large thermal inertia of the fused-silica prism.) Put differently, neither the energy gap between the HS and LS states, nor the cooperativity of the spin transition appear to be affected by the (ultra)strong light-matter coupling in cavity **1**. In the past decade, the effect of strong coupling on the ground-state properties and reactivity of molecules has attracted much attention [Thomas 2016; Thomas 2020; Wang 2014; Canaguier-Durand 2013; Thomas 2019; Simpkins 2021], but the origin of the exciting experimental findings remains largely open to discussion. The generally accepted picture is that for a macroscopic system with $N >> 1$ dipoles, the resonant-coupling-induced change to the free energy becomes negligible [Ćwik 2016; Martínez-Martínez 2018; Galego 2019; Pilar 2020; Li 2020] and thus other, still debated, mechanisms must

prevail. Notably, theoretical calculations indicated that strong coupling between the dipole moment (μ) of SCO molecules and the confined EM field in plasmonic nanocavities could give rise to a substantial shift of the spin-state equilibrium temperature – provided that μ is aligned with the polarization of the cavity mode and displays a sizeable change upon the spin transition [Climent 2019]. These conditions are, effectively, not met in our experiments due to the high symmetry of the studied molecules, which results in extremely small permanent dipole moments (ca. 0.001 and 0.0002 Debye in the HS and LS states, respectively, for compound **1**) [Dixon 2020]. Further work should therefore focus on using molecules exhibiting large dipole moment differences between the two spin states and photonic resonators with more tightly confined EM fields.

3.4.4 Comparison of the two studied resonators

As a summary, Figure 3.22 displays the temperature evolution of the Rabi-splitting energies measured in the two studied resonators, demonstrating the possibility of a thermal tunability of the light-molecule coupling strength, between a strong and weak coupling regime. Interestingly, due to the comparable absorption properties in the two studied SCO complexes at room temperature (in the LS state), the two fabricated resonators exhibit an ultrastrong coupling regime with similar Rabi-splitting energies of *ca.* 550 meV. In addition, we show that the coupling regime change follows the characteristics of the thermal spin transition. Indeed, the two resonators studied here represent two antagonist cases: while cavity **2**, incorporating the complex [Fe(HB(1,2,3-triazol-1-yl)$_3$)$_2$], exhibits a very gradual tuning of the hybridization strength on a wide temperature range (then allowing a tight external control of the coupling strength), cavity **1** (incorporating [Fe(HB(1,2,4-triazol-1-yl)$_3$)$_2$]) shows a relatively abrupt ON/OFF switching of the coupling regime. It is worth mentioning that in both cases the switching between the ultrastrong and weak coupling regimes can be achieved reversibly and in a fully reproducible manner.

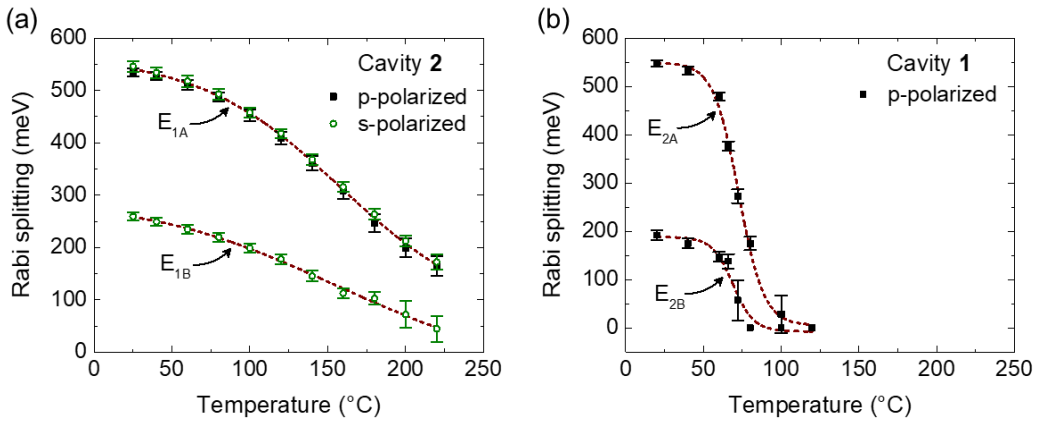

Figure 3.22. Tunability of the light-matter coupling strength with temperature in the two studied resonators. Temperature evolution of the Rabi-splitting energies measured in (a) cavity **2** and (b) cavity **1**, incorporating a SCO thin film of complexes $[Fe(HB(1,2,3\text{-triazol-1-yl})_3)_2]$ and $[Fe(HB(1,2,4\text{-triazol-1-yl})_3)_2]$, respectively. Error bars represent one standard deviation of the fitted Rabi-splitting values. The dashed lines are guides for the eye.

3.5 Conclusions and perspectives

In conclusion, we have demonstrated a switchable ultrastrong light-matter coupling between optical modes of metal/dielectric bilayer resonators and SCO molecules. In their LS state, the intense absorption bands of SCO molecules in the UV spectral domain can be coupled to cavity photon modes resulting in Rabi-splitting energies up to 550 meV, i.e. ~15 % of the molecular excitation energy. By converting thermally the molecules into their non-absorbing HS state, we demonstrate the possibility of finely tuning the hybridization strength, ultimately allowing a reversible and reproducible switching between ultrastrong and weak coupling regimes in a single photonic system. Using vacuum-deposited thin films of two SCO compounds with different spin-transition properties, a gradual and abrupt switching of the coupling regime could be achieved with temperature.

Through this work, we show that SCO compounds constitute a class of switchable molecular materials of great interest in the field of switchable polaritonic chemistry as well as in the domain of active photonics. In this perspective, an appealing feature of SCO compounds is the possibility to use light irradiation to address the molecular spin

state. As the photoswitching process typically occurs on the sub-picosecond timescale [Ridier 2019], this suggests interesting prospects for ultrafast all-optical modulation of the strong light-matter coupling in micro-nano-cavities, governed by short laser excitations. In addition, the vast library of well-characterized SCO materials, exhibiting a variety of spin-transition properties (gradual, abrupt, with or without hysteretic behaviors), provides an excellent playground for the investigation of the effects of strong coupling, and potentially affords for appealing switchable polaritonic systems.

On the other way around, this study also opens up the possibility to explore the physical and chemical properties of switchable SCO molecules under strong coupling. In particular, an interesting aspect would be to probe the effect of this coupling on the photophysical properties of molecules (e.g. by ultrafast optical spectroscopic methods), the present results paving the way, for instance, to appealing possibilities for investigating the dynamics of the polaritonic states as a function of the coupling strength in a single cavity. Another appealing perspective is to investigate the possible effects of the light-matter hybridization on the molecular ground state and, therefore, on the LS/HS phase equilibrium of molecules coupled to the cavity. Indeed, whereas the strong coupling primarily affects the excited states, we shall remark that it also gives rise to a shift of the ground-state energy (ΔG^0 in Figure 3.1a). Although the magnitude of this effect is still controversial, especially in the case of a large ensemble of molecules [Martínez-Martínez 2018], several experimental studies report on sizeable modification of the free energy landscape of strongly coupled molecular systems [Canaguier-Durand 2013; Wang 2014]. These studies unveil a Gibbs free energy difference (ΔG^0) between ground states of the uncoupled and coupled molecules of the order of tens of meV, which is of the same order of magnitude as the energy gap between molecular LS and HS states in some SCO complexes. For example, Ebbesen and co-workers have reported the successful tuning of the first-order structural phase transition of a perovskite film, strongly coupled to the vacuum field inside a Fabry-Perot microcavity [Wang 2014]. However, it is worth to mention that the mechanisms underlying these observations are still unclear and are likely not restricted to polaritonic

effects, but can also involve other phenomena such as Casimir-Polders interactions [Galego 2019]. If observed, this effect would open up an exciting scope to adjust the spin-transition temperature of compounds by means of nanotechnology (instead of synthetic chemistry).

For now, within our experimental conditions, we have not observed any noticeable effect of the USC regime on the SCO behavior. Yet, the extreme robustness and reproducibility of the SCO phenomenon in our preferentially-oriented, thin films (>10 million thermal switching events with <1 °C drift in films of [Fe(HB(1,2,4-triazol-1-yl)$_3$)$_2$]) [Ridier 2020] will provide an appealing scope to analyze even minute effects of the USC regime on the ground state of the system in future works.

In addition, based on the present results, an interesting perspective will be to assess the dependence of light-matter coupling strength on the design of the cavity, in order to determine the most favorable conditions for obtaining the highest Rabi-splitting energies. To this aim, Al-mirror-based Fabry-Pérot cavities, which offer both ease of fabrication and of characterization, constitute appealing systems for analyzing SCO-based strong-coupling phenomena in the near future. The obtained Rabi-splitting values can be compared with those obtained in the Al/SCO bilayer resonators.

GENERAL CONCLUSIONS AND PERSPECTIVES

GENERAL CONCLUSIONS AND PERSPECTIVES

The 3d orbital electrons of spin crossover materials rearrange under external stimuli (such as temperature, pressure, light radiation, etc.), resulting in a change in the length of the coordination bond between the metal ion and the ligand, which eventually leads to a change in the molecular volume. These electronic and structural changes give rise to sizeable changes in the optical properties of the material through the entire UV-VIS-NIR spectral range. Based on this asset of SCO compounds, this thesis work focuses on their application in the fields of optics and photonics with the central aim of achieving reconfigurable, active and/or adaptive optical devices. On one hand, thermally-tunable optical devices were constructed, based on the reversible switching of the refractive index between the high spin and low spin states of SCO materials. Then, we explored strong coupling of SCO molecules to electromagnetic modes within optical cavities and achieved a fine control of the light-matter hybridization strength through the spin state switching of molecules, which entails the change of extinction coefficient.

As for the first axis of this work, the low extinction coefficient in the visible range and the large refractive index change at the spin transition in some SCO materials provides potential advantages for photonics applications in comparison with other phase change materials. Indeed, the relevant figure of merit ($\frac{\Delta n}{k_{min}}$) for SCO compounds is typically ≥ 100 in the VIS-NIR range, whereas for other PCMs typically one observes FOM values of ≤ 1. To examine more closely this potential benefit of SCO materials, we constructed simple, multilayer optical devices based on SCO materials. We selected the SCO complex **1** [Fe(HB(1,2,4-triazol-1-yl)$_3$)$_2$] displaying a robust and abrupt spin transition above room temperature. The first device, with the structure Ag (40 nm)/**1** (142 nm)/Ag (40 nm), was based on previous works in the team. Its transmittance spectra revealed a substantial resonance wavelength shift of 6 nm due to the spin state switching, but the associated optical modulation was rather modest (3 %). For this reason, our attention was focused on the bilayer resonator, Ag (35 nm)/**1** (162 nm), which was investigated

using a total internal reflectance method. Compared with the Ag (40 nm)/**1** (142 nm)/Ag (40 nm) Fabry–Pérot cavity, the Ag (35 nm)/**1** (162 nm) resonator is not only easier to fabricate, but also provides a higher sensitivity to refractive index change, showing a large spectral shift of the resonant mode ($\Delta\lambda_{SCO}$ = 30 nm) upon SCO, and, ultimately, a higher optical modulation (70 %). Interestingly, we demonstrate that the large thermal tunability of the device also gives rise to a photothermal nonlinearity, which can be leveraged for achieving optical limiting applications, i.e. an adaptive device. Overall, we demonstrate thus that SCO compounds constitute a promising class of phase-change materials exhibiting broadband optical transparency in the visible range, which is a highly demanded asset for the development of low-loss photonic applications. In this context, the prospect is to further explore the applicability of our materials in real world devices, such as photonic integrated circuits (PICs) and spatial light modulators (SLMs). Notably, for PIC applications, CMOS-compatible silicon nitride waveguide technology appears promising as it opens prospects for transparency down to the visible spectral region [Roeloffzen 2013]. However, device actuation is limited to thermal stimulus. It appears thus particularly interesting to integrate SCO materials with silicon nitride platforms, which can allow combining the advantages of the latter with fast and efficient optical modulation.

Regarding the second axis of our work, taking advantage of the absorbance change accompanying the SCO phenomenon, we explored the strong coupling of SCO molecules with electromagnetic modes in optical cavities consisting of Al/SCO bilayers. The formation of hybrid light-matter states, through the resonant interaction of confined electromagnetic fields with matter excitations, has emerged as a fascinating tool for controlling quantum-mechanical states and then manipulating matter functionalities and chemical reactivity landscape. Here, we reported on the first observation of switchable strong light-matter coupling involving bistable spin-crossover molecules of [Fe(HB(1,2,4-triazol-1-yl)$_3$)$_2$] and [Fe(HB(1,2,3-triazol-1-yl)$_3$)$_2$]. Spectroscopic measurements, supported by transfer-matrix simulations, revealed Rabi-splitting values up to 550 meV, which, at 15 % of the molecular excitation energy, enters the regime of

ultrastrong coupling. We find that the thermally induced switching of molecules between their low-spin and high-spin states allows a fine control of the light-matter hybridization strength, offering the appealing possibility of a reversible switching between the ultrastrong and weak coupling regimes within the cavity. On the other hand, the energy gap between the two spin states was found to remain unaltered by the coupling. Through this work, we show that spin-crossover molecular compounds constitute a promising class of active nanomaterials in the burgeoning context of tunable polaritonic devices and polaritonic chemistry. As for the perspectives of the light-matter coupling, we seek to fine-tune the spin crossover properties by coupling one of the two molecular spin states to a cavity mode. This property could be the 'Holy Grail' in the spin crossover field allowing, for instance, custom-designed photophysical properties (LIESST effect). In a first time, we will continue to study the strong coupling of SCO molecules to electromagnetic modes in Fabry–Pérot cavities. Notably, SCO complexes with different spin transition types (such as gradual spin transition, abrupt spin transition and spin transition with hysteresis etc.) and temperatures (below and above room temperature) will embedded in Al/SCO/Al structures and their SCO properties will be examined using static and dynamic light excitations.

References

Abdul-Kader K., Lopes M., Bartual-Murgui C., et al., Synergistic switching of plasmonic resonances and molecular spin states, Nanoscale 5 (2013) 5288.

Akou A., Gural'skiy I. A., Salmon L., et al., Soft lithographic patterning of spin crossover complexes. Part 2: stimuli-responsive diffraction grating properties, J. Mater. Chem. 22 (2012) 3752.

Akou A, Bartual-Murgui C, Abdul-Kader K, et al., Photonic gratings of the metal–organic framework {Fe(bpac)[Pt(CN)$_4$]} with synergetic spin transition and host–guest properties, Dalton Trans. 42 (2013) 16021.

Arnaud C, Forestier T, Daro N, et al., Observation of an asymmetry in the thermal hysteresis loop at the scale of a single spin-crossover particle, Chem. Phys. Lett. 470 (2009) 131.

Asamoah B. O., Mohamed S., Datta S., et al., Optically induced crossover from weak to strong coupling regime between surface plasmon polaritons and photochromic molecules, Opt. Express 28 (2020) 26509.

Ashida Y., İmamoğlu A., Faist J., et al., Quantum electrodynamic control of matter: Cavity-enhanced ferroelectric phase transition, Phys. Rev. X 10 (2020) 041027.

Bartual-Murgui C, Akou A, Thibault C, et al., Spin-crossover metal–organic frameworks: promising materials for designing gas sensors, J. Mater. Chem. C 3 (2015) 1277.

Baudrion A. L., Perron A., Veltri A., et al., Reversible strong coupling in silver nanoparticle arrays using photochromic molecules, Nano Lett. 13 (2013) 282.

Beeckman J., Neyts K., Vanbrabant P. J. M., Liquid-crystal photonic applications, Opt. Eng. 50 (2011) 081202.

Benz A., Montaño I., Klem J. F., et al., Tunable metamaterials based on voltage controlled strong coupling, Appl. Phys. Lett. 103 (2013) 263116.

Bertoni, R., Lorenc, M., Cailleau, et al. Elastically driven cooperative response of a molecular material impacted by a laser pulse. Nat. Mater. 15 (2016) 606.

Bitarafan M. H., DeCorby R. G., On-chip high-finesse Fabry-Perot microcavities for optical sensing and quantum information, Sensors 17 (2017) 1748.

Boillot M.-L., Sour A., Delhaes P., et al., A photomagnetic effect for controlling spin states of Iron(II) complexes in molecular materials, Coord. Chem. Rev. 190-192 (1999) 47.

Boillot M.-L., Zarembowitch J., Sour A., Ligand-driven light-induced spin change (LD-LISC): a promising photomagnetic effect, Top. Curr. Chem. 234 (2004) 261.

Bousseksou A., Nasser J., Linares J., Ising-like model for the two-step spin-crossover, J. Phys. I France, 2 (1992) 1381.

Bousseksou, A., McGarvey, J. J., Varret, F. et al., Raman spectroscopy of the high-and low-spin states of the spin crossover complex Fe (phen) 2 (NCS) 2: an initial approach to estimation of vibrational contributions to the associated entropy change. Chem. Phys. Lett. 318 (2000) 409.

Bousseksou, A., Boukheddaden, K., Goiran, et al., Dynamic response of the spin-crossover solid C o (H 2 (fsa) 2 e n)(py) 2 to a pulsed magnetic field. Phys. Rev. B 65 (2002) 172412.

Bousseksou A., Molnár G., Salmon L., et al., Molecular spin crossover phenomenon: recent achievements and prospects, Chem. Soc. Rev. 40 (2011) 3313.

Bousseksou A. (Ed.), Spin crossover phenomenon, C. R. Chimie, Vol. 21, issue 12, 2018.

Brady C., McGarvey J. J., McCusker J. K., et al., Time-resolved relaxation studies of spin crossover systems in solution, Top. Curr. Chem. 235 (2004) 1.

Briggs R. M., Pryce I. M., Atwater H. A., Compact silicon photonic waveguide modulator based on the vanadium dioxide metal-insulator phase transition, Opt. Express, 18 (2010) 11192.

Canaguier-Durand A., Devaux E., George J., et al., Thermodynamics of molecules strongly coupled to the vacuum field, Angew. Chem. Int. Ed. 52 (2013) 10533.

Chang Y. W., Yao J., Zhu X. F., et al., Alternating Coupling Regimes in a Plasmon–Molecule Hybrid Structure through a Phase-Change Material, J. Phys. Chem. C 124 (2020) 22671.

Ciuti C., Bastard G., Carusotto I., Quantum vacuum properties of the intersubband cavity polariton field, Phys. Rev. B 72 (2005) 115303.

Climent C., Galego J., Garcia-Vidal F. J., et al., Plasmonic Nanocavities Enable Self-Induced Electrostatic Catalysis, Angew. Chem. Int. Ed. 58 (2019) 8698.

Coldren L. A., Corzine S. W., Mashanovitch M. L., Diode lasers and photonic integrated circuits, John Wiley & Sons, (2012).

Ćwik J. A., Kirton P., De Liberato S., et al., Excitonic spectral features in strongly coupled organic polaritons, Phys. Rev. A 93 (2016) 033840.

de Bruijn H. E., Lenferink A. T. M., Kooyman R. P. H., et al., A dielectric/metal layer system as chemical sensor, Opt. Commun. 86 (1991) 444.

Decurtins S., Gutlich P., Kohler C.P., et al., Light-induced excited spin state trapping in a transition-metal complex: the hexa-1-propyltetrazole-iron(II) tetrafluoroborate spin-crossover system, Chem. Phys. Lett. 105 (1984) 1.

Delaney M., Zeimpekis I., Lawson D., et al., A New Family of Ultralow Loss Reversible Phase-Change Materials for Photonic Integrated Circuits: Sb_2S_3 and Sb_2Se_3, Adv. Funct. Mater. 30 (2020) 2002447.

Dixon I. M., Rat S., Sournia-Saquet A., et al., On the spin-state dependence of redox potentials of spin crossover complexes, Inorg. Chem. 59 (2020) 18402.

Dong W., Liu H., Behera J. K., et al., Wide bandgap phase change material tuned visible photonics, Adv. Funct. Mater. 29 (2019) 1806181.

Dovzhenko D. S., Ryabchuk S. V., Rakovich Y. P., et al., Light–matter interaction in the strong coupling regime: configurations, conditions, and applications, Nanoscale 10 (2018) 3589.

Drickamer H. G., Pressure tuning of electronic energy levels, Int. Rev. Phys. Chem. 2 (1982) 171.

Ebbesen T. W., Hybrid light–matter states in a molecular and material science perspective, Acc. Chem. Res. 49 (2016) 2403.

Efron U., Spatial light modulators: Technology and applications, Proc. SPIE, 4457 (2001).

Ewald A. H., Martin R. L., Sinn E., et al., Electronic equilibrium between the $^6A_1$ and $^2T_2$ states in Iron(III) dithio chelates, Inorg. Chem. 8 (1969) 1837.

Félix G., Abdul-Kader K., Mahfoud T., Surface Plasmons Reveal Spin Crossover in Nanometric Layers, J. Am. Chem. Soc. 133 (2011) 15342.

Forn-Díaz P., Lisenfeld J., Marcos D., et al., Observation of the Bloch-Siegert shift in a qubit-oscillator system in the ultrastrong coupling regime, Phys. Rev. Lett. 105 (2010) 237001.

Forn-Díaz P., Lamata L., Rico E., et al., Ultrastrong coupling regimes of light-matter interaction[J]. Rev. Mod. Phys. 91 (2019) 025005.

Frisk Kockum A., Miranowicz A., De Liberato S., et al., Ultrastrong coupling between light and matter, Nat. Rev. Phys. 1 (2019) 19.

Galego J., Climent C., Garcia-Vidal F. J., et al., Cavity Casimir-Polder forces and their effects in ground-state chemical reactivity, Phys. Rev. X 9 (2019) 021057.

Garcia-Vidal F. J., Ciuti C., Ebbesen T. W., Manipulating matter by strong coupling to vacuum fields, Science, 373 (2021) eabd0336.

Gaspar A. B., Molnar G., Rotaru A., et al., Pressure effect investigations on spin-crossover coordination compounds, C. R. Chimie 21 (2018) 1095.

Gérard D., Gray S. K., Aluminium plasmonics, J. Phys. D 48 (2014) 184001.

Gütlich, P., Spin crossover in iron(II)-complexes. Structure and Bonding, 44 (1981) 83.

Gütlich P., Goodwin H. A., (eds.) Spin Crossover in Transition Metal Compounds I-III, Topics in Current Chemistry, Springer-Verlag: Berlin, Heidelberg, 233-235 (2004).

Haglund Jr. R. F., Weiss, S. M., Appavoo, K., Photonic and plasmonic modulators based on optical switching in VO_2, Quantum Sensing and Nanophotonic Devices XII, 9370, (2015) 303.

Halcrow M. A. (Ed.), Spin-crossover materials: properties and applications, John Wiley & Sons (2013).

Hauser A., Reversibility of light-induced excited spin state trapping in the $Fe(ptz)_6(BF_4)_2$ and the $Zn_{1-x}Fe_x(ptz)_6(BF_4)_2$ spin-crossover systems, Chem. Phys. Lett. 124 (1986) 543.

Hauser A., Intersystem crossing in the $[Fe(ptz)_6](BF_4)_2$ spin crossover system (ptz=1propyltetrazole), J. Chem. Phys. 94 (1991) 2741.

Hauser A., Four-wave-mixing in the Fe (II) spin-crossover system $[Zn_{1-x}Fe_x(ptz)_6](BF_4)_2$ (ptz = 1-propyltetrazole), Chem. Phys. Lett. 202 (1993) 173.

Hauser A., Ligand Field Theoretical Considerations, Top. Curr. Chem. 233 (2004) 49.

Hauser A., Light-Induced Spin Crossover and the High-Spin→Low-Spin Relaxation, Top. Curr. Chem. 234 (2004) 155.

Herrera F., Owrutsky J., Molecular polaritons for controlling chemistry with quantum optics, J. Chem. Phys. 152 (2020) 100902.

Hertzog M., Wang M., Mony J., et al., Strong light–matter interactions: a new direction within chemistry, Chem. Soc. Rev. 48 (2019) 937.

Hirai K., Hutchison J. A., Uji-i H., Recent progress in vibropolaritonic chemistry, ChemPlusChem, 85 (2020) 1981.

Hobson P. A., Barnes W. L., Lidzey D. G., et al., Strong exciton–photon coupling in a low-Q all-metal mirror microcavity, Appl. Phys. Lett. 81 (2002) 3519.

Horniichuk O. Y., Ridier K., Molnár G., et al., Solvatomorphism, polymorphism and spin crossover in bis [hydrotris (1, 2, 3-triazol-1-yl) borate] iron (II), New J. Chem. 46 (2022) 11734.

Horniichuk O. Y., Ridier K., Zhang L., et al., High-Sensitivity Microthermometry Method Based on Vacuum-Deposited Thin Films Exhibiting Gradual Spin Crossover above Room Temperature, ACS Appl. Mater. Int. 14 (2022) 52140.

Hutchison J. A., Schwartz T., Genet C., et al., Modifying chemical landscapes by coupling to vacuum fields, Angew. Chem. Int. Ed. 51 (2012) 1592.

Hutchison J. A., Liscio A., Schwartz T., et al. Tuning the work-function via strong coupling, Adv. Mater. 25 (2013) 2481.

Iazzolino A, Galle G, Degert J, et al., Impact of the spin state switching on the dielectric

constant of iron (II) spin crossover nanoparticles, Chem. Phys. Lett. 641 (2015) 14.

Kahn O., Kröber J., Jay C., Spin Transition Molecular Materials for Displays and Data Recording, Adv. Mater. 4 (1992) 718.

Kahn O., Martinez C. J., Spin-Transition Polymers: From Molecular Materials Toward Memory Devices, Science 279 (1998) 44.

Kakiuchida H., Jin P., Nakao S., et al., Optical properties of vanadium dioxide film during semiconductive–metallic phase transition, Jap. J. Appl. Phys. 46 (2007) L113.

Kang L, Jenkins R P, Werner D H., Recent progress in active optical metasurfaces, Adv. Opt. Mater. 7 (2019) 1801813.

Karvounis A., Gholipour B., MacDonald K. F., et al., All-dielectric phase-change reconfigurable metasurface, Appl. Phys. Lett. 109 (2016) 051103.

Katsidis C. C., Siapkas D. I., General transfer-matrix method for optical multilayer systems with coherent, partially coherent, and incoherent interference, Appl. Opt. 41 (2002) 3978.

Kelly, C. T., Dunne, S., Kühne, et al. Proton-Induced Spin State Switching in an FeIII Complex. Angew. Chem. Int. Ed. 62 (2023) e202217388.

Ko J. H., Yoo Y. J., Lee Y., et al., A review of tunable photonics: Optically active materials and applications from visible to terahertz, Iscience, 25 (2022) 104727.

König E., Ritter G., Kulshreshtha S. K., The nature of spin-state transitions in solid complexes of Iron(II) and the interpretation of some associated phenomena, Chem. Rev. 85 (1985) 219.

Kretschmann E., Raether H., Radiative decay of non radiative surface plasmons excited by light, Z. Naturforsch. A 23 (1968) 2135.

Ksenofontov V., Gaspar A. B., Levchenko G., et al., Pressure effect on spin crossover in $[Fe(phen)_2(NCS)_2]$ and $[CrI_2(depe)_2]$, J. Phys. Chem. B 108 (2004) 7723.

Kumar K. S., Ruben M., Emerging trends in spin crossover (SCO) based functional materials and devices, Coord. Chem. Rev. 346 (2017) 176.

Li T. E., Nitzan A., Subotnik J. E., On the origin of ground-state vacuum-field catalysis: Equilibrium consideration, J. Chem. Phys. 152 (2020) 234107.

Lidzey D. G., Bradley D. D. C., Skolnick M. S., et al., Strong exciton–photon coupling in an organic semiconductor microcavity, Nature 395 (1998) 53.

Lin L., Wang M., Wei X., et al., Photoswitchable rabi splitting in hybrid plasmon–waveguide modes, Nano Lett. 16 (2016) 7655.

Liu H., Lu J., Wang X. R., Metamaterials based on the phase transition of VO_2, Nanotechn. 29 (2017) 024002.

Liu S, Zhou K, Yuan T, et al., Imaging the thermal hysteresis of single spin-crossover nanoparticles, J. Am. Chem. Soc. 142 (2020) 15852.

Lorenc, M., Hébert, J., Moisan, N., et al., Successive dynamical steps of photoinduced switching of a molecular Fe (III) spin-crossover material by time-resolved X-ray diffraction, Phys. Rev. Lett. 103 (2009) 028301.

Loutete-Dangui E. D., Varret F., Codjovi E., et al. Thermal spin transition in $[Fe(NH_2{-}trz)_3]Br_2$ investigated by spectroscopic ellipsometry, Phys. Rev. B 75 (2007) 184425.

Malitson I. H., Interspecimen comparison of the refractive index of fused silica, J. Opt. Soc. Am. 55 (1965) 1205.

Martínez-Martínez L. A., Ribeiro R. F., Campos-González-Angulo J., et al., Can ultrastrong coupling change ground-state chemical reactions?, ACS Photonics 5 (2018) 167.

McGravey, J. J., Lawthers, I. Photochemically-induced perturbation of the 1 A⇌ 5 T equilibrium in Fe 11 complexes by pulsed laser irradiation in the metal-to-ligand charge-transfer absorption band, J. Chem. Soc. Chem. Commun. (1982) 906.

McPeak K. M., Jayanti S. V., Kress S. J. P., et al., Plasmonic films can easily be better: rules and recipes, ACS Photonics 2 (2015) 326.

Mikolasek M., Étude de la dépendance en taille des propriétés physiques des composés à transition de spin. PhD Thesis, Universite de Toulouse 3, Toulouse France (2016).

Miller K. J., Hallman K. A., Haglund R. F., et al., Silicon waveguide optical switch with embedded phase change material, Opt. Express 25 (2017) 26527.

Miller K. J., Haglund JR. R. F., Weiss S. M., Optical phase change materials in integrated silicon photonic devices: review, Opt. Mater. Express 8 (2018) 2415.

Molnár G., Rat S., Salmon L., et al., Spin Crossover Nanomaterials: From Fundamental Concepts to Devices, Adv. Mater. 30 (2018) 17003862.

Molnár G., Mikolasek M., Ridier K., et al., Molecular spin crossover materials: review of the lattice dynamical properties, Ann. Phys. 531 (2019) 1900076.

Moritomo Y., Kamiya M., Nakamur A., et al., Cooperative formation of high-spin species in a photoexcited spin-crossover complex, Phys. Rev. B 73 (2006) 012103.

Mounaix P., Freysz E., Degert J., et al., One-dimensional tunable photonic crystals with spin crossover material for the terahertz range, Appl. Phys. Lett. 89 (2006) 174105.

Nagarajan K., Thomas A., Ebbesen T. W., Chemistry under vibrational strong coupling, J. Am. Chem. Soc. 143 (2021) 16877.

Nicolazzi W., Bousseksou A., Thermodynamical aspects of the spin crossover phenomenon, C. R. Chimie 21 (2018) 1060.

Ohba, M., Yoneda, K., Agustí, G., et al., Bidirectional chemo-switching of spin state in a microporous framework. Angew. Chem. Int. Ed. 48 (2009) 4767.

Orgiu E., George J., Hutchison J. A., et al., Conductivity in organic semiconductors hybridized with the vacuum field, Nat. Mater. 14 (2015) 1123.

Palluel M., Tran N. M., Daro N., et al., The Interplay between Surface Plasmon Resonance and Switching Properties in Gold@Spin Crossover Nanocomposites, Advanced Functional Materials, Adv. Funct. Mater. 30 (2020) 2000447.

Parra J., Navarro-Arenas J., Menghini M., et al., Low-threshold power and tunable integrated optical limiter based on an ultracompact VO_2/Si waveguide, APL Photonics 6 (2021) 121301.

Pernice W. H. P., Bhaskaran H., Photonic non-volatile memories using phase change materials, Appl. Phys. Lett. 101 (2012) 171101.

Pilar P., De Bernardis D., Rabl P., Thermodynamics of ultrastrongly coupled light-matter systems, Quantum 4 (2020) 335.

Rat S., Ridier K., Vendier L., et al., Solvatomorphism and structural-spin crossover property relationship in bis[hydrotris(1,2,4-triazol-1-yl)borate]iron(II), CrystEngComm, 19 (2017) 3271.

Raoux S., Wełnic W., Ielmini D., Phase change materials and their application to nonvolatile memories, Chem. Rev. 110 (2010) 240.

Ribeiro R. F., Martínez-Martínez L. A., Du M., et al., Polariton chemistry: controlling molecular dynamics with optical cavities, Chem. Sci. 9 (2018) 6325.

Ridier, K., Molnár, G., Salmon, L., et al., Hysteresis, nucleation and growth phenomena in spin-crossover solids. Sol. State Sci. 74 (2017) A1.

Ridier K., Bas A.-C., Shalabaeva V., et al., Finite Size Effects on the Switching Dynamics of Spin-Crossover Thin Films Photoexcited by a Femtosecond Laser Pulse, Adv. Mater. 31 (2019) 1901361.

Ridier, K., Bas, AC., Zhang, Y. et al., Unprecedented switching endurance affords for high-resolution surface temperature mapping using a spin-crossover film, Nat. Commun. 11 (2020) 3611.

Roeloffzen C. G. H., Zhuang L., Taddei C., et al., Silicon nitride microwave photonic circuits, Opt. Express 21 (2013) 22937.

Roux C., Zarembowitch J., Gailois B., et al., Toward ligand-driven light-induced spin change. Influence of the configuration of 4-Styrylpyridine (stpy) on the magnetic properties of Fe^{II} $(stpy)_4(NCS)_2$ complexes. Crystal Structures of the spin-crossover species $Fe(trans\text{-}stpy)_4(NCS)_2$ and of the high-spin species $Fe(cis\text{-}stpy)_4(NCS)_2$, Inorg.Chem. 33 (1994) 2273.

Rudé M., Pello J., Simpson R. E., et al., Optical switching at 1.55 μ m in silicon

racetrack resonators using phase change materials, Appl. Phys. Lett. 103 (2013) 141119.

Ryckman J. D., Diez-Blanco V., Nag J., et al., Photothermal optical modulation of ultra-compact hybrid Si-VO 2 ring resonators, Opt. Express 20 (2012) 13215.

Salamon Z., Macleod H. A., Tollin G., Coupled plasmon-waveguide resonators: a new spectroscopic tool for probing proteolipid film structure and properties, Biophys. J. 73 (1997) 2791.

Savona V., Andreani L. C., Schwendimann P., et al., Quantum well excitons in semiconductor microcavities: Unified treatment of weak and strong coupling regimes, Sol. State Commun. 93 (1995) 733.

Schleicher F., Studniarek M., Kumar K. S., et al., Linking electronic transport through a spin crossover thin film to the molecular spin state using X-ray absorption spectroscopy, ACS Appl. Mater. Interf. 10 (2018) 31580.

Schwartz T., Hutchison J. A., Genet C., et al., Reversible switching of ultrastrong light-molecule coupling, Phys. Rev. Lett. 106 (2011) 196405.

Shalabaeva V., Rat S., Manrique-Juarez M. D., et al., Vacuum deposition of high-quality thin films displaying spin transition near room temperature, J. Mater. Chem. C 5 (2017) 4419.

Shalabaeva V., Mikolasek M., Manrique-Juarez M. D., et al., Unprecedented size effect on the phase stability of molecular thin films displaying a spin transition, J. Phys. Chem. C 121 (2017) 25617.

Shalabney A., George J., Hutchison J., et al., Coherent coupling of molecular resonators with a microcavity mode[J]. Nat. Commun. 6 (2015) 5981.

Simpkins B. S., Dunkelberger A. D., Owrutsky J. C., Mode-specific chemistry through vibrational strong coupling (or a wish come true), J. Phys. Chem. C 125 (2021) 19081.

Simpson R. E., Yang J. K. W., Hu J., Are phase change materials ideal for programmable photonics?: opinion, Opt. Mater. Express 12 (2022) 2368.

Sorai M., Seki S., Magnetic heat capacity due to cooperative low-spin $^{1}A_{1}$ ⇋ high-spin $^{5}T_{2}$ transition in $Fe(phen)_2(NCS)_2$ crystal, J. Phys. Soc. Jap. 33 (1972) 575.

Sorai M., Seki S., Phonon coupled cooperative low-spin $^{1}A_{1}$ ⇋ high-spin $^{5}T_{2}$ transition in $[Fe(phen)_2(NCS)_2]$ and $[Fe(phen)_2(NCSe)_2]$ crystals, J. Phys. Chem. Solids 35 (1974) 555.

Spiering H., Elastic Interaction in Spin Crossover Compounds, Top. Curr. Chem. 235 (2004) 171.

Stegmaier M., Rıos C., Bhaskaran H., et al., Thermo-optical effect in phase-change nanophotonics, ACS Photonics 3 (2016) 828.

Tanabe Y., Sugano S., On the Absorption Spectra of Complex Ions II, J. Phys. Soc. Jpn.

9 (1954) 766.

Thomas A., George J., Shalabney A., et al., Ground-state chemical reactivity under vibrational coupling to the vacuum electromagnetic field, Angew. Chem. Int. Ed. 55 (2016) 11462.

Thomas A., Lethuillier-Karl L., Nagarajan K., et al., Tilting a ground-state reactivity landscape by vibrational strong coupling, Science 363 (2019) 615.

Thomas A., Jayachandran A., Lethuillier-Karl L., et al., Ground state chemistry under vibrational strong coupling: dependence of thermodynamic parameters on the Rabi splitting energy, Nanophotonics 9 (2020) 249.

Thomas P. A., Tan W. J., Fernandez H. A., et al., A new signature for strong light–matter coupling using spectroscopic ellipsometry, Nano Lett. 20 (2020) 6412.

Thomas P. A., Menghrajani K. S., Barnes W. L., All-optical control of phase singularities using strong light-matter coupling, Nat. Commun. 13 (2022) 1809.

Törmä P., Barnes W. L., Strong coupling between surface plasmon polaritons and emitters: a review, Rep. Prog. Phys. 78 (2014) 013901.

Tuchagues J. P., Bousseksou A., Molnár G., et al., The role of molecular vibrations in the spin crossover phenomenon, Top. Curr. Chem. 235 (2004) 85.

Vef A., Manthe U., Gütlich P., et al., Intersystem crossing dynamics in the spin–crossover systems $[M:Fe(pic)_3]Cl_2 \cdot Sol$ (M=Mn or Zn, Sol=MeOH or EtOH), J. Chem. Phys. 101 (1994) 9326.

Wan C., Zhang Z., Salman J., et al., Ultrathin broadband reflective optical limiter, Laser Photon. Rev. 15 (2021) 2100001.

Wang S., Chervy T., George J., et al., Quantum yield of polariton emission from hybrid light-matter states, J. Phys. Chem. Lett. 5 (2014) 1433.

Wang S., Mika A., Hutchison J. A., et al., Phase transition of a perovskite strongly coupled to the vacuum field, Nanoscale 6 (2014) 7243.

Williams C., Hong N., Julian M., et al., Tunable mid-wave infrared Fabry-Perot bandpass filters using phase-change GeSbTe, Opt. Express 28 (2020) 10583.

Windt D. L., IMD—Software for modeling the optical properties of multilayer films, Comp. Phys. 12 (1998) 360.

Wuttig M., Bhaskaran H., Taubner T., Phase-change materials for non-volatile photonic applications, Nat. Photonics 11 (2017) 465.

Yang Z., Ko C., Ramanathan S., Oxide electronics utilizing ultrafast metal-insulator transitions, Annual Rev. Mater. Res. 41 (2011) 337.

Zarembowitch J. Electronic spin crossovers in solid-state molecular compounds-some new aspects concerning cobalt (II) complexes. New J. Chem. 16 (1992) 255.

Zarembowitch J., Roux C., Boillot M.L., et al., Temperature-, Pressure-, and light-induced electronic spin conversions in transition metal complexes, Mol. Cryst. Liq. Cryst. 234 (1993) 247.

Zhang Q., Zhang Y., Li J., et al., Broadband nonvolatile photonic switching based on optical phase change materials: beyond the classical figure-of-merit, Opt. Lett. 43 (2018) 94.

Zhang Y., Chou J.B., Li J. et al. Broadband transparent optical phase change materials for high-performance nonvolatile photonics, Nat. Commun. 10 (2019) 4279.

Zhang Y., Ridier K., Shalabaeva V., et al., A molecular spin-crossover film allows for wavelength tuning of the resonance of a Fabry–Perot cavity, J. Mater. Chem. C 8 (2020) 8007.

Zheng J., Khanolkar A., Xu P., et al., GST-on-silicon hybrid nanophotonic integrated circuits: a non-volatile quasi-continuously reprogrammable platform, Opt. Mater. Express 8 (2018) 1551.

Zilun G., Fuyi Y., Letian W., et al., Phase change materials in photonic devices, J. Appl. Phys. 129 (2021) 030902.

Zuliani P., Palumbo E., Borghi M., et al., Engineering of chalcogenide materials for embedded applications of Phase Change Memory, Sol. State Electr. 111 (2015) 27.

RESUME FRANCAISE

(French language summary)

Introduction générale

Les nanomatériaux qui subissent une transition de phase électronique et/ou structurelle, associée à un changement réversible des propriétés optiques, ont récemment fait l'objet d'une attention croissante pour le développement de dispositifs photoniques actifs [Kevin 2018; Gong 2021] ainsi que pour la recherche fondamentale sur les interactions lumière-matière. Ces matériaux à changement de phase (PCM) présentent d'importants variations de l'indice de réfraction complexe en réponse à un stimulus externe (par exemple la chaleur, la tension de polarisation ou l'irradiation lumineuse), qui a été exploité pour une variété d'applications photoniques telles que les fenêtres intelligentes, [Beeckman 2011] les mémoires optiques, [Wuttig 2017] les modulateurs spatiaux de lumière [Zhang 2019] et les circuits intégrés photoniques (PIC). Les PCM les plus étudiés sont les oxydes de métaux de transition présentant une transition métal-isolant, les alliages de chalcogénures présentant un changement de phase amorphe-cristallin et les cristaux liquides présentant des transitions de type ordre-désordre. [Gong 2021 ; Beeckman 2011 ; Wuttig 2017 ; Zhang 2019 ; Delaney 2020 ; Kevin 2018]. Cependant, parmi ces matériaux, seuls les cristaux liquides ont été facilement utilisés dans des applications nécessitant une transparence dans la gamme spectrale visible. Par ailleurs, le champ d'application des cristaux liquides reste limité par les taux de commutation lents et les pertes de diffusion élevées [Beeckman 2011], ainsi que par la nécessité de les encapsuler.

Dans ce contexte, les composés moléculaires à transition de spin (SCO) représentent une nouvelle classe prometteuse de matériaux à changement de phase avec un potentiel élevé pour les applications photoniques actives. Ces complexes de métaux de transition sont connus pour présenter une commutation rapide et réversible de l'état de spin entre les configurations électroniques à faible spin (LS) et à haut spin (HS) de l'ion métallique central sous divers stimuli [Gütlich 2004; Molnár 2018]. Des études expérimentales et théoriques visant à élucider le mécanisme de commutation entre les configurations électroniques à haut spin (HS) et à bas spin (LS) de l'ion métallique central sont en cours depuis près d'un siècle et un certain nombre de revues et de livres récents

indiquent l'intérêt continu pour ce sujet [Gütlich 2004; Bousseksou 2011; Halcrow 2013; Kumar 2017]. Au cours de la dernière décennie, l'attention portée aux matériaux SCO pour les applications technologiques s'est considérablement accrue grâce à des avancées majeures dans la synthèse et la manipulation de nanomatériaux SCO sous diverses formes telles que les nanoparticules, les films minces, les nanostructures, les nano-hétérostructures et les nanocomposites [Molnár 2018].

Sur la base de ces avancées, cette thèse se concentre sur les dispositifs optiques actifs à base de SCO et tire parti du fait que le changement de spin s'accompagne de changements substantiels dans les propriétés optiques. Considérant l'indice de réfraction complexe n* = n + ik, avec une partie réelle (indice de réfraction, n) et une partie imaginaire (coefficient d'extinction, k), nous proposons deux stratégies de recherche. La première stratégie exploite la variation de l'indice de réfraction au niveau du SCO pour mettre en œuvre une modulation active des dispositifs optiques. La seconde stratégie, sans précédent, se concentre sur le coefficient d'extinction k et étudie l'influence des changements d'absorbance sur le degré d'hybridation entre les molécules SCO et les modes électromagnétiques dans les cavités optiques.

Le contexte scientifique et les résultats obtenus au cours de ce travail de thèse sont décrits dans trois chapitres.

Le chapitre 1 présente une introduction au phénomène de Transition de Spin (SCO). Le mécanisme moléculaire de la transition de spin est brièvement rappelé à l'aide de la théorie du champ cristallin. Ensuite, nous décrivons les comportements SCO les plus couramment observés (graduel, abrupt, par étapes) et la notion de coopérativité. Nous discutons ensuite de l'effet de la température, de la pression et de l'irradiation lumineuse sur l'état de spin des molécules. Enfin, les changements de propriétés physiques qui en résultent et les méthodes de caractérisation associées sont aussi passés en revue. L'accent étant mis sur les propriétés optiques (indice de réfraction et les changements de couleur).

Le chapitre 2 est consacré à la modification de l'indice de réfraction des matériaux

SCO dans le contexte des dispositifs optiques actifs. Nous étudions deux résonateurs différents basés sur des couches minces du même complexe SCO **1** [Fe(HB(1,2,4-triazol-1-yl)3)2]. Tout d'abord, nous discutons de la fabrication et des propriétés des cavités Fabry-Pérot Ag/**1**/Ag, qui se composent de deux couches d'argent parallèles comme miroirs et d'un film de **1** comme couche diélectrique prise en sandwich entre les deux couches métalliques. Cette étude est suivie par celle des résonateurs bicouches Ag/**1**, excités dans une géométrie de réflexion interne totale (TIR) à l'aide d'un prisme de couplage. Les propriétés optiques de ces deux résonateurs sont étudiées en mesurant les spectres de résonance en fonction de l'angle d'incidence, de la polarisation et de la température. Nous évaluons plusieurs facteurs de mérite importants, tels que le décalage de la longueur d'onde de résonance en fonction de la température, le facteur de qualité et le contraste de réflectance (ou de transmittance) réalisable. Enfin, nous exploitons cette ‘‘accordabilité’’ pour démontrer la non-linéarité photo-thermique et l'application de la limitation optique pour le résonateur bicouche Ag/**1**.

Le chapitre 3 propose, pour la première fois, une stratégie basée sur la variation du coefficient d'extinction *k* en fonction de la force d'hybridation lumière-matière, induite par le phénomène SCO. À cette fin, nous avons utilisé des résonateurs bicouches Al/SCO, constitués de films minces des complexes [Fe(HB(1,2,4-triazol-1-yl)$_3$)$_2$] **1**, et [Fe(HB(1,2,3-triazol-1-yl)$_3$)$_2$] **2**, présentant des transitions SCO abrupts et graduels, respectivement. Le mode de la cavité a été mis en résonance avec une transition dipolaire optique dans l'état bas spin des complexes, ce qui permet une hybridation forte. La force du couplage a ensuite été étudiée par la commutation thermiquement induite des molécules entre leurs états bas spin et haut spin, offrant la possibilité attrayante d'une commutation réversible entre les régimes de couplage ultra-fort et faible à l'intérieur de la cavité.

La thèse se termine par quelques conclusions générales et des perspectives pour des travaux ultérieurs.

Chapitre 1 : Brève introduction au phénomène de transition de spin

Les molécules à transition de spin sont des complexes de métaux de transition octaédriques avec des configurations électroniques $3d^4$-$3d^7$, impliquant des complexes de Cr^{II}, Mn^{III}, Mn^{II}, Fe^{III}, Fe^{II}, Co^{III} et Co^{II}. Lorsqu'ils sont soumis à des stimuli externes (tels que la température, la pression, le rayonnement lumineux, etc.), ces complexes de métaux de transition peuvent passer de manière réversible d'une configuration électronique haut spin à une configuration électronique bas spin, appelée "Spin Crossover" (SCO) qui s'accompagne de changements de longueurs et d'angles de liaison et, d'une variété de changements de propriétés physiques telles que le moment magnétique, la permittivité diélectrique, la capacité calorifique, les constantes élastiques et la couleur. Ce phénomène de SCO peut être par conséquent caractérisé par une pléthore de techniques, notamment les mesures de susceptibilité magnétique, la spectroscopie électronique (UV-VIS), la spectroscopie vibrationnelle (Raman, FTIR), la diffraction des rayons X, la spectroscopie diélectrique, la calorimétrie, etc. Il est important de noter que dans les matériaux massifs, la manifestation du phénomène SCO est considérablement modifiée par les interactions élastiques à courte et longue portée entre les molécules dans le réseau cristallin, alors que dans les matériaux à l'échelle nanométrique, l'influence des propriétés de surface/interface doit également être prise en compte. Potentiellement, les matériaux à transition de spin offrent un large éventail d'applications technologiques dans les capteurs, des dispositifs d'affichage, d'actionnement et de traitement de l'information. Dans ce chapitre, après une introduction générale, nous nous concentrons principalement sur les changements de propriétés optiques accompagnant la commutation de l'état de spin et sur les idées d'application associées.

Pour comprendre l'origine du phénomène de changement d'état de spin dans les complexes de métaux de transition, nous devons d'abord examiner l'effet des ligands sur l'ion métallique central [Hauser 2004a; Gütlich 2004b]. L'approche la plus simple

est la théorie dite du champ cristallin qui considère que l'interaction entre l'ion du métal de transition et les ligands est analogue à l'attraction électrostatique des ions positifs et négatifs dans les cristaux ioniques. Le rôle des ligands est d'établir le champ potentiel de charge négative, appelé champ cristallin. Sous l'effet de la perturbation du champ cristallin, les orbitales 3d dégénérées de l'ion métallique subissent un éclatement des niveaux d'énergie.

En prenant l'exemple des complexes Fe(II), qui ont été utilisés dans cette thèse, les six électrons des orbitales 3d peuvent avoir deux arrangements différents en fonction des magnitudes relatives du gap d'énergie dû au champ cristallin, 10Dq, et de l'énergie d'appariement de spin, Π. Comme le montre la figure 1.1, dans un champ cristallin faible (10Dq < Π), les six électrons occuperont chacune des orbitales 3d. Dans ce cas, le nombre d'électrons non appariés dans le système est de 4, le moment angulaire de spin total est donc S = 4 x ½ = 2, ce qui donne une multiplicité de spin maximale 2S+1 = 5. Ce complexe paramagnétique est appelé 'haut spin' (HS). À l'inverse, dans un champ cristallin intense (10Dq > Π), les électrons occuperont préférentiellement les orbitales t_{2g} de faible énergie. Dans ce cas, il n'y a pas d'électrons non appariés, S = 0, ce qui donne la plus petite multiplicité de spin (2S+1=1). Ce complexe diamagnétique est appelé 'bas spin' (LS).

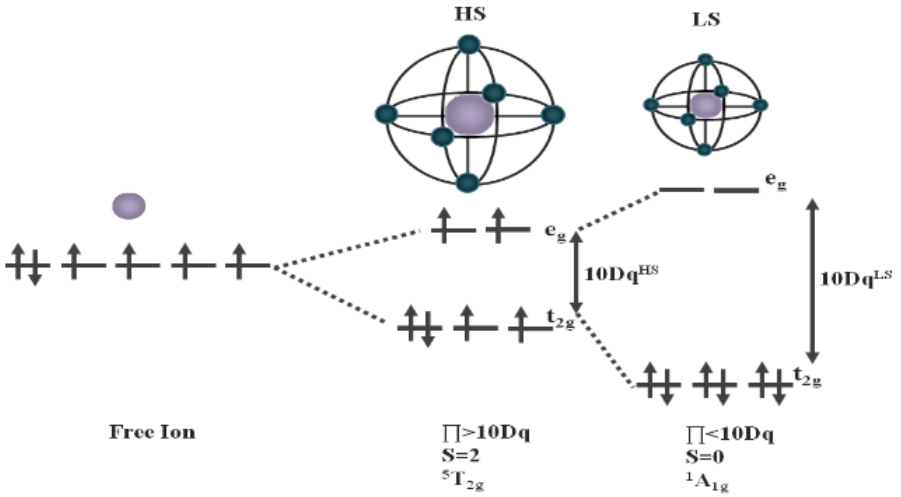

Figure 1.1. Séparation énergétique des orbitales 3d d'un ion Fe(II) dans un environnement octaédrique induit par le champ des ligands (10Dq) - montrant à la fois les cas de champ faible (HS) et de champ fort (LS).

La courbe de transition de spin décrit la fraction molaire de l'état haut spin du complexe, γHS(T), en fonction de la température. La forme de la courbe de transition de spin permet de déduire de nombreuses informations, telles que le degré de coopérativité du système [Nicolazzi 2018]. Les courbes de transition de spin les plus courantes sont données dans la figure 1.2: (a) Transition de spin graduelle, (b) Transition de spin abrupte, (c) Transition de spin avec hystérésis, (d) Transition de spin à plusieurs étapes, (e) Transition de spin incomplète.

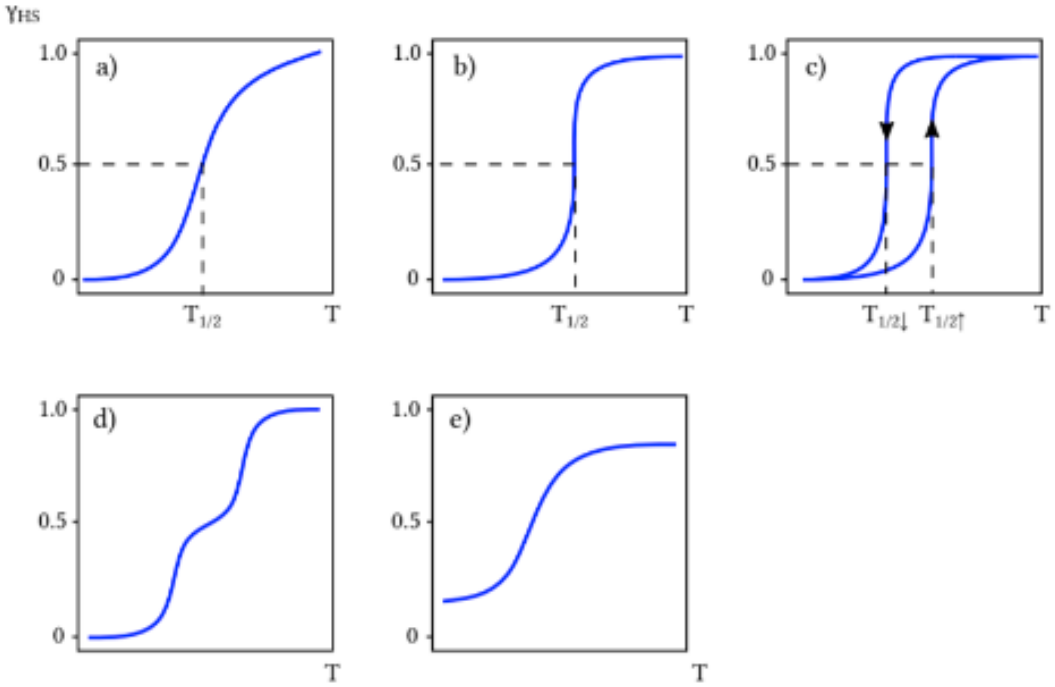

Figure 1.2. Principaux types de courbes de transition de spin sous l'effet de la température. a) Transition de spin graduelle. b) Transition de spin abrupte. c) Transition de spin avec hystérésis. d) Transition de spin en deux étapes. e) Transition de spin incomplète [Gütlich 2004].

L'énergie nécessaire pour induire le phénomène de transition de spin peut être récoltée à partir de stimuli externes. Nous présentons ici les stimuli les plus courants: la température, l'irradiation lumineuse et la pression [Gütlich 2004b]. Toutefois, il convient de noter que les transitions de spin peuvent également être induites par un champ magnétique intense et l'adsorption de molécules de gaz/vapeur.

En raison du fort couplage électronique-réseau (électron-phonons), le processus de transition de spin s'accompagne de changements de pratiquement toutes les propriétés

physiques du matériau (telles que les propriétés magnétiques, optiques, structurales, élastiques, thermiques, etc.), de sorte qu'il existe une série de méthodes expérimentales correspondantes (telles que la magnétométrie, la spectroscopie électronique, les spectroscopies vibrationnelles et optiques, les mesures mécaniques, la calorimétrie, etc). Dans ce qui suit, nous nous concentrerons sur l'étude des propriétés optiques et les méthodes de détection optique.

Une des caractéristiques des plus intéressantes de la transition de spin est le changement des propriétés d'absorption optique du matériau. Cela s'explique évidemment par le fait que le changement d'état électronique (entre HS et LS) entraîne inévitablement une modification de toutes les transitions de champ de ligand centrées sur le métal et que l'on s'attend également à une modification significative des transitions de transfert de charge métal-ligand et ligand-métal. Par conséquent, l'un des aspects les plus frappants (et les plus connus) de la transition de spin est le changement de couleur spectaculaire du matériau. C'est la propriété appelée thermochromisme, photochromisme ou piézochromisme, en fonction des stimuli utilisés [Hauser 2004b]. À titre d'exemple, la figure 1.3 présente les spectres d'absorption d'un monocristal du composé $[Fe(ptz)_6](BF_4)_2$ dans les deux états de spin, ainsi que les photographies du cristal montrant le changement de couleur correspondant, du rose dans l'état LS à l'incolore dans l'état HS. De façon plus détaillée, dans l'état LS, le spectre montre deux bandes d'absorption du champ de ligands, $^1A_1 \rightarrow {}^1T_1$ et $^1A_1 \rightarrow {}^1T_2$, la première apparaissant dans le visible (18500 cm-1, $\lambda \approx 540$ nm) tandis que la seconde dans la région ultraviolette (26500 cm-1, $\lambda \approx 375$ nm). Par conséquent, comme le cristal dans l'état LS absorbe principalement dans le vert, il apparaît dans la couleur complémentaire, c'est-à-dire le rose. Lorsque le cristal passe à l'état HS, le spectre ne montre qu'une bande d'absorption d-d dans le proche infrarouge (NIR) (11800 cm-1, $\lambda \approx 850$ nm), provenant de la transition $^5T_2 \rightarrow {}^5E$, tandis qu'aucune absorption significative ne se produit dans le domaine visible, ce qui explique pourquoi le cristal apparaît incolore.

Outre le changement de la partie imaginaire (coefficient d'extinction, k) de l'indice de réfraction complexe $n^* = n + ik$, directement associé au changement d'absorption

optique, le phénomène SCO s'accompagne également d'un changement significatif de la partie réelle n [Hauser 1993]. Jusqu'à présent, seules quelques études ont été consacrées à la commutation de l'indice de réfraction des composés SCO dans la région optique. Ces recherches visaient soit à utiliser des principes photoniques pour détecter l'occurrence du phénomène de transition de spin ("photonique pour SCO"), soit, à l'inverse, à utiliser les propriétés optiques commutables des molécules SCO dans des dispositifs photoniques actifs ("SCO pour photonique").

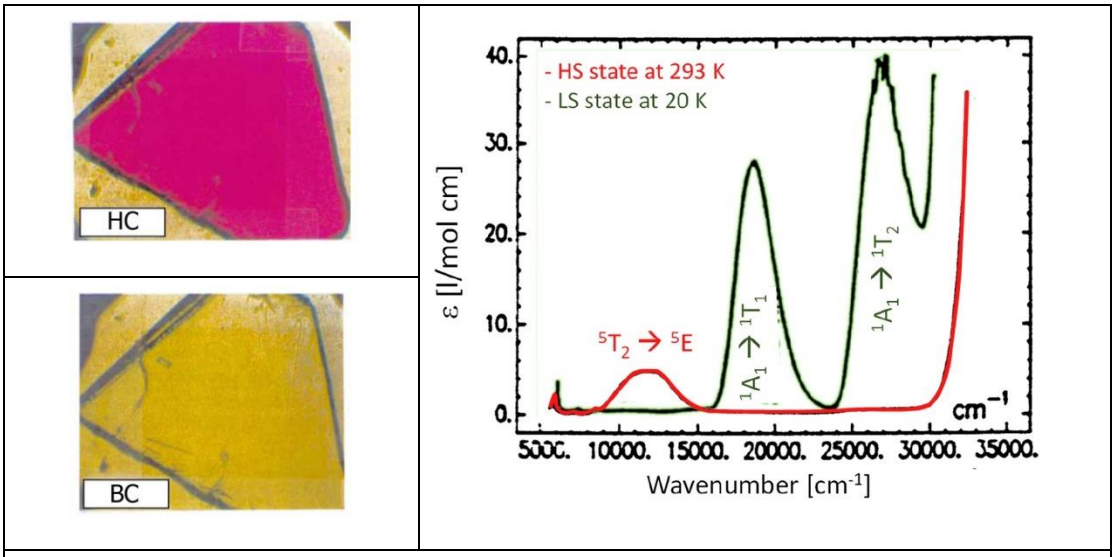

Figure 1.3. Images d'un cristal du composé $[Fe(ptz)_6](BF_4)_2$ à 20 K (en haut, état LS) et à 293 K (en bas, état HS), et les spectres d'absorption optique correspondants [Hauser 1991].

Par exemple, la spectroscopie de résonance plasmonique de surface (SPR) - en raison de sa grande sensibilité au changement d'indice de réfraction - s'est révélée extrêmement prometteuse pour la détection et l'étude du phénomène de la transition de spin dans des films ultraminces (< 10 nm) [Félix 2011], c'est-à-dire à une échelle de taille où la plupart des techniques de caractérisation en laboratoire échouent. Les polaritons plasmoniques de surface (SPP) sont des ondes électromagnétiques guidées qui se propagent à l'interface entre des couches métalliques et diélectriques sous l'excitation de la lumière, qui peuvent être couplées à la lumière incidente à l'aide d'un prisme (voir figure 1.4a). Pour bénéficier de la sensibilité de la technique SPP, un

échantillon multicouche, composé de verre/Ti (5 nm)/Au (45 nm)/$[Fe(hptrz)_3](OTs)_2$ (30 nm) a été fabriqué par Félix et el. [Félix 2011]. Les spectres de réflectivité angulaire ont montré un déplacement évident du "creux SPR" (l'angle correspondant est appelé "angle de résonance plasmonique",θ_{SPR}) entre les états LS et HS (voir figure 1.4b). La dépendance en température de l'angle θ_{SPR} démontre la température de transition de spin autour de 320 K, accompagnée d'une boucle d'hystérésis d'environ 3 K dans une couche mince de 30 nm (voir figure 1.4c). Le déplacement de l'angle de résonance plasmonique a été attribué au changement d'indice de réfraction en utilisant des calculs de matrice de transfert. [Félix 2011]

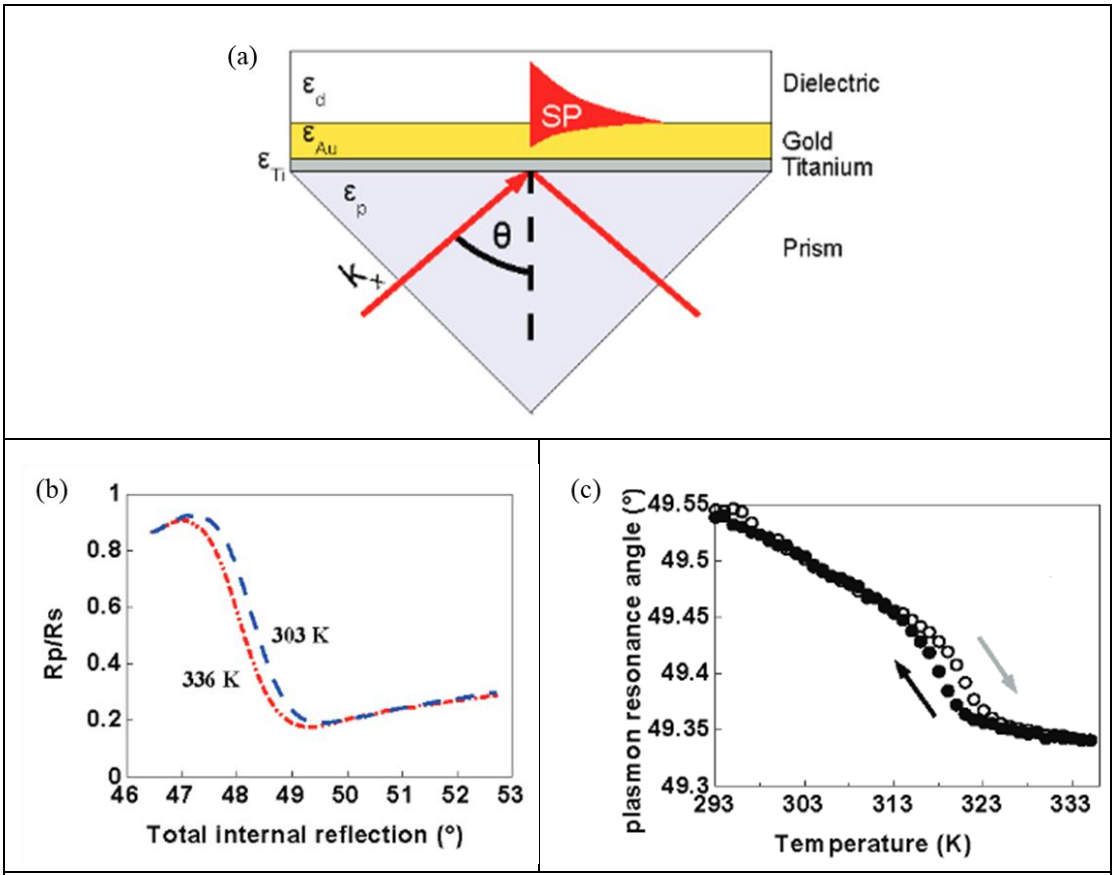

Figure 1.4. (a) Schéma du dispositif multicouche verre/Ti/Au/SCO. (b) Spectres de réflectance en fonction de l'angle d'une multicouche verre/Ti (5 nm)/Au (45 nm)/$[Fe(hptrz)_3](OTs)_2$ (30 nm) à 303 K (état LS) et 336 K (état HS) (λ= 660 nm). Rp et Rs se réfèrent à la réflectance de la lumière polarisée p et s, respectivement. (c) Dépendance en température de l'angle de résonance plasmonique (minima de réflectance) de la multicouche dans les modes de chauffage et de refroidissement (dT/dt= 2 K/min). [Félix 2011]

Chapitre 2 : Résonateurs optiques multicouches accordables basés sur la commutation de l'indice de réfraction SCO

Dans les vastes domaines de l'optique et de la photonique, l'accordabilité, la reconfigurabilité et l'adaptabilité sont des atouts majeurs, très demandés pour diverses applications [Kang 2019 ; Ko 2022]. Celles-ci comprennent, par exemple, les écrans pour l'affichage, les mémoires optiques, les modulateurs spatiaux de lumière (SLM), les circuits intégrés photoniques (PIC), les réseaux neuronaux optiques et d'autres approches pour l'informatique optique. Notamment, il y a eu récemment une explosion d'intérêt pour les fonctionnalités actives permettant une modification contrôlée de la phase et/ou de l'amplitude des fronts d'onde optiques dans les SLM (par exemple, orientation du faisceau, affichages holographiques, correction de la distorsion) [Efron 2001], ou pour le routage de la lumière à travers des PIC (par exemple, commutateurs optiques, modulateurs, filtres, limiteurs) [Coldren 2012].

Fondamentalement, il existe deux façons d'obtenir des propriétés optiques actives ou adaptatives, qui comprennent (i) la modification de la géométrie de la structure par déplacement(s) mécanique(s) (par exemple, micro-miroirs, miroirs déformables), et (ii) l'utilisation de matériaux dont l'indice de réfraction est contrôlable.

Dans ce chapitre, en utilisant le changement de la partie réelle de l'indice de réfraction qui accompagne le phénomène de transition de spin, nous visons à démontrer la possibilité d'utiliser des films minces de matériaux SCO comme éléments actifs dans des dispositifs optiques accordables fonctionnant dans le domaine des longueurs d'onde visibles. En particulier, deux résonateurs optiques à base de SCO (la cavité Fabry-Pérot Ag/SCO/Ag et la structure bicouche résonante Ag/SCO), avec des géométries différentes, ont été considérés et étudiés.

Pour mener à bien ces recherches, nous avons choisi le composé SCO [Fe(HB(1,2,4-triazol-1-yl)$_3$)$_2$] qui présente l'avantage de montrer une transition de spin extrêmement robuste et reproductible au-dessus de la température ambiante, et qui est un complexe

sublimable sous vide, ce qui signifie qu'il peut être déposé sous la forme de films minces homogènes et de haute qualité par évaporation thermique sous vide. En accord avec les résultats précédents dans l'équipe [Shalabeava 2017a], les spectres d'absorbance des films de **1**, déposés sur des substrats de silice fondue, présentent des bandes d'absorption intenses et dépendantes du SCO dans la gamme spectrale UV (voir Figure 2.1a). Plus précisément, à température ambiante (à l'état LS), le complexe **1** présente trois bandes autour de 272, 305 et 317 nm. Compte tenu des coefficients d'absorption élevés associés à ces pics (environ 10^4 cm^{-1}), ils correspondent probablement à des transitions de transfert de charge (métal-ligand et/ou ligand-métal). Comme le montre la figure 2.1a, ces bandes d'absorption sont complètement éffacées lorsque le film est chauffé au-dessus de la température de transition de spin, l'état HS étant totalement transparent dans la gamme spectrale 250-800 nm. En suivant l'évolution de la température de l'absorbance optique à la longueur d'onde λ = 317 nm (figure 2.1b), nous observons que les films de **1** présentent une transition de spin abrupte centrée autour de 64 °C, s'étendant sur une plage de température d'environ 12 °C.

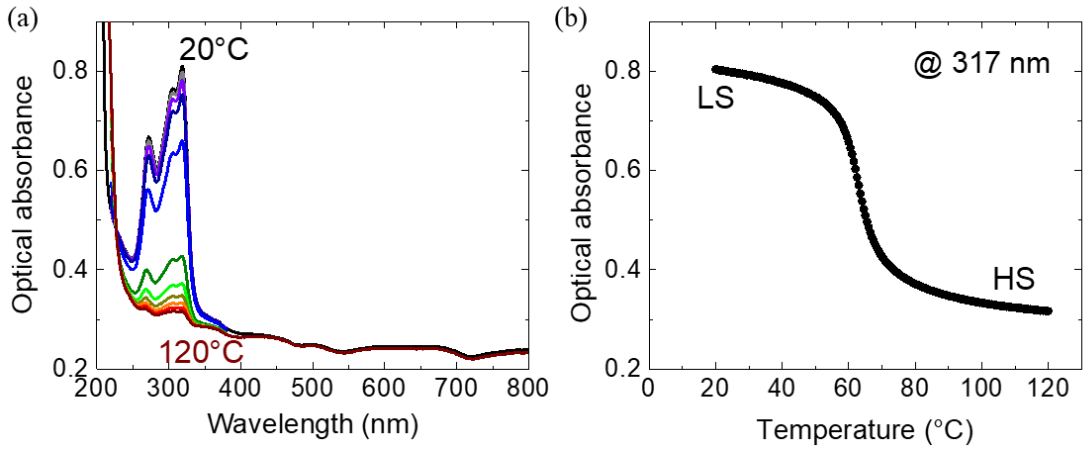

Figure 2.1. (a) Spectres d'absorbance optique d'un film de 138 nm d'épaisseur du complexe **1**, enregistrés à des températures entre 20 et 120 °C. Les films ont été déposés sur des substrats en silice fondue. (b) Courbe de transition de spin thermique du film, extraite de la variation thermique de l'absorbance optique à λ = 317 nm.

Sur la base de ces études précédentes, nous avons fabriqué une série de cavités Fabry-Pérot Ag/**1**/Ag, incorporant un film mince de composé **1**, dans le but de mener une étude

plus approfondie des propriétés optiques de ce résonateur et de son accordabilité thermique. Pour mieux suivre l'effet de la transition de spin induite thermiquement, la figure 2.2a montre l'évolution de la température du mode polarisé s de la cavité à un angle d'incidence fixé à θ = 60°, à la fois en mode chauffage et en mode refroidissement. La transition de spin de l'état LS à l'état HS dans la cavité donne lieu à une chute abrupte de la longueur d'onde de résonance à proximité de 65 °C, qui est entièrement réversible lors du refroidissement.

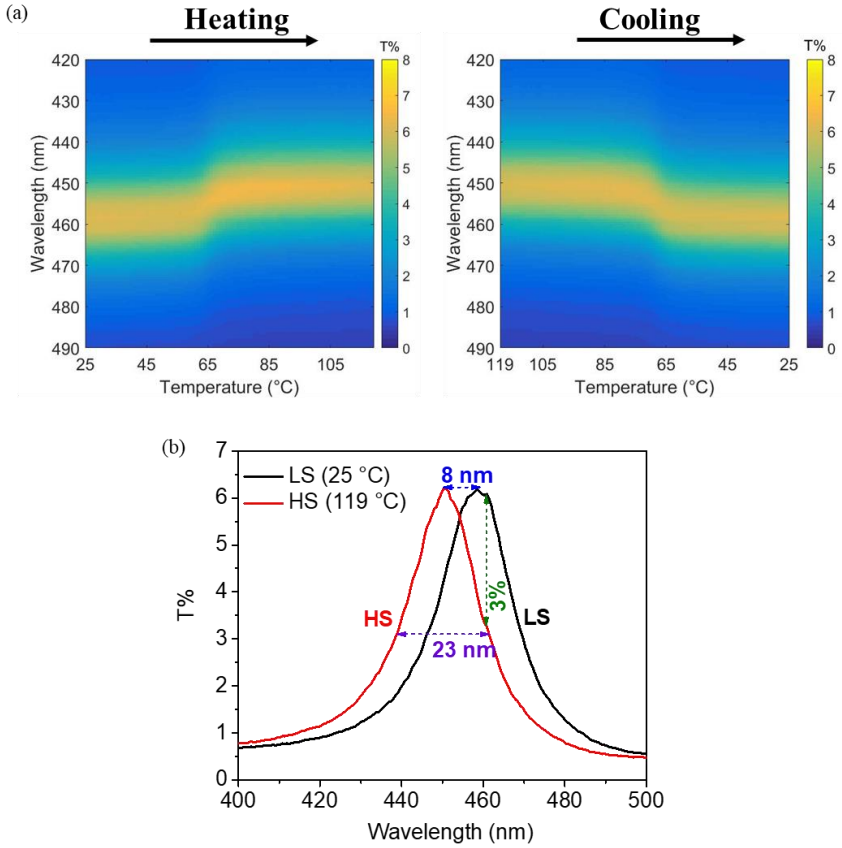

Figure 2.2. (a) Evolution du mode résonnant polarisé s de la cavité Ag (40 nm)/**1** (142 nm)/Ag (40 nm), mesuré en fonction de la température à un angle d'incidence fixé à θ= 60°, lors du chauffage et du refroidissement entre 25 et 119 °C. (b) Spectres de transmittance en polarisation s enregistrés pour la même cavité à un angle d'incidence de θ = 60° dans les états LS et HS.

La figure 2.2b montre le spectre de transmittance de cette cavité pour le mode polarisé s à un angle d'incidence fixé à θ = 60° à 25 °C (LS) et à 119 °C (HS). Cette figure montre un décalage d'environ 8 nm de la longueur d'onde de résonance entre les états LS et HS, ce qui donne lieu à une modulation de la transmittance d'environ 3 % (au

maximum). Il est clair que cette faible modulation résulte de la largeur de bande relativement élevée du pic de résonance (environ 23 nm) et, plus important encore, de la faible transmittance du dispositif (environ 6 %). On notera que l'intensité de la résonance est la même dans les deux états de spin, ce qui signifie clairement que la modulation est exclusivement liée au changement de la partie réelle de l'indice de réfraction associé avec le phénomène de transition de spin. Pour conclure, les travaux sur les résonateurs Ag/**1**/Ag ont démontré qu'en utilisant des complexes SCO à faibles coefficients d'extinction et à forts changements d'indice de réfraction entre les deux états de spin, des dispositifs optiques actifs peuvent être fabriqués et utilisés dans la gamme spectrale visible. Notamment, l'empilement multicouche [Ag (40 nm)/**1** (142 nm)/Ag (40 nm)] présente un décalage de la longueur d'onde de résonance allant jusqu'à 8 nm. Cependant, le contraste de transmission réalisable reste relativement faible (environ 3 %), ce qui n'est pas favorable aux applications pratiques.

Afin de palier au problème de la faible modulation optique, nous avons conçu et fabriqué un nouveau type de résonateur optique, qui consiste en une simple structure bicouche Ag/**1**, excitée à l'aide d'un prisme de couplage, et fonctionnant dans une géométrie de réflexion interne totale (TIR). En effet, les résonances dans nos bicouches Ag/SCO ne peuvent être excitées que dans des conditions spécifiques, que nous avons obtenues en utilisant la méthode de Kretschmann (voir figure 2.3), en employant un prisme de verre comme milieu de couplage [Kretschmann 1968].

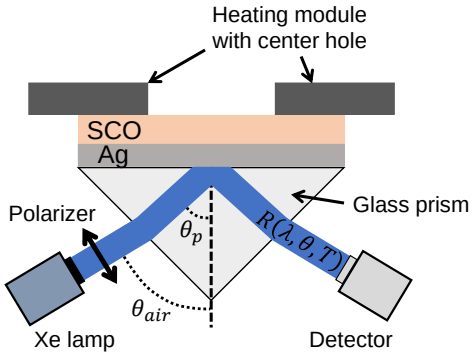

Figure 2.3. Schéma du dispositif du mesure de réflexion interne totale atténuée, utilisée pour coupler la lumière au résonateur formé par la bicouche Ag (35 nm)/**1** (162 nm) déposée sur un prisme en verre.

La figure 2.4a montre des spectres de réflectance polarisés en s du résonateur, enregistrés à un angle d'incidence de θair = 68°, pour des températures sélectionnées. Il est important de noter que nous observons un décalage important (jusqu'à 46 nm) du pic de résonance lors du chauffage de 25 à 120 °C. Ce décalage est plus important que la largeur de bande spectrale du mode résonant (*FWHM* = 37 nm). En outre, il convient de mentionner que la majeure partie de ce déplacement spectral se produit entre 60 et 80 °C. L'origine de ce phénomène apparaît clairement dans la figure 2.4b, qui montre la variation de la longueur d'onde de résonance en fonction de la température au même angle de θ_{air} = 68°. En chauffant le dispositif à partir de la température ambiante, on observe d'abord un petit décalage linéaire de la résonance, suivi d'une variation plus abrupte (avec un point d'inflexion autour de 70 °C) et, enfin, d'un ralentissement au-dessus d'environ 80 °C. Alors que les déplacements linéaires de la résonance à basse et haute températures dénotent des effets de thermoréflectance ordinaires, la variation abrupte peut être attribuée sans ambiguïté au phénomène SCO. Cette figure permet donc d'évaluer clairement le déplacement de la résonance, qui est associé uniquement à la commutation de l'état de spin ($\Delta\lambda_{SCO} \approx 30$ nm) sans aucun effet thermique de fond. On peut également remarquer qu'après le premier chauffage, qui est toujours quelque peu anormal, les courbes de chauffage-refroidissement suivantes se chevauchent étroitement, ce qui dénote une bonne réversibilité de la commutation.

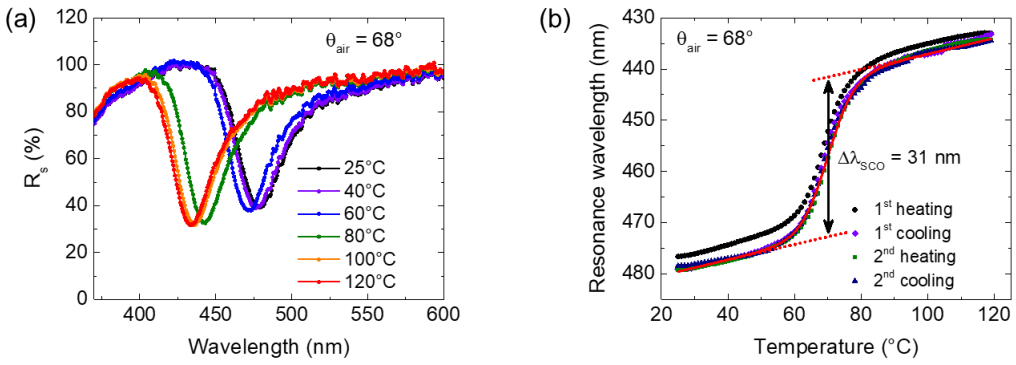

Figure 2.4. (a) Spectres de réflectance de la bicouche Ag (35 nm)/**1** (162 nm) enregistrés à différentes températures (polarisation s, θ_{air} = 68°) montrant le déplacement du pic de résonance lors de la transition de spin. (b) Variation thermique de la longueur d'onde de résonance sur deux cycles de chauffage et de refroidissement.

Si l'on compare les deux dispositifs étudiés, à savoir la cavité Fabry-Pérot Ag (40 nm)/**1** (142 nm)/Ag (40 nm) et le résonateur Ag (35 nm)/**1** (162 nm), qui possèdent le même matériau pour le changement d'indice de réfraction, leurs conditions de fabrication sont comparables. Cependant, la comparaison de leur accordabilité optique (voir figure 2.5) révèle une sensibilité à l'indice de réfraction 6 fois plus élevée pour le résonateur Ag (35 nm)/**1** (162 nm), tout en gardant des valeurs de facteurs de qualité assez similaires. En ce qui concerne le contraste optique, la variation maximale de la transmittance est de ΔTr = 3 % pour la cavité Ag (40 nm)/**1** (142 nm)/Ag (40 nm), contre une variation de la réflectance de ΔR = 68 % pour le résonateur Ag (35 nm)/**1** (162 nm). Dans l'ensemble, les différents facteurs de mérite mesurées pour le résonateur Ag /**1** sont sensiblement supérieurs à ceux obtenus pour la cavité Ag/**1**/Ag, incorporant le même matériau SCO. Ainsi, ces considérations montrent que, pour un matériau de changement d'indice de réfraction donné et des conditions de fabrication comparables, la conception du résonateur est d'une grande importance pour obtenir un contraste optique élevée.

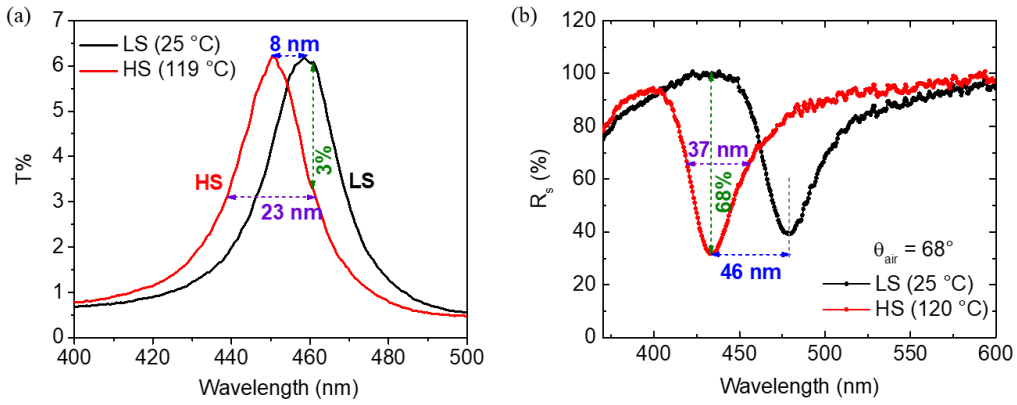

Figure 2.5. (a) Spectres de transmittance acquis dans les états HS et LS (polarisation s, θ_{air} = 60°) pour la cavité Ag (40 nm)/**1** (142 nm)/Ag (40 nm). (b) Spectres de réflectance acquis dans les états HS et LS (polarization s, θ_{air} = 68°) pour le résonateur Ag (35 nm)/**1** (162 nm). Pour les deux dispositifs, les décalages de résonance, les largeurs de résonance et les modulations optiques sont indiqués par des flèches en pointillés.

Chapitre 3. Commutation d'un couplage lumière-matière

ultra-fort à un couplage faible à l'aide de molécules à transition de spin

Dans ce chapitre, nous mettrons en œuvre, pour la première fois, une approche qui consiste à concevoir un résonateur optique de telle sorte qu'un mode optique tombe dans le domaine des longueurs d'onde UV, où nos composés moléculaires présentent des bandes d'absorption intenses, dépendantes de l'état de spin. En d'autres termes, l'idée principale est maintenant de mettre en résonance un mode de cavité avec une excitation moléculaire, dans le but d'atteindre (et d'exploiter) un ***régime de fort couplage lumière-matière*** entre la structure photonique et les molécules SCO. Étant donné que les excitations moléculaires (ou bandes d'absorption) sont différentes dans les deux états de spin, la transition de spin devrait permettre de moduler l'intensité du couplage entre les molécules et le résonateur optique.

Comme le montre la figure 3.1, lorsqu'une excitation moléculaire entre en résonance avec un mode de la cavité, un échange rapide d'énergie (par l'échange de photons) peut se produire entre la cavité optique et le matériau. En particulier, si cet échange d'énergie devient plus rapide que tout processus de dissipation (fuite de photons de la cavité) ou de décohérence (déphasage moléculaire), alors le régime dit de couplage fort apparaît entre la matière et le champ électromagnétique (EM) environnant. Dans ce cas, de nouveaux états hybrides lumière-matière (avec un caractère mixte moléculaire et photonique) - connus sous le nom de polaritons - sont formés, avec une séparation d'énergie (appelée énergie de Rabi, $\hbar\Omega_R$) étant proportionnelle à la force de couplage [Hutchison 2012 ; Törmä 2014].

Pour coupler nos molécules SCO à des modes EM, nous avons fabriqué des résonateurs bicouches métallo-diélectriques (excités à l'aide d'un prisme de couplage), [prisme / Al (16 nm) / [Fe(HB(1,2,4-triazol-1-yl)$_3$)$_2$] (138 nm)], cavité **1**, et [prisme / Al (16 nm) / Fe(HB(1,2,3-triazol-1-yl)$_3$)$_2$ (153 nm)], cavité **2**. Pour rappel, des propriétés d'absorption des films des composés **1** et **2** sont exposés dans le Figure 2.1 et 3.2,

respectivement.

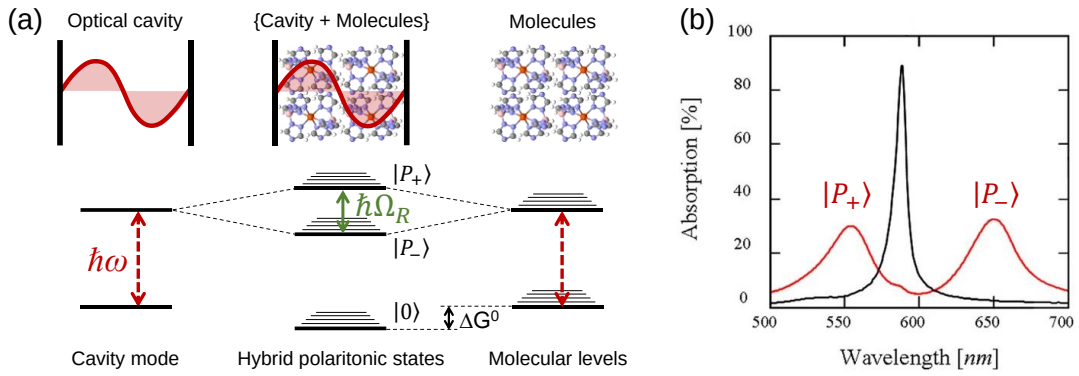

Figure 3.1. (a) Schéma énergétique simplifié d'un système {molécules + cavité} en régime de couplage fort. La résonance entre l'excitation moléculaire (électronique ou vibrationnelle) et le mode de la cavité $\hbar\omega$ conduit à la formation de deux états hybrides lumière-matière (polaritoniques), $|P_+\rangle$ et $|P_-\rangle$, séparés par l'énergie de Rabi, $\hbar\Omega_R$. Il est intéressant de noter que l'énergie du niveau fondamental du système couplé peut également être modifiée (ΔG^0) par le couplage fort. (b) Spectre d'absorption expérimental d'une molécule colorante avant (courbe noire) et après (courbe rouge) avoir subi un couplage fort lumière-matière avec une cavité. [Ebbesen 2016]

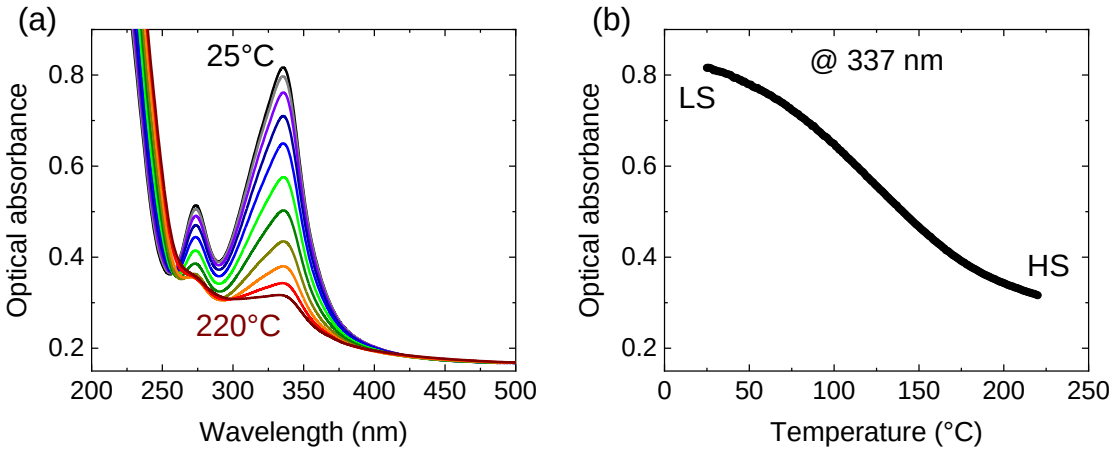

Figure 3.2. Propriétés SCO des films minces du composé [Fe(HB(1,2,3-triazol-1-yl)$_3$)$_2$]. (a) Spectres d'absorbance optique d'un film de 153 nm d'épaisseur sur un substrat de silice fondue, enregistrés entre 25 et 220 °C. (b) Courbe de transition de spin thermique du même film extraite de la variation thermique de l'absorbance optique à λ = 337 nm.

En résumé, la figure 3.3 montre l'évolution en température des énergies de séparation

de Rabi, mesurées dans les deux résonateurs étudiés, démontrant la possibilité d'une modulation thermique de la force de couplage lumière-molécule, entre un régime de couplage fort et un régime de couplage faible. Il est intéressant de noter qu'en raison des propriétés d'absorption comparables des deux complexes SCO étudiés à température ambiante (dans l'état LS), les deux résonateurs fabriqués présentent un régime de couplage ultra-fort avec des énergies de Rabi similaires d'environ 550 meV. De plus, nous montrons que le changement de régime de couplage suit les caractéristiques de la transition thermique de spin. En effet, les deux résonateurs étudiés ici représentent deux cas antagonistes : alors que la cavité **2**, incorporant le complexe [Fe(HB(1,2,3-triazol-1-yl)$_3$)$_2$], présente une variation très progressif de la force d'hybridation sur une large gamme de température (permettant ainsi un contrôle externe étroit de la force de couplage), la cavité **1** (incorporant le composé [Fe(HB(1,2,4-triazol-1-yl)$_3$)$_2$]) présente une commutation ON/OFF relativement abrupte du régime de couplage. Il convient de mentionner que dans les deux cas, la commutation entre les régimes de couplage ultra-fort et faible peut être réalisée de manière réversible et entièrement reproductible.

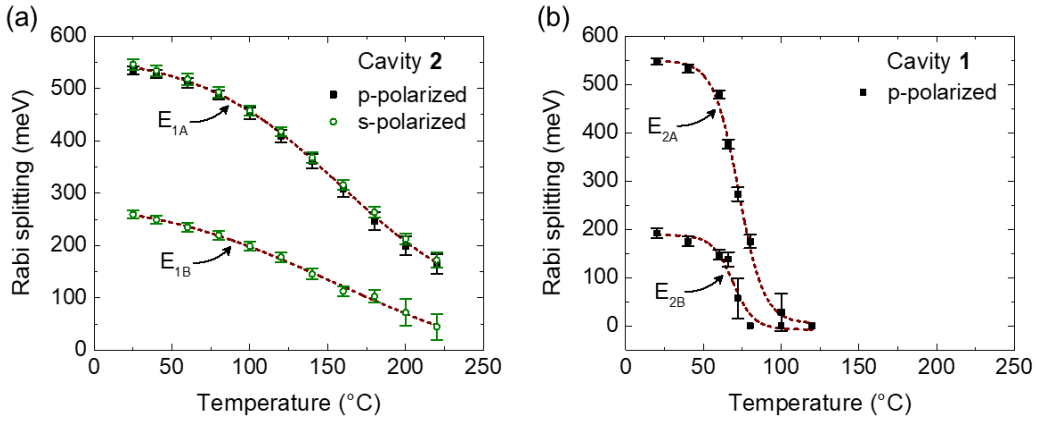

Figure 3.3. Variation de la force du couplage lumière-matière avec la température dans les deux résonateurs étudiés. Évolution en température des énergies de Rabi mesurées dans (a) la cavité **2** et (b) la cavité **1**, incorporant un film mince SCO des complexes [Fe(HB(1,2,3-triazol-1-yl)$_3$)$_2$] et [Fe(HB(1,2,4-triazol-1-yl)$_3$)$_2$], respectivement. Les lignes en pointillé sont des guides pour l'œil.

En conclusion, nous avons démontré un couplage lumière-matière commutable entre

les modes optiques des résonateurs bicouches métal/diélectriques et les molécules SCO. Dans leur état LS, les bandes d'absorption intenses des molécules SCO dans le domaine spectral UV peuvent être couplées aux modes de photons de la cavité, ce qui entraîne des énergies de Rabi allant jusqu'à 550 meV, c'est-à-dire ~15 % de l'énergie d'excitation moléculaire. En convertissant thermiquement les molécules dans leur état HS non absorbant, nous démontrons la possibilité de régler finement la force d'hybridation, permettant finalement une commutation réversible et reproductible entre les régimes de couplage ultra-fort et faible dans un seul système photonique. En utilisant des films minces déposés sous vide de deux composés SCO ayant des propriétés de transition de spin différentes, une commutation graduelle et abrupte du régime de couplage a pu être obtenue avec la température.

Conclusions générales et perspectives

Les électrons des orbitales 3d des matériaux à transition de spin se réarrangent sous l'effet de stimuli externes (tels que la température, la pression, les radiations lumineuses, etc.) Ces changements électroniques et structurels entraînent des modifications importantes des propriétés optiques du matériau dans toute la gamme spectrale UV-VIS-NIR. Basé sur cet atout des composés SCO, ce travail de thèse se concentre sur leur application dans les domaines de l'optique et de la photonique avec l'objectif central de réaliser des dispositifs optiques reconfigurables, actifs et/ou adaptatifs. D'une part, des dispositifs optiques thermiquement modulables ont été construits, basés sur la commutation réversible de l'indice de réfraction entre les états haut spin et bas spin des matériaux SCO. Ensuite, nous avons exploré le couplage fort des molécules SCO aux modes électromagnétiques dans les cavités optiques et nous avons obtenu un contrôle fin de la force d'hybridation lumière-matière par la commutation de l'état de spin des molécules.

En ce qui concerne le premier axe de ce travail, le faible coefficient d'extinction dans le domaine visible et le changement considérable d'indice de réfraction à la transition de spin dans certains matériaux SCO offrent des avantages potentiels pour les applications photoniques par rapport à d'autres matériaux à changement de phase. En effet, le facteur de mérite pertinent ($FOM = \frac{\Delta n}{k_{min}}$) pour les composés SCO est généralement ≥ 100 dans la gamme VIS-NIR, alors que pour d'autres matériaux PCM, on observe généralement des valeurs de FOM de ≤ 1. Pour examiner de plus près cet avantage potentiel des matériaux SCO, nous avons construit des dispositifs optiques multicouches basés sur des matériaux SCO. Nous avons choisi le complexe SCO **1** [Fe(HB(1,2,4-triazol-1-yl)$_3$)$_2$] qui présente une transition de spin robuste et abrupte au-dessus de la température ambiante. Le premier dispositif, avec la structure Ag (40 nm)/**1** (142 nm)/Ag (40 nm), était basé sur des travaux antérieurs de l'équipe. Ses spectres de transmittance ont révélé un déplacement substantiel de la longueur d'onde de résonance de 6 nm dû à la commutation de l'état de spin, mais la modulation optique associée était

plutôt modeste (3 %). C'est pourquoi notre attention s'est portée sur le résonateur bicouche, Ag (35 nm)/**1** (162 nm), qui a été étudié en utilisant une méthode de réflexion interne totale. Comparé à la cavité Fabry-Pérot Ag (40 nm)/**1** (142 nm)/Ag (40 nm), le résonateur Ag (35 nm)/**1** (162 nm) est non seulement plus facile à fabriquer, mais offre également une plus grande sensibilité au changement d'indice de réfraction, montrant un décalage spectral important du mode résonant ($\Delta\lambda_{SCO}$ = 30 nm) lors de la SCO, et, finalement, une modulation optique plus élevée (70 %). De manière intéressante, nous démontrons que la grande sensibilité thermique du dispositif donne également lieu à une non-linéarité photothermique, qui peut être exploitée pour réaliser des applications de limitation optique, c'est-à-dire un dispositif adaptatif. Dans l'ensemble, nous démontrons ainsi que les composés SCO constituent une classe prometteuse de matériaux à changement de phase présentant une transparence optique à large bande dans le domaine visible, ce qui est un atout très recherché pour le développement d'applications photoniques à faibles pertes. Dans ce contexte, la perspective est d'explorer d'avantage l'applicabilité de nos matériaux dans des dispositifs réels, tels que les circuits intégrés photoniques (PIC) et les modulateurs spatiaux de lumière (SLM). Notamment, pour les applications PIC, la technologie des guides d'ondes en nitrure de silicium semble prometteuse car elle ouvre des perspectives de transparence jusqu'à la région spectrale visible [Roeloffzen 2013]. Cependant, l'actionnement thermique du dispositif est peu efficace. Il semble donc particulièrement intéressant d'intégrer les matériaux SCO aux plateformes en nitrure de silicium, ce qui peut permettre de combiner les avantages de ces dernières avec une modulation optique rapide et efficace.

En ce qui concerne le deuxième axe de notre travail, profitant du changement d'absorbance accompagnant le phénomène SCO, nous avons exploré le couplage fort des molécules SCO avec des modes électromagnétiques dans des cavités optiques constituées de bicouches Al/SCO. En effet, la formation d'états hybrides lumière-matière, par l'interaction résonante de champs électromagnétiques confinés avec des excitations de la matière, apparait comme un outil fascinant pour contrôler les états quantiques et ensuite manipuler les fonctionnalités de la matière et le paysage de la

réactivité chimique. Nous présentons ici la première observation d'un couplage lumière-matière fort et commutable impliquant des molécules à transition de spin des composés [Fe(HB(1,2,4-triazol-1-yl)$_3$)$_2$] et [Fe(HB(1,2,3-triazol-1-yl)$_3$)$_2$]. Les mesures spectroscopiques, appuyées par des simulations numériques, ont révélé des énergies de Rabi allant jusqu'à 550 meV, ce qui, à 15 % de l'énergie d'excitation moléculaire, permet d'entrer dans le régime de couplage ultra-fort. Nous constatons que la commutation thermiquement induite des molécules entre leur état de bas spin et de haut spin permet un contrôle fin de la force d'hybridation lumière-matière, offrant la possibilité attrayante d'une commutation réversible entre les régimes de couplage ultra-fort et de couplage faible à l'intérieur de la cavité. D'autre part, l'écart d'énergie entre les deux états de spin n'a pas été modifié par le couplage. Grâce à ce travail, nous montrons que les composés moléculaires SCO constituent une classe prometteuse de nanomatériaux actifs dans le contexte florissant des dispositifs polaritoniques accordables et de la chimie polaritonique. En ce qui concerne les perspectives du couplage lumière-matière, nous cherchons à moduler les propriétés de transition de spin en couplant l'un des deux états de spin moléculaire à un mode de cavité. Cette propriété pourrait être le "Saint Graal" dans le domaine de la transition de spin, permettant, par exemple, des propriétés photophysiques ajustables par couplage aux modes EM. Nous continuerons à étudier le couplage fort des molécules SCO aux modes électromagnétiques dans les cavités Fabry-Pérot. Notamment avec des complexes SCO avec différents types de transition de spin (tels que la transition de spin graduelle, la transition de spin abrupte et la transition de spin avec hystérésis, etc.) seront intégrés dans des structures Al/SCO/Al et leurs propriétés SCO seront examinées en utilisant des excitations lumineuses statiques et dynamiques.

Titre: Dispositifs photoniques actifs à base de molécules à transition de spin

Mots clés: transition de spin, couches minces, cavités optiques, couplage lumière-matière

Résumé : Cette thèse se focalise sur l'étude des matériaux moléculaires à transition de spin (SCO) et vise à utiliser le changement des propriétés optiques accompagnant la commutation de l'état de spin pour concevoir des dispositifs optiques actifs. Plus précisément, deux objectifs de recherche ont été poursuivis. D'une part, nous exploitons la variation de l'indice de réfraction de ces matériaux, Δn, entre les états bas-spin (LS) et haut-spin (HS), pour concevoir des résonateurs optiques thermiquement accordables, fonctionnant dans la gamme spectrale du visible. D'autre part, nous exploitons le changement du coefficient d'extinction, Δk, lors de la transition de spin, pour explorer les effets de couplage lumière-matière qui peuvent exister entre les molécules SCO et les modes électromagnétiques de cavité. Pour le premier objectif, des cavités Fabry-Pérot Ag/SCO/Ag ainsi que des résonateurs bicouches Ag/SCO ont été fabriqués en incorporant le complexe à transition de spin [Fe(HB(1,2,4-triazol-1-yl)$_3$)$_2$]. Nous avons montré que la commutation des molécules de l'état LS vers l'état HS entraine des déplacements spectraux importants des modes de résonance de la cavité vers le bleu (jusqu'à 30 nm), ainsi qu'une modulation notable du signal optique associé (jusqu'à 70 %). Ces différents effets ont été rationalisés via des simulations de matrices de transfert. Nous avons montré que ces propriétés de modulation optique peuvent être utilisées pour des applications concrètes de limitation optique. Pour le second objectif de ce travail de thèse, des structures résonantes bicouches Al/SCO ont été fabriquées en utilisant deux complexes isomères, [Fe(HB(1,2,4-triazol-1-yl)$_3$)$_2$] et [Fe(HB(1,2,3-triazol-1-yl)$_3$)$_2$], qui présentent respectivement une transition de spin thermique abrupte et graduelle entre les états LS et HS. La mise en résonance des modes optiques avec les bandes d'absorption moléculaires nous a permis d'atteindre un régime de couplage fort lumière-matière avec des énergies de Rabi allant jusqu'à 550 meV. Nous avons montré que la commutation des molécules entre les deux états de spin permet un contrôle fin de la force de ce couplage lumière-matière, en raison du changement du coefficient d'extinction du matériau pendant la transition de spin. Dans le cadre de cette thèse, nous montrons que les composés SCO constituent une classe prometteuse de matériaux optiques à changement de phase permettant un contrôle actif des dispositifs photoniques.

Title: Active photonic devices based on spin crossover molecules

Keywords: spin crossover, thin films, optical cavities, light-matter coupling

Abstract: This thesis focuses on molecular spin crossover (SCO) materials and aims at using the changes in optical properties accompanying the spin state switching to conceive active optical devices. Specifically, we follow two research strategies. On one hand, we harness the variation of the refractive index, Δn, between the low spin (LS) and high spin (HS) states to fabricate thermally tunable optical resonators working in the visible wavelength range. On the other hand, we exploit the change of the extinction coefficient, Δk, upon the spin transition to explore the light-matter coupling effects that can exist between SCO molecules and electromagnetic modes in optical cavities. For the first aim, Ag/SCO/Ag Fabry-Pérot cavities and Ag/SCO bilayer resonators were fabricated incorporating the SCO complex [Fe(HB(1,2,4-triazol-1-yl)$_3$)$_2$]. The switching of SCO molecules from the LS to the HS states caused significant blue shifts of the cavity resonances (up to 30 nm), associated with large optical modulations (up to 70 %), which were rationalized by transfer-matrix simulations. We leveraged these properties to demonstrate prospects for applications in optical limiters. For the second aim, Al/SCO bilayer cavities were fabricated using two isomeric SCO complexes, [Fe(HB(1,2,4-triazol-1-yl)$_3$)$_2$] and [Fe(HB(1,2,3-triazol-1-yl)$_3$)$_2$], displaying abrupt and gradual SCO behaviors, respectively. The appropriate tuning of the cavity resonances allowed us to achieve light-matter strong coupling in both systems with Rabi-splitting energies up to 550 meV. We demonstrated that the thermally induced switching of molecules between the two spin states allows a fine control of the light-matter hybridization strength, due to the change in the extinction coefficient during the spin transition. Through this thesis, we show that SCO compounds constitute a promising class of optical materials, providing scope for active tuning and reconfiguration of photonic devices.